Mechanical Regulation of Clathrin-Mediated Endocytosis by Membrane Bending Protein Epsin

by

Jophin George Joseph

A dissertation submitted in partial fulfillment
of the requirements for the degree of
Doctor of Philosophy
(Mechanical Engineering)
in The University of Michigan
2022

Doctoral Committee:

Associate Professor Allen Liu, Chair
Associate Professor Arun Anantharam
Associate Professor Jinaping Fu
Professor Joel Swanson

Jophin George Joseph

jgjoseph@umich.edu

ORCID iD: 0000-0003-0128-831X

Dedication

I would like to dedicate this thesis to my parents, whose hard work and perseverance have helped me become the person I am today.

Acknowledgements

First and foremost, I thank God Almighty for blessing me with his wisdom and knowledge throughout my life. I would like to thank my parents Joseph and Jessy for their guidance, support and motivation in my life. I like to specially thank my sister Jane, for her unyielding support and motivation in my life.

I would like to specifically thank Dr. Allen Liu for being a great PhD advisor and a good role model in both personal and professional life. I would like to thank my committee members, Dr. Joel Swanson, Dr. Jianping Fu and Dr. Arun Anantharam for providing me valuable directions in my research. I would like to thank my collaborators Dr. Ashutosh Agrawal and Carlos Osorio, Dr. Akira Ono, Dr. Rajat Mudgal for their contribution to my work. I acknowledge members of microscopy core and SMART center specifically Eric and Damon. I thank my previous lab mates Max, Luciana, Xinyu and Sagardip whose inputs were essential in the success of my research. I also like to thank Vivian and Dominic who helped me performed lot of the experiments.

I would like to thank all my friends in Ann Arbor who made this last 5 years very enjoyable. I express my gratitude Liz for being a such an important part of my life by providing me emotional and moral support during this journey. I like to specifically mention my roommate Aniruddhe, my friends Sachin, Tess, Anilash, Joel, Tibin, Stephen and Daniel who made Ann arbor a special place. Finally I acknowledge all my family, friends, teachers and mentors, lab members and collaborators for supporting me throughout each stages of my education and research. Without the support of each and every one of these individuals, this dissertation would not have been possible

Table of Contents

List of Tables

List of Figures

Abstract

Cells are complex biomechanical systems that constantly adapt to and modify their physical environment. The cell membrane is the boundary that separates organelles and other molecular machineries in a cell from the extracellular environment and plays a major role in maintaining the biochemical and biomechanical homeostasis of cells. The constant deformation and remodeling of cell membranes is key in biological processes like cell division, polarization and migration. It also enables the trafficking of a diverse ensemble of cargos in and out of cells by endocytosis and exocytosis, respectively. This remodeling process is regulated by mechanical factors like membrane tension, rigidity, substrate stiffness, morphology of the cargo,…etc.

Clathrin-mediated endocytosis (CME) is an endocytic pathway by which cells internalize cargos from the extracellular environment by extensive remodeling of the plasma membrane from a flat to a bud morphology supported by clathrin-coat assembly. Epsin is an adaptor protein in CME that aids in membrane bending and is recruited prior to clathrin to clathrin-coated pit (CCP) nucleation sites. Epsin has a structured N-terminal ENTH (epsin N-terminal homology) region and an unstructured C-terminal IDP (intrinsically disordered protein) region that are involved in membrane bending via amphipathic helix insertion and steric repulsion, respectively. Membrane tension plays an inhibitory role in CME by destabilizing CCP assembly. My investigation shows that overexpressing epsin rescues the stability of CCPs under high membrane tension. The recruitment of epsin to CCPs increases with elevated membrane tension. Masking the N-terminus of ENTH with EGFP or deletion of ENTH in epsin delays recruitment of epsin to CCP

nucleation sites. Interfering with the activity of the H_0 helix abrogates the elevated recruitment of epsin at high tension. The ENTH domain, while necessary for tension sensitivity of epsin, is not necessary for epsin puncta formation. Deletion of adaptor protein 2 binding sites and clathrin binding sites in the IDP domain of epsin renders it cytosolic. Further, the IDP domain itself is sufficient to impart stability to CCPs as CCPs recruiting epsin with only IDP domain shows reduction in the fraction of abortive pits. My findings conclude that H_0 alpha helix in the ENTH domain of epsin acts as a tension sensor and the IDP domain acts as a tether stabilizing CCPs. Our work reveals the complimentary action of structured ENTH and unstructured IDP domains of epsin supporst CME at high tension.

CME is also utilized by pathogens like Influenza A virus (IAV) to gain access to host cells. Epsin is a known cargo-specific adaptor for IAVs. Epsin interacts with ubiquitinated surface receptors bound to IAVs via its ubiquitin-interacting motifs. My investigation shows that the ENTH domain in epsin biomechanically regulates curvature generation around spherical IAVs thereby initiating CME of the virion. Mutations in the H_0 helix negatively regulate the recruitment of epsin to CCPs containing spherical IAVs and their subsequent internalization. However, internalization of filament-forming IAVs were not affected by the inhibition of H_0 helix formation in ENTH domain of epsin.

In summary, the findings of this dissertation define the biomechanical role of epsin in CME under high membrane tension conditions and during viral entry. By improving our understanding of biomechanics of endocytosis and viral entry, I hope that this research will lead to development of better therapies targeting abnormal endocytosis pathways and viral diseases, as well as advances in viral vector and nanoparticle-based drug delivery systems.

Chapter 1 Introduction

This chapter was published as review in *Advanced Biosystems* (2020). J.G.J. and A.P.L. wrote the review.

1.1 Mechanical regulation of endocytosis

Endocytosis involves transport of nutrients, macromolecules and pathogens across the plasma membrane by forming membrane invaginations and subsequently internalizing the cargo in a membrane-enclosed vesicle. Eukaryotic cells have evolved multiple pathways of endocytosis to internalize cargos of different types and sizes. Endocytosis plays a role in various cellular processes including signal transduction, immune response, cell division, and cell migration [1–3]. Endocytic pathway is often exploited by toxins and pathogens like bacteria and viruses to gain entry into a cell [4], but cells also rely on endocytosis to neutralize pathogens [5]. A critical step of several endocytic pathways is the formation of the budded membrane invagination by sculpting the plasma membrane. Different endocytosis pathways utilize different protein complexes to generate and stabilize membrane buds [6]. Mechanical factors like bending rigidity of the lipid bilayer, membrane tension, stiffness of the extracellular matrix (ECM), shape, size and stiffness of the cargo can affect the effectiveness of the remodeling process [5–8]. Membrane rigidity and membrane tension act as limit agents against the spontaneous membrane curvature generation by creating an energy barrier for membrane deformation. Activity of curvature generating proteins or processes including imposition of intrinsic protein curvature onto the membrane (BAR proteins), insertion of amphipathic helix (E/ANTH domain proteins), steric repulsion by protein crowding,

and polymerization of actin networks, is required for bud formation [9]. Furthermore, the aforementioned mechanical factors also regulate the fission of membrane invaginations to create endocytic vesicles [1]. Quantifying the effects of mechanical factors on membrane curvature generation and membrane scission is critical for understanding how these factors influence the overall trafficking and regulatory role of endocytosis. Since nanoparticle-based drug delivery systems target different endocytic pathways in cells, understanding the interplay between mechanical factors and endocytosis can aid in better designs of these drug carrier systems [8].

Most endocytic events (<100 nm) occur below the diffraction limit of light. Hence, studying the morphological development of endocytic structures using conventional optical microscopy does not offer sufficient spatial resolution for in-depth dissection of its assembly. Further, robust techniques to control mechanical properties of cells were largely inaccessible until the last decade. Hence, our understanding of mechanoregulation of endocytosis primarily came from molecular simulations and *in vitro* reconstitution of endocytic proteins in vesicles. Recent developments, improvements, and implementation of advanced microscopy techniques like stochastic optical reconstruction microscopy (STORM), structured-illumination microscopy (SIM), polarized total internal reflection fluorescence (TIRF) microscopy, correlative light and electron microscopy (CLEM) have enabled researchers to look beyond diffraction limit into the protein architecture of endocytic structures while they are budding [10]. Robust techniques to mechanically manipulate cells which are compatible with high-resolution microscopy, like cell stretchers, microcontact printing, stiffness tunable hydrogels, and micropillar arrays also gained progress in the last decade [11–13]. Automated algorithms for detecting and tracking endocytic events coupled with these sophisticated imaging techniques have enabled visualization of endocytosis in living organisms [14,15].

Simultaneous utilization of sub-diffraction-limited microscopy and robust techniques to mechanically manipulate cells have provided us with important insights into how endocytic protein complexes respond to mechanical stimuli. These sophisticated techniques have spurred interests in recent years to experimentally validate theoretical and computational predictions on the mechanobiology of endocytosis. At the same time, these advances have reignited once settled controversies about endocytosis. Newer studies utilizing aforementioned techniques have called into question whether membrane bud formation in clathrin-mediated endocytosis occur primarily via a constant curvature mechanism, or the newly emerging flat-to-dome mechanism [11,16]. Recent findings have also strengthened non-specific membrane bending hypotheses like steric crowding as an alternative to protein-specific mechanisms such as amphipathic helix insertion [17,18].

Mechanoregulation is shown to affect endocytosis pathways including macropinocytosis, phagocytosis, caveolae-mediated endocytosis, clathrin-mediated endocytosis (CME), and caveolae and clathrin-independent endocytosis (CIE) **(Figure 1.1)**. In the following sections of Chapter 1 I will survey recent studies that provided insights into mechanoregulation of endocytosis. Specifically, I will discuss how several key mechanical factors, including (i) membrane tension, (ii) membrane rigidity, (iii) physical properties of extracellular surroundings, and (iv) physical properties of cargo **(Figure 1.2)** affect the membrane sculpting associated with endocytosis pathways. Further I will analyze mechanoregulation of individual steps of CME, one of the prominent endocytic pathways. Competing hypotheses on mechanoregulation of membrane sculpting will be scrutinized to provide a progress report on the present state of understanding on how mechanical cues control endocytosis.

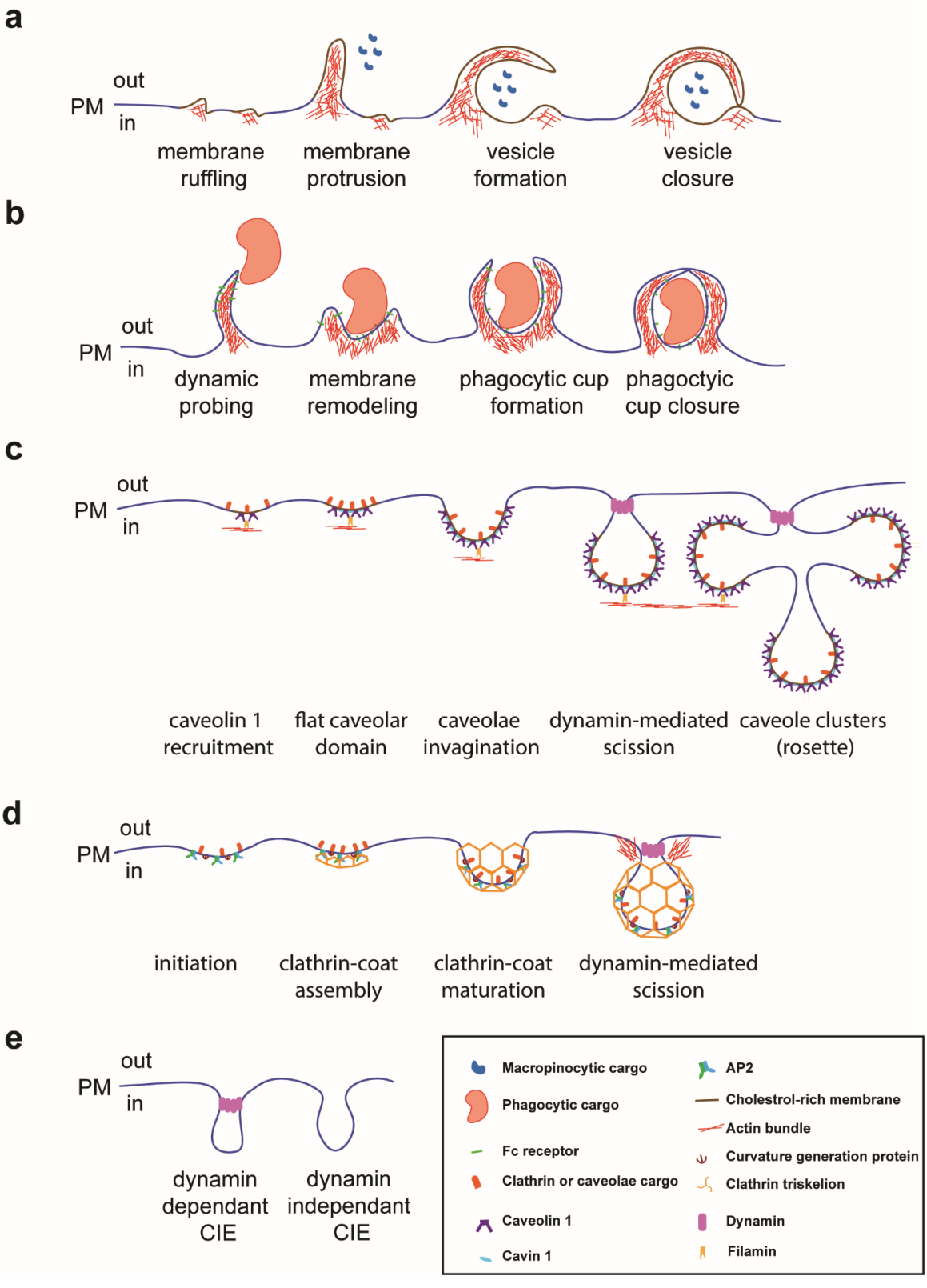
a
out
PM
in
membrane ruffling
membrane protrusion
vesicle formation
vesicle closure
b
out
PM
in
dynamic probing
membrane remodeling
phagocytic cup formation
phagoctyic cup closure
c
out
PM
in
caveolin 1 recruitment
flat caveolar domain
caveolae invagination
dynamin-mediated scission
caveole clusters (rosette)
d
out
PM
in
initiation
clathrin-coat assembly
clathrin-coat maturation
dynamin-mediated scission
e
out
PM
in
dynamin dependant CIE
dynamin independant CIE
Macropinocytic cargo
Phagocytic cargo
Fc receptor
Clathrin or caveolae cargo
Caveolin 1
Cavin 1
AP2
Cholestrol-rich membrane
Actin bundle
Curvature generation protein
Clathrin triskelion
Dynamin
Filamin

Figure 1.1. Progression of endocytic pathways.

a. Macropinocytosis is initiated by actin polymerization near the membrane in response to receptor activation, leading to membrane ruffling. Membrane protrusions are formed from the ruffles which may fold back to the plasma membrane to form vesicles. The fusion of folded membrane protrusions to basal membrane create macropinosomes, encapsulating extracellular fluid and other cargo [19]. **b.** Phagocytosis is initiated by binding specialized receptors on the cell membranes to target particles. Phagocytic cells like macrophages actively probe for pathogens by forming pseudopodial extensions. Once the particle for internalization is located, the plasma membrane is remodeled by actin polymerization to wrap around the particle to form a phagocytic cup. The phagocytic cup is closed by the depolymerization of actin at the base of the cup, forming a membrane bound phagosome [20]. **c.** Caveolae-mediated endocytosis is initiated at cholesterol-rich membrane sites by the recruitment of caveolin-1. Caveolae associated proteins like cavin 1 enables the polymerization of caveolin-1, leading to the formation of caveolae. Caveolae are linked with actin stress fibers through filamin A. Membrane tension and stress fiber activity mediate the transformation of caveolae into an Ω shape, enabling dynamin-mediated scission. High membrane tension and excess stress fiber linkage can flatten caveolae, whereas a sudden drop in membrane tension and stress fiber disruption lead to formation of caveolae clusters known as rosettes [21]. **d.** Clathrin-mediated endocytosis is initiated by the recruitment of adaptor protein AP2 and membrane bending proteins like E/ANTH domain proteins and F-BAR proteins to the membrane. Clathrin triskelia bind to AP2 and polymerize to form clathrin coats with hexagonal and/or pentagonal faces. Whether the coat is formed before or after the start of membrane bending is still contested. Once the coated pit matures to a hemispherical shape, it is transitioned to an Ω shape (with the help of actin at high tension), enabling dynamin-mediated scission [1] **e.** Clathrin-independent endocytosis pathways exist in two types. Pathways which utilize dynamin for membrane scission and pathways which do not utilize dynamin for membrane scission [6].

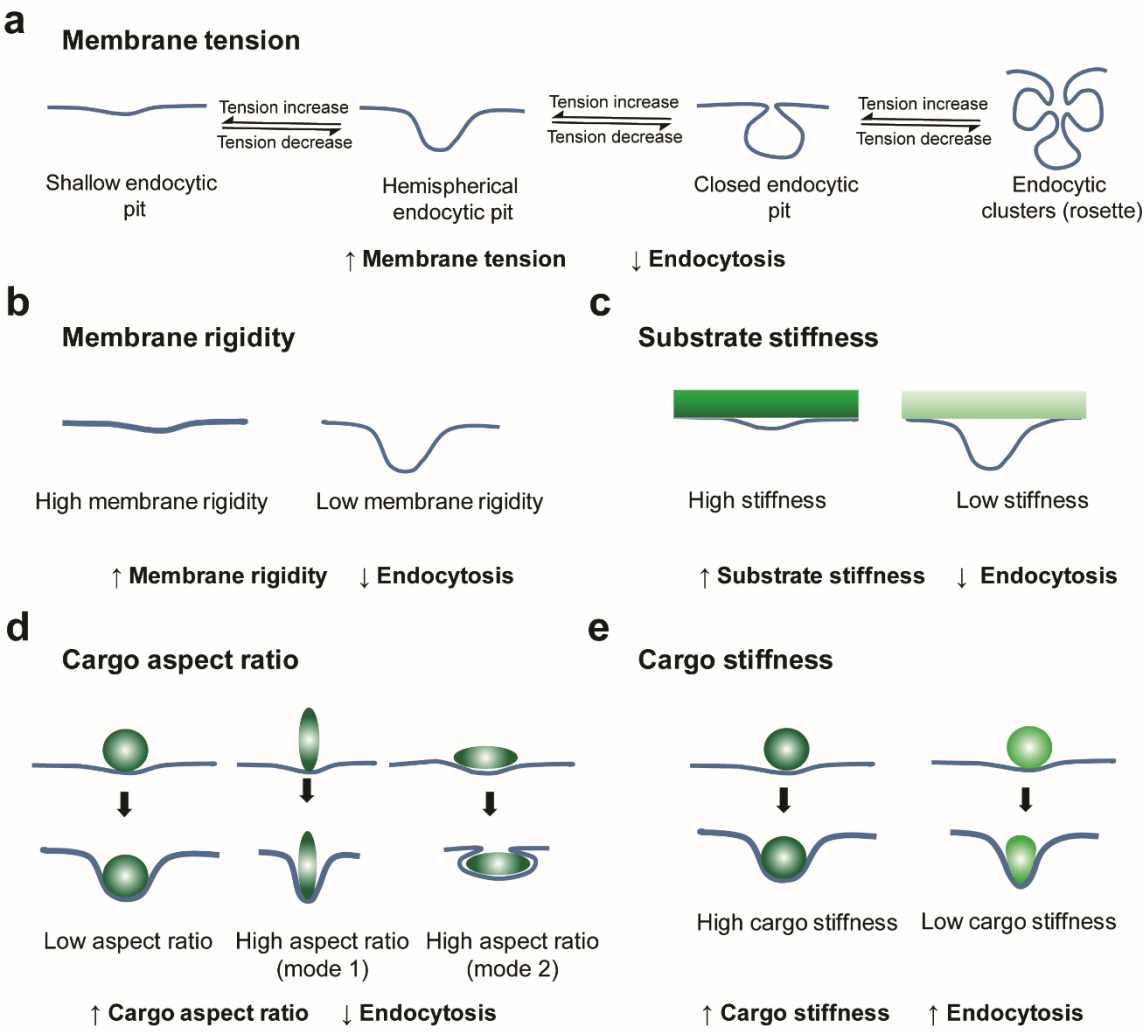

Figure 1.2. Effect of mechanical stimuli on endocytosis.

a. Membrane bending requires work done against membrane tension. Transition of membrane from flat-to-dome and dome-to-Ω shape is mediated by recruitment of proteins which provide energy to overcome the membrane tension energy barrier [9,39]. An acute increase in membrane tension leads to the flattening of membrane buds and an acute reduction in membrane tension can lead to the formation of endocytic clusters (in caveolae-mediated endocytosis) [21,92]. **b**. Bending rigidity of plasma membrane defines its resistance to undergo bending. Bending rigidity of the plasma membrane depends on the composition of membrane and protein recruitment to the plasma membrane alters membrane rigidity [27,28]. **c.** Extracellular substrate stiffness regulates the ability of membrane to undergo deformation. Membrane adhered to a stiffer substrate is less deformable compared to the ones adhered on a softer substrate. [30]. **d.** Cargos with low aspect ratio (spherical shape) can be easily internalized by endocytic pathways due to the ease of membrane wrapping around them. High aspect ratio of cargo can inhibit endocytosis by impeding membrane wrapping. High aspect ratio cargos can be internalized by membrane wrapping from its pole (mode 1) or membrane wrapping along its shallow edge (mode 2). Cells prefer pole-based internalization of high aspect ratio cargos [8,56,192]. **e.** Stiffer cargo is internalized *via* wrapping the cellular membrane without deforming the particle. Softer cargo undergoes large deformation during internalization causing changes in aspect ratio thereby increasing the energy barrier for full wrapping [8,59,137].

1.2 Mechanical factors regulating endocytosis

It is well appreciated that several mechanical factors regulate endocytosis. In this section, I will provide an overview of different mechanical factors, considering the properties of membrane, extracellular interaction, and cargo.

1.2.1 Membrane tension

The plasma membrane of cells is under tension as a result of the in-plane tension in the lipid bilayer due to intracellular hydrostatic pressure and the cortical tension due to the cortical actin cytoskeleton [22]. In-plane tension and cortical tension are interdependent [23] and together they play a major role in regulating endocytosis [22,24]. Membrane tension affects the rate of nucleation and lifetime of endocytic events in different pathways by inhibiting curvature formation and membrane scission [11,23,25,26]. Coarse-grained simulations have shed light on the inhibitory effect of membrane tension on curvature generation [27,28]. At high membrane tension (0.2 pN/nm), the assembly of coat proteins may not be sufficient for spontaneous flat-to-dome transition of plasma membrane critical for endocytosis. Whereas, at low membrane tension (0.002 pN/nm), increasing coat area of endocytic proteins induces flat-to-dome transition in the membrane. An acute drop in membrane tension is also associated with initiation of ultrafast endocytosis and formation of clustered endocytic structures [21,29]. Increased membrane tension also inhibits the transition of membrane invaginations from an open (U shape) to a close (Ω) topology **(Figure 1.2a)** [27,28]. An increase in plasma membrane tension has been associated with stalling of endocytic structures in the membrane [11,26] and an alteration of the morphology and size of endocytic pits [21,30–32]. Action of actin cytoskeleton and membrane curvature generation proteins is necessary to rescue endocytosis at high tension [26,28,33]. Membrane tension and concentration of endocytic coat proteins control the

shape of membrane invaginations [28,33] . For instance, membrane tubulation can be induced by increasing protein coverage at constant membrane tension or by decreasing membrane tension at constant coverage [33].

In the last decade, we have gained a better understanding of the role membrane tension plays in several classical pathways of endocytosis (*e.g.*, CME, phagocytosis) [22,34]. At the same time, newer studies are putting much more emphasis on CIE pathways and their coupling with exocytosis as a major response mechanism against membrane tension variations [6,35]. I expect such studies to uncover deeper insights into how cells cope with acute variation in membrane tension (*e.g.*, muscle cells), perhaps by coupling of fast endocytosis and exocytosis to prevent membrane damage.

1.2.2 Membrane rigidity

Bending rigidity of the plasma membrane determines the resistance of the lipid bilayer to bending [36,37]. Bending rigidity of the bilayer strongly depends on the composition of the membrane [37]. Reduction of bending rigidity of the membrane by incorporation of polyunsaturated phospholipids was shown to increase endocytic activity [38]. Amphipathic insertion of protein into membranes initiates membrane budding by altering membrane rigidity [39]. Alpha helix insertion rigidifies the membrane and induces spontaneous curvature in a lipid bilayer. However, as the insertion depth increases, the membrane rigidity reduces after reaching a maximum [40]. Concurrently, spontaneous curvature changes from positive to negative [40]. Once the endocytic coats are formed, the increased rigidity imparted by the coat proteins stabilizes invaginations [36,41]. Membrane bending simulations showed that bending rigidity mediates the smooth transition between open (U shaped) to closed (Ω shaped) endocytic pits [28]. Membrane rigidity also controls the ease of scission of endocytic vesicles from the plasma membrane [42,43]. An increase in membrane rigidity delays or inhibits

vesicle scission by increasing the elastic energy barrier for dynamin-mediated membrane fission [43].

1.2.3 Physical confinement of cells and mechanical properties of extracellular matrix

Endocytosis pathways play important roles in mediating the interaction between cells and the ECM. Physical confinement of cells and properties of ECM like stiffness have been shown to regulate endocytosis [5,44] **(Figure 1.2c)**. Cells spread on large adhesive islands showed a reduction in endocytic and phagocytic activity [32,45]. Changes in stiffness of ECM, due to infection or other disease conditions, can initiate phagocytosis response in macrophages [46,47]. Increase in matrix stiffness enhances vascular endothelial growth factor receptor VEGFR-2 internalization, signaling, and proliferation of tumor-like phenotype in endothelial cells [48,49]. Endocytosis of integrin β1 in bone marrow mesenchymal stem cells on collagen I-coated substrates promotes cell differentiation to a neuronal lineage [50]. Thus, cells may utilize endocytic pathways as a mechanosensitive conduit for sensing and responding to changes in ECM. Physical confinement of cells and increase in ECM stiffness could downregulate membrane remodeling on the adherent face of cells, which is necessary for endocytosis. Increased substrate stiffness can inhibit or stall endocytosis on the adherent face of a cell [30]. Cells also respond to different substrate stiffnesses by preferentially up- or down-regulating specific endocytic pathways. Cellular uptake of nanoparticles by bovine aortic endothelial cells on a stiff substrate resulted in a higher total cellular uptake on a per cell basis, but a lower uptake per unit membrane area [51]. Cells cultured on softer hydrogel substrate exhibited reduced CME of transferrin without affecting the rate of CIE of cholera toxin subunit B [44]. Until recently, researchers have largely ignored the effect of physical microenvironment on endocytic pathways like phagocytosis [5]. This gap of knowledge was due to the fact that traditional cell-based studies are performed on 2-dimensional petri dishes. Wider usage of 3D and 2D cell culture

systems with tunable stiffnesses, that are amenable for high-resolution microscopy will hopefully bridge this knowledge gap. It is not yet clear whether an increase in ECM stiffness or physical confinement of cells have an inhibitory effect on all endocytic pathways. Furthermore, I have barely scratched the surface on the crosstalk between ECM properties and endocytic cargo properties, and how they regulate the endocytic machinery. Future works need to address the combinatorial effects of multiple mechanical stimuli on endocytosis.

1.2.4 Physical properties of cargo: shape, aspect ratio, stiffness

Endocytosis is the primary mode of entry for particulate matter into the cells like nanoparticles, viruses and bacteria. The physical properties of these cargos can often determine the type endocytic pathway used and the rate of uptake [52]. The endocytic pathway for nanoparticles depends on the size, aspect ratio and stiffness [8]. Hydrogel-based nanoparticles with a large bulk modulus (3000 kPa) were internalized at a higher rate by epithelial tumor cells and brain endothelial cells, compared to internalization of softer particles. The phagocytic rate by J774 macrophages is also higher for stiff particles compared softer ones [53]. Spherical nanoparticles with a 25 nm radius and made with different materials (gold, silica, single-walled nanotubes) have an optimum endocytic uptake [8,54,55]. Nanoparticles and other cargos with higher aspect ratio show reduction in uptake compared low aspect ratio ones. It is thought that an increase in aspect ratio impedes effective membrane wrapping needed for endocytic entry. However, when high aspect ratio nanoparticles become oriented with the major axis being perpendicular to the membrane, the nanoparticles may enter the cell by tip entry **(Figure 1.2d)** [8,51,56]. Interestingly, pathogens like *E. coli* and fungi form high aspect ratio filaments during infection, and this could cleverly inhibit phagocytosis and help pathogens evade an immune response [57,58]. Molecular dynamic simulations have shown that softer nanoparticles may increase the energy barrier for effective membrane

wrapping due to an increase in curvature of the leading edge of particle during internalization **(Figure 1.2e)** [8,59]. Interestingly, this deformation of nanoparticles during internalization negatively regulates uptake [59]. For instance, macrophages prefer uptaking stiff microgels *via* macropinocytosis and softer gels *via* phagocytosis [60]. This may be due the extensive membrane remodeling capability of the phagocytosis pathway. Optimizing the physical properties of nanoparticles and other drug delivery vehicles to improve cellular entry *via* endocytosis – a concept known as mechanotargeting – may drastically advance the specificity of cellular targeting [61–63].

In the following sections, I will review key understanding of how various physical and mechanical properties of the plasma membrane and cargo regulate specific endocytic pathways.

1.3 Mechanoregulation of clathrin-independent endocytosis

1.3.1 Macropinocytosis

Macropinocytosis involves nonspecific uptake of extracellular materials *via* membrane protrusions driven by actin polymerization. The protrusive structures fuse with the basal membrane forming a vesicle of 0.2 to 0.5 μm in size [64]. Membrane ruffling is heavily associated with the initiation of macropinocytosis. Peterson *et al.* showed that lipid raft disruptions caused by mechanical or kinetic factors can lead to the activation of phospholipase D2 (PLD2), which is involved in endocytosis and actin polymerization [65–67]. Subsequently, Loh *et al.* showed that an acute drop in membrane tension by osmotic shock activated PLD2, which in turn led to phosphatidic acid (PA) production, F-actin and PIP_2-enriched membrane ruffling in myoblasts. They identified that F-actin and PIP_2-mediated ruffling initiate macropinocytosis [68]. Further, mechanical stretching of muscle cells led to PA-enriched macropinosomes, which act as a platform for mTOR recruitment and activation [69]. Macropinocytosis has been identified as the preferential

route of uptake for soft particles like hydrogel-based nanoparticles [70,71]. Aspect ratio of the cargo has also been shown to play an important role in macropinocytosis. Mesoporous silica nanoparticle with an aspect ratio of 2.1-2.5 were preferentially internalized *via* small GTPase-dependent macropinocytosis compared to nanoparticles with a higher or smaller aspect ratio [72].

1.3.2 Phagocytosis

Phagocytosis involves ingestion of large particles like bacteria into phagosomes for lysosome-based degradation. Phagocytosis involves extensive mechanosensing, membrane and cytoskeletal remodeling to 'search and destroy' pathogens [5]. This remodeling is a two-phase process depending on the membrane tension and other mechanical characteristics of the cell. In the first phase, polymerization of actin pushes the membrane to extend pseudopods. The second phase is initiated once the membrane reservoirs are depleted causing the membrane tension to increase. This membrane tension increase alters activity of small Rho GTPase Rac1, and 3′-phosphoinositide and cytoskeletal organization. Further, it activates exocytosis of GPI-anchored protein-containing vesicles to replenish membrane area that is necessary to carry out phagocytosis of large particles [34].

Controlling cell shape modulates pro-inflammatory (M1) vs. pro-healing (M2) activation of macrophages. Induction of macrophage elongation by confinement in high aspect ratio microcontact printed islands result in polarization towards an M2 phenotype. This confinement upregulated the effect of M2-inducing cytokines and while downregulating the effect of M1-inducing cytokines [73]. Preventing cell spreading by spatially confining macrophages on micropatterned islands, circular 3D microwells or cell crowding reduces their bacteria uptake and cytokine secretion. This may be due to reduced transcriptional activity of M1 macrophage that is regulated by actin and myocardin-related transcription factor A (MRTF-A) as a result of area

confinement [45]. Further, macrophages were unable to phagocytose higher aspect ratio of filament-formed *E. coli*, as such structures presented limited access of bacteria poles for macrophages to initiate phagocytosis [58].The ability for macrophages to detect variations in ECM stiffness associated with tissue inflammation is necessary for their phagocytic response. Beningo *et al.* showed that Fc-mediated phagocytosis is regulated by the mechanical properties of its target. By microinjecting constitutively active Rac1, phagocytosis of softer particles by macrophages could be activated [74]. Bakalar *et al.* showed that antigen height mediates the phagocytosis of engineered and tumor-specific antigens [75]. Phagocytosis was severely inhibited by antigens that created a separation of more than 10 nm between antibodies and target surface [75]. Scheraga *et al.* showed that a mechanosensitive ion channel transient receptor potential vanilloid 4 (TRPV4), triggered by changes in ECM stiffness due to inflamed or fibrotic lung, mediates lipopolysaccharide-stimulated murine macrophage phagocytosis [47]. Bacterial pathogen-associated molecular pattern molecules (PAMPs), cytokines (IFNγ), substrate rigidity, and stretch *via* actin polymerization and small Rho GTPase activity can control macrophage phagocytosis independently. This suggest a coordinated mechanism to increase macrophage phagocytosis in disease states like pneumonia which is associated with an increase in tissue rigidity and production of PAMPs or inflammatory cytokines [46]. This mechanism likely play an important role in regulating macrophage activity during pulmonary infection and fibrosis [47].

1.3.3 Caveolae-mediated endocytosis

Caveolae-mediated endocytosis uses membrane proteins caveolins (*e.g.*, Cav-1) and cavins to create 50-60 nm sized, sphingolipid and cholesterol-rich flask-shaped plasma membrane pits called caveolae [76]. Caveolae are closely associated with actin stress fibers and are internalized in

response to various mechanical and chemical stimuli [21,77]. Filamin A anchors caveolae to the plasma membrane by linking them to the actin fibers. Loss of cell adhesion induces rapid internalization and trafficking of caveolae to perinuclear compartments [78], specifically to recycling endosomes. This internalization is mediated by the loss of linkage between caveolae and actin fibers due to the rapid protein kinase Cα-mediated phosphorylation of filamin A [79].

Cells respond to increasing membrane tension by flattening or dissembling of caveolae [80–82]. Muscle cells utilize caveolae flattening to protect themselves from membrane rupture due high tension [82]. The enhanced membrane fragility in myotubes of muscular dystrophic patients has been attributed to the absence of caveolae reserve in their muscle cells [82]. Similar to individual caveolae, clusters of caveolae known as caveolar rosettes are stabilized by low tension and destabilized by high tension **(Figure 1.2a)** [83]. It has been shown that plasma membrane wounds induce lysosomal exocytosis and subsequent caveolar rosette formation to seal the membrane [84]. On the other hand, actin fiber anchorage of caveolae inhibits the formation of caveolar rosettes [85]. In response to mechanical stress, cells increase the phosphorylation of Egr1 (early growth response-1) transcription factor and thereby inhibiting its suppression of Cav-1 and cavin-1 genes, which in turn upregulate caveolae biogenesis [86]. Given all these, it is widely accepted that caveolae in the plasma membrane act as a buffer system against rapid membrane tension changes either by flattening of caveolae (during tension increase) or forming caveolae rosettes (tension decrease) [21].

Cav-1 is implicated in the force-induced cytoskeletal reorganization mediated by RhoA [87] and the maturation of contractile smooth muscle cells induced by transforming growth factor TGF-β1 [88]. Cav-1 is also associated with focal adhesion turnover *via* regulation of RhoA [89]. Further, Cav-1-dependent β1 integrin and fibronectin endocytosis mediate fibronectin matrix turnover, pointing towards the role of Cav-1 in ECM remodeling [90]. Low shear stress induces Cav-1

clustering in lipid rafts and co-localization of Cav-1 and membrane type 1-matrix metalloproteinase in invadopodia[91]. Cav-1 activation induces PI3K/Akt/mTOR signaling which in turn promotes motility, invadopodia formation and metastasis of breast cancer cells [91]. Cav-1 also favors cell elongation in three dimensional cultures and metastasis by enabling Rho and actomyosin-mediated matrix reorganization [92]. Given the tight connection of Cav-1 with several key cell signaling pathways, coupled with the mechanoregulation of caveolae assembly/disassembly by mechanical stresses, caveolae are viewed as key structures for cells to rapidly respond to extreme mechanical stresses in the plasma membrane and to changes in ECM due to inflammation and other disease conditions.

1.3.4 Clathrin- and caveolin-independent endocytosis

Cells use multiple endocytic pathways which do not involve clathrin coat formation and caveolae formation. These endocytosis modes have a very high capacity to internalize membrane, thereby making them the rapid responders to abrupt mechanical changes in cells [22,35,93,94]. Clathrin-independent endocytosis (CIE), as these mechanisms are generally known, is further classified based on whether they use dynamin for membrane scission or not. RhoA-mediated endocytosis, fast endophilin-mediated endocytosis (FEME), Shiga toxin-induced tubules, and ARF6-mediated endocytosis are CIEs involving dynamin for mediating membrane scission. Cdc42 dependent endocytosis (clathrin-independent carriers (CLICs) / glycosylphosphatidylinositol- anchored protein (GPI-AP) enriched compartments (GEECs) pathway or CG pathway) and flotillin-mediated endocytosis are CIEs, which do not use dynamin-mediated scission [95]. One of the major CIE pathway, the CG pathway, has been suggested to be involved in the fast response to membrane tension decrease due to its rapid rate of membrane internalization [94,96]. The surface area-to-volume measurement suggests that the CG pathway can turn over the entire plasma membrane of

fibroblasts in 12 minutes [96,97]. This fast membrane recycling by CG pathway coupled with rapid exocytosis is utilized by fibroblasts to regulate membrane area during spreading [98]. Inhibition of the CG pathway was also shown to reduce membrane tension[94]. Vinculin is shown to mediate the membrane tension response of CG pathway by controlling guanine-nucleotide exchange factor GBF1 in the plasma membrane [94]. Inverted BAR protein IRSp53 enables the formation of tubules in the CG pathway by reducing the force needed to sustain tubules [99]. The activity of IRSp53 to enable tubule formation and aid membrane scission in CG pathway is depended on its density and membrane tension [100].

Ca^{2+}-dependent endocytosis is involved in rapid sealing of microbial-toxin induced membrane rupture by internalizing lesions from the plasma membrane [101]. Neuronal synapses use actin and dynamin-mediated ultrafast CIE for recycling synaptic vesicles [29]. Recycling synaptic vesicles is necessary to remove excess membrane from the plasma membrane to maintain optimal tension needed for synaptic vesicle fusion [29,102]. In yeast cells, inhibition of TORC2 controls CIE pathways by modulating membrane tension [103]. Elevated membrane tension upon TORC2 inhibition, inhibits the binding of adaptor proteins Sla2 and Ent1 to actin cytoskeleton as well as hinders the recruitment of Rvs167, a N-BAR protein involved in vesicle fission, to endocytic sites, leading to the downregulation of endocytosis in yeast. Altogether, these findings point to the vital role of CIE pathways in rapid reorganization of the plasma membrane in response to physical stresses and membrane ruptures [104].

1.4 Clathrin-mediated endocytosis

CME involves internalization of cargo by packaging it in 60 - 120 nm sized clathrin-coated vesicles [1]. CME is a well-studied endocytic pathway, fundamental to nutrient uptake,

neurotransmission, signal transduction and intercellular communication [1,4,105]. CME, with clathrin-coated pits (CCPs) as the fundamental functional units, is a multi-step process involving extensive sculpting and reorganization of the plasma membrane. Initiation of CME is triggered by the recruitment of adaptor protein complex AP2 and membrane bending BAR domain and E/ANTH domain proteins [106,107]. The clathrin coat is assembled at the sites of adaptor protein nucleation. Concurrent with cargo recruitment, a CCP matures into a dome-shaped invagination, which is subsequently reorganized to a Ω-shaped pit and cleaved from the membrane to form a clathrin-coated vesicle. The membrane reorganization in CME is regulated by mechanical factors like membrane tension, membrane rigidity and stiffness of the ECM and cargo [9,108]. In the section below, I will examine how different stages of CME, through a CCP's lifecycle from initiation to scission, is modulated by mechanical stimuli.

1.4.1 Initiation

The initiation of CME is marked by the arrival of early endocytic adaptor proteins like AP2 [4]. Although initiation events are generally considered stochastic [109], 'hot spots' for CCP initiation exists at specific regions of cells [110], which can be based on the presence of specific lipid or cargo proteins [1]. Mechanical factors like area of confinement, local membrane tension, and polarity of a cell may play a role in the selective initiation of CME at specific membrane sites [26,32,111,112]. Endocytic proteins like AP2, epsin 1, amphiphysin 1 show preferential recruitment to regions of pre-existing sub-micron curvature. Unsurprisingly, pre-curved membranes show increased rate of endocytic nucleation events [113]. An increase in membrane tension correlates with a reduction in CME initiation density [108]. CME nucleation proceeds only after the recruitment of membrane curving protein above a critical density above which the membrane transitions from a flat to curve morphology, and this critical density is a function of membrane tension [27,33]. Coarse-grained

molecular dynamic simulations show that membrane tension controls the assembly of curvature-generating, BAR domain-containing proteins. Elevated tension inhibits BAR protein oligomerization, N-BAR domain's interaction with membrane and alters the geometry of BAR protein aggregates [114]. Local reduction in membrane tension by myosin-based contraction can accelerate the recruitment of BAR proteins at the leading edge of a polarized cell [115].

Membrane bending proteins can alter the mechanical property of the membrane to achieve membrane curvature [39]. Purified ENTH domain binding to giant unilamellar vesicles (GUVs) causes considerable reduction in area compressibility modulus and the bending rigidity of the membrane [116]. The insertion of helix-0 of ENTH domain into membrane, tubulates membrane at low tension and soften the bilayer at higher tension [116]. Helix insertion reduces the energetic cost of membrane bending and makes tubule formation energetically less costly [116,117]. Consistent with this, osmotic pressure-induced tension enhances the hydrophobic insertion of N-BAR domain of amphiphysin into membrane [118]. This may be due to the increase in density of lipid packing defects, which aid in helix insertion of BAR proteins [119,120]. Further, spontaneous membrane bud formation aided by protein crowding by intrinsically disorder proteins like epsin and AP180 is also controlled by global membrane tension which equilibrate lipid-protein binding energy and membrane free energy [121].

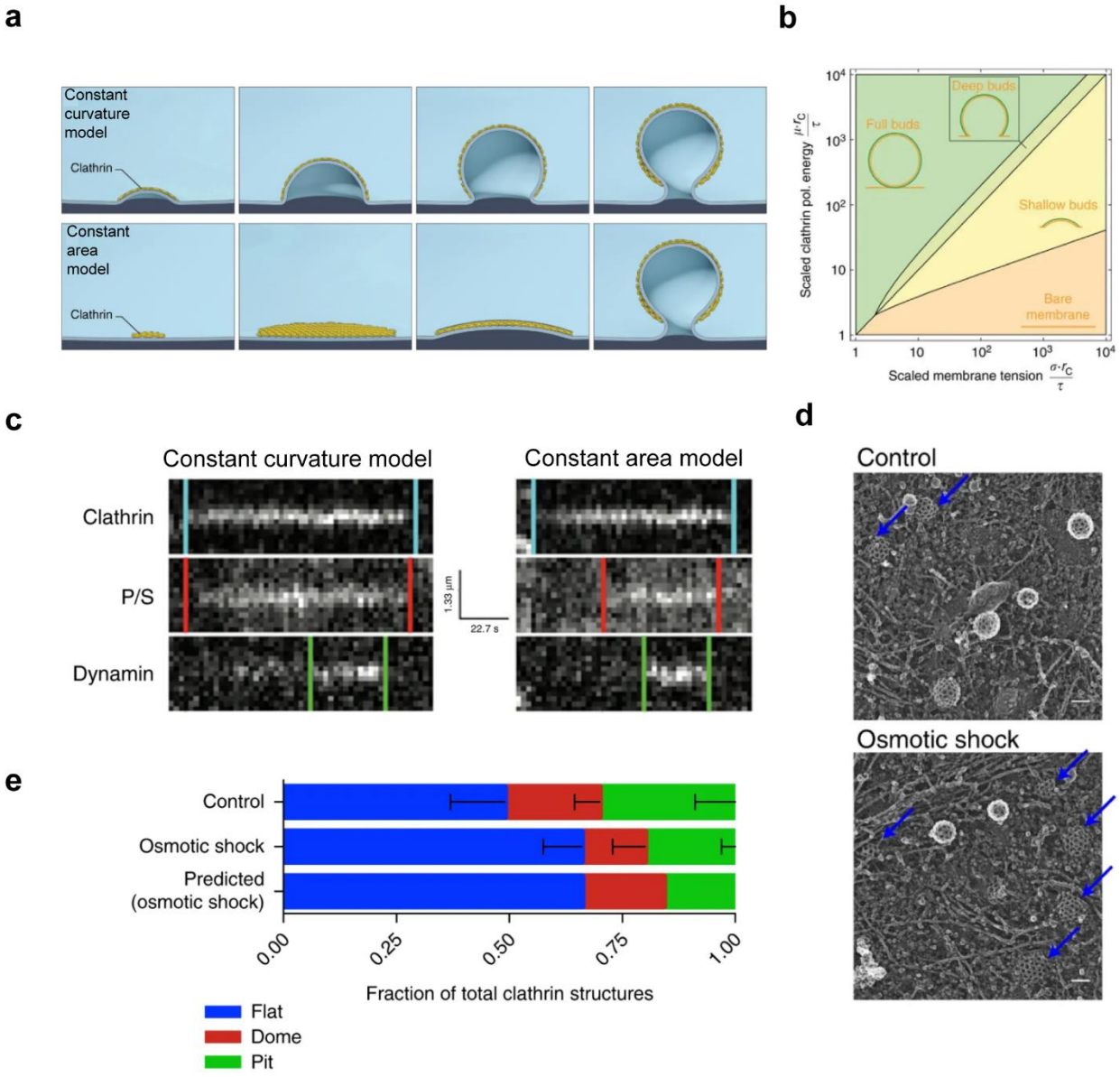

Figure 1.3. **Clathrin bud formation under different tensions.**

a Membrane bending model for clathrin-mediated endocytosis (CME). Constant curvature model (top panel), where membrane bending proceeds with a constant radius of curvature with continuous addition and polymerization of clathrin triskelion. Constant area model (bottom panel), where clathrin triskelion polymerizes into a flat coat then remodels into a coated pit [16]. Reproduced under the terms of the CC BY 4.0 license. Copyright 2018, The Authors, published by Springer Nature. **b.** Distinct mode of membrane bending observed in cells *via* polarized-TIRF. Constant curvature model for membrane bending observed by pol-TIRF (left panel). Clathrin and P/S signals proceed together indicating synchrony of clathrin assembly and curvature. Dynamin recruitment in the end shows the scission of the coated pit. Constant area model for membrane bending

observed by pol-TIRF (right panel). Clathrin signal plateaus prior to the start of P/S signal indicating clathrin assembly began as a flat sheet and subsequent remodeled into a vesicle. Dynamin recruitment in the end shows the scission of the coated pit [16]. Reproduced under the terms of the CC BY 4.0 license. Copyright 2018, The Authors, published by Springer Nature. **c.** Phase diagram of predicted budding state as a function of the scaled membrane tension and scaled clathrin polymerization energy. Four possible states of a single bud are considered in the model: bare membrane with no clathrin binding, shallow membrane with partial budding, hemispherical membrane with partial budding and spherical membrane with full budding [122]. Reproduced under the terms of the CC BY 4.0 license. Copyright 2015, Nature Publishing Group. **d.** Transmission electron microscopy images of clathrin buds and flat coats (pointed by blue arrows) under normal condition and osmotic shock (scale bar: 100 nm) [11]. Reproduced under the terms of the CC BY 4.0 license. Copyright 2018, The Authors, published by Springer Nature. **e**. The proportion of flat and domed structures in normal and osmotic shock condition. Increase in membrane tension *via* osmotic shock increases the proportion of flat assemblies. The predicted proportion of flat and dome structure is shown based on the constant area model [11]. Reproduced under the terms of the CC BY 4.0 license. Copyright 2018, The Authors, published by Springer Nature.

1.4.2 Coat assembly

Clathrin triskelia are recruited directly to adaptor protein nucleation sites to form cage-like clathrin coat [4]. Clathrin polymerization is necessary for the stabilization of the membrane invaginations. The assembly and formation of the coat is regulated by membrane tension and rigidity [9,22]. There exist two competing hypotheses for clathrin scaffolding mechanism. The first model, the constant curvature model, considers the direct polymerization of clathrin coat to curved membrane as the pit increases in size **(Figure 1.3a top)**. A second model, the constant area model, considers clathrin assembly to occur on flat membrane and after the critical density of clathrin coat is reached, the flat assembly reorganizes into a spherical coat while maintaining a constant clathrin coat area **(Figure 1.3a bottom)**.

Membrane tension has an inhibitory effect on clathrin coat polymerization, coat size and shape [32,122]. The shape stability curve of membrane invaginations shows the existence of multiple invagination topologies mediated by membrane tension and protein density [122] **(Figure 1.3b)**. An increase in membrane tension results in premature disassembly of clathrin coat [32,33]. Increasing

membrane rigidity also inhibits clathrin coat formation [33,122]. This is consistent with the early finding that the rate of endocytosis is slower on the apical side of an epithelial layer where the membrane rigidity is elevated [123]. Membrane curvature generation proteins like epsin enable coat formation under higher tension and rigidity [28,122], but the precise mechanism of how epsin achieves this remains unknown. Coarse-grained modeling shows that higher tension stabilizes large, flat clathrin plaques, whereas lower tension leads to smaller budded structures [124]. Flat, flake-like clathrin structures, which are slowly internalized with the help of actin, are found on the basal surface of fibroblasts adhered to solid substrate, whereas small, curved, and pit-like structures with non-hexagonal faces are found on the apical membrane [125]. An increase in substrate rigidity causes the formation of stalled and flat clathrin-coated structures that are mediated by αvβ5 integrin [30]. Although *in vitro* biochemical data on clathrin coat polymerization have favored the constant curvature model [1], the observation of flat clathrin lattices have challenged the canonical constant curvature model. Recent studies based on super-resolution imaging and correlative light electron microscopy have shown evidence for the existence of the constant area model (Model 2) for clathrin coat formation [11,16,126]. Quantification of membrane curvature using polarized TIRF by selectively exciting DiI molecules in vertical (p-pol, P) or horizontal membrane (s-pol, S) during clathrin assembly shows the presence of both modes of coat curvature generation (constant curvature model and constant area model) can occur in the same cell [16] **(Figure 1.3c)**. Constant area model of coat formation by flat-to-dome transition is heavily regulated by clathrin-adaptor ratio and membrane tension. Osmotic shock-induced tension increase inhibits the transition from flat to curved coated structures [11] **(Figure 1.3d, e)**. Factors determining the mode of clathrin coat assembly, like distribution of membrane bending proteins [127], lateral membrane tension [11,122], local

actin polymerization [26,128], and cargo binding [129,130] vary locally in the plasma membrane, leading to the presence of both modes of assembly in cells.

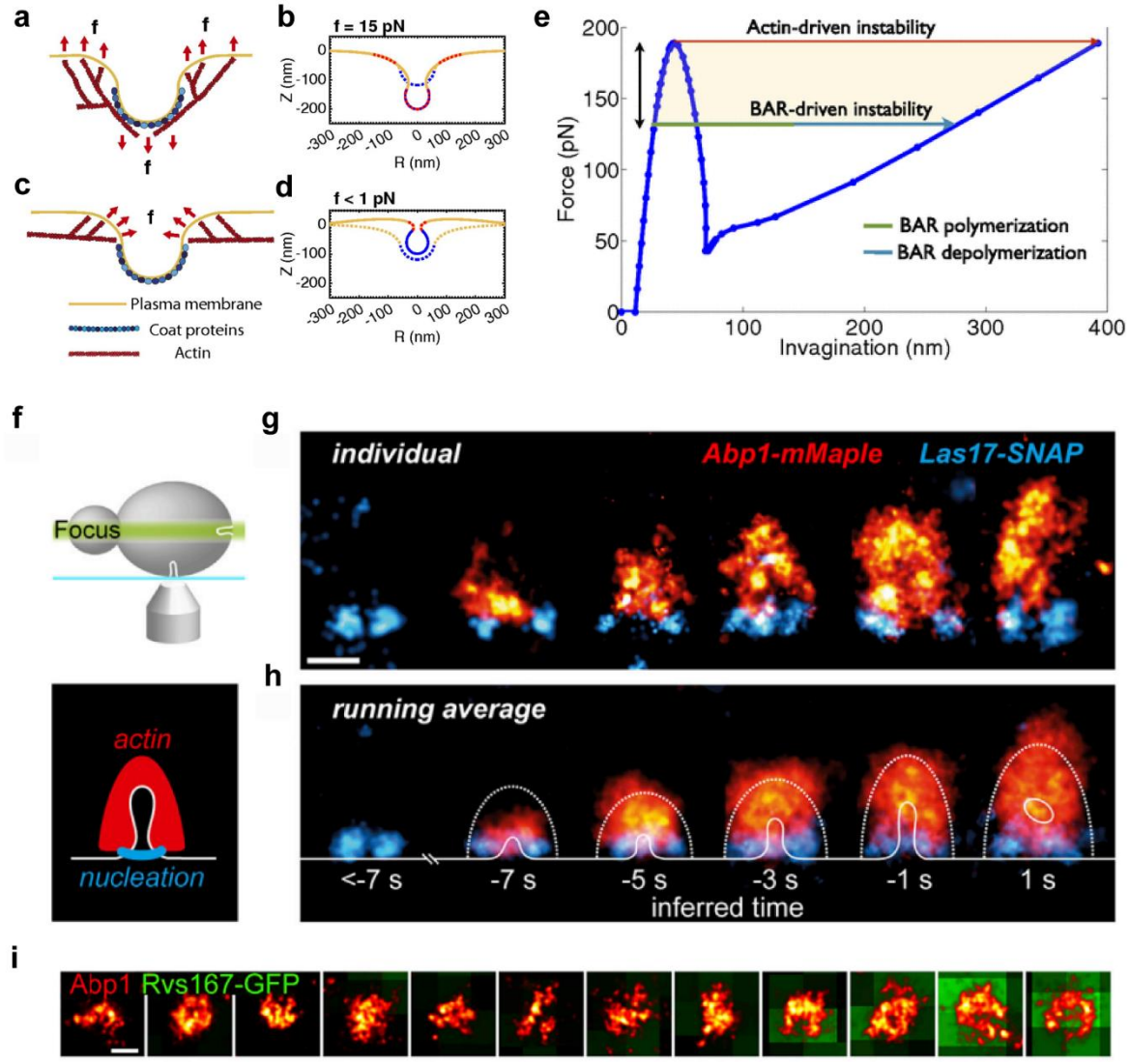

Figure 1.4. Experimental confirmation of U to Ω transition of clathrin-coated pits (CCP) with the aid of actin.

a. Schematic depicting actin polymerization at the base of a CCP with the network attached to the coat, causing a net inward force on the bud. **b.** At constant coat area and spontaneous curvature, force (red dash) of actin polymerization adjacent to the coat drives transition of U-shaped pit (dashed line) to Ω-shaped pit (solid line). The final applied inward force on the bud was f = 15 pN. **c.** Schematic depicting actin assembly at the neck of coated pit directly providing a constricting force. **d.** A constricting force (red dash) of actin polymerization adjacent to the neck of the coat drives transition of U-shaped pit (dashed line) to Ω-shaped pit (solid line). The final applied constriction force on the bud was f < 1 pN[28]. Copyright 2017, Proceedings of National Academy

of Sciences. **e** Synchronous roles of actin and BAR proteins in forming membrane invagination. In the presence of BAR scaffold, a reduced dependence on actin force is required due to a stronger squeezing effect of the BAR scaffold. In the absence of BAR proteins, a tension-dependent critical actin force is needed to induce U to Ω-shape transition [27]. Copyright 2015, Proceedings of National Academy of Sciences. **f.** Schematic of dual-color side view super-resolution images (top panel). The localization of actin and actin nucleating proteins (Wiskott–Aldrich Syndrome protein (WASp): Las17) in CCPs of yeasts (bottom panel). Reproduced under the terms of the CC BY 4.0 license. Copyright 2018, The Authors, published by Cell Press. **g.** Dual-color side-view super-resolution images of Las17-SNAP and Abp1-mMaple at individual endocytic sites. **h.** Running-window averages of Las17 and Abp1 at endocytic sites with overlay of average outer boundaries of the actin network (dotted lines), and average plasma membrane profiles (solid line) (scale bar: 100 nm, $n_{events\ Las17}$ =8599, $n_{events\ Abp1}$ =2849). Images (g) and (h) show the transition of CCPs from U shape to Ω-shape mediated by actin polymerization initiating at the neck of the CCP [131]. Reproduced under the terms of the CC BY 4.0 license. Copyright 2018, The Authors, published by Cell Press. **i.** Actin binding protein 1 (Abp1) imaged by super-resolution imaging is overlaid on diffraction-limited Rvs167-GFP (BAR protein) in yeast showing the aforementioned synchronous effect for vesicle scission in yeast cells. Reproduced under the terms of the CC BY 4.0 license. Copyright 2018, The Authors, published by Cell Press.

1.4.3 Maturation and scission

The clathrin-coat assembly leads to the formation of hemi-spherical CCPs. Transition of hemi-spherical domes (U shape) to closed (Ω shape) pits is necessary for the internalization of cargo molecules. Membrane scission proceeds by assembling dynamin into tight oligomers of initial radius of 10 nm around the neck of a CCP to constrict the neck [1]. Coarse-grained simulations show that at physiologically significant value of membrane tension (0.02 pN/nm), the transition from an open to a closed bud occur spontaneously through a snap-through instability [27,28]. The snap-through instability occurs when a small change in clathrin coat area causes the hemi-spherical bud to abruptly close to a Ω-shaped morphology. At high tension, increasing the coat rigidity and the force from actin polymerization around CCPs together ensure CCPs experience a smooth transition from an open to closed bud morphology without snap-through instability [28] **(Figure 1.4a, b, c, d)**. This is consistent with a previous study where disrupting actin cytoskeleton by Jasplakinolide caused stalling of CCPs in cells under hypo-osmotic shock [26]. The transition of hemispherical bud

to Ω-shaped bud exists over a range of membrane tension, and it is driven by BAR domain proteins and actin cytoskeleton (**Figure 1.4e)**[27]. Super-resolution imaging has enabled the visualization of actin-aided transition of CCPs from open to close buds in yeast cells **(Figure 1.4f, g, h)** [131]. BAR domain proteins also facilitate membrane scission of CCPs. BAR protein scaffold imposes a frictional force on the neck of the membrane invagination, while an external force provided by actin assembly can pull to elongate the invagination. Although CME does not rely on dynamin to mediate membrane scission in yeast, a similar principle applies where the BAR domain of Rvs161/167p stabilizes the neck and induces friction to mediate scission of the membrane **(Figure 1.4i)** [132]

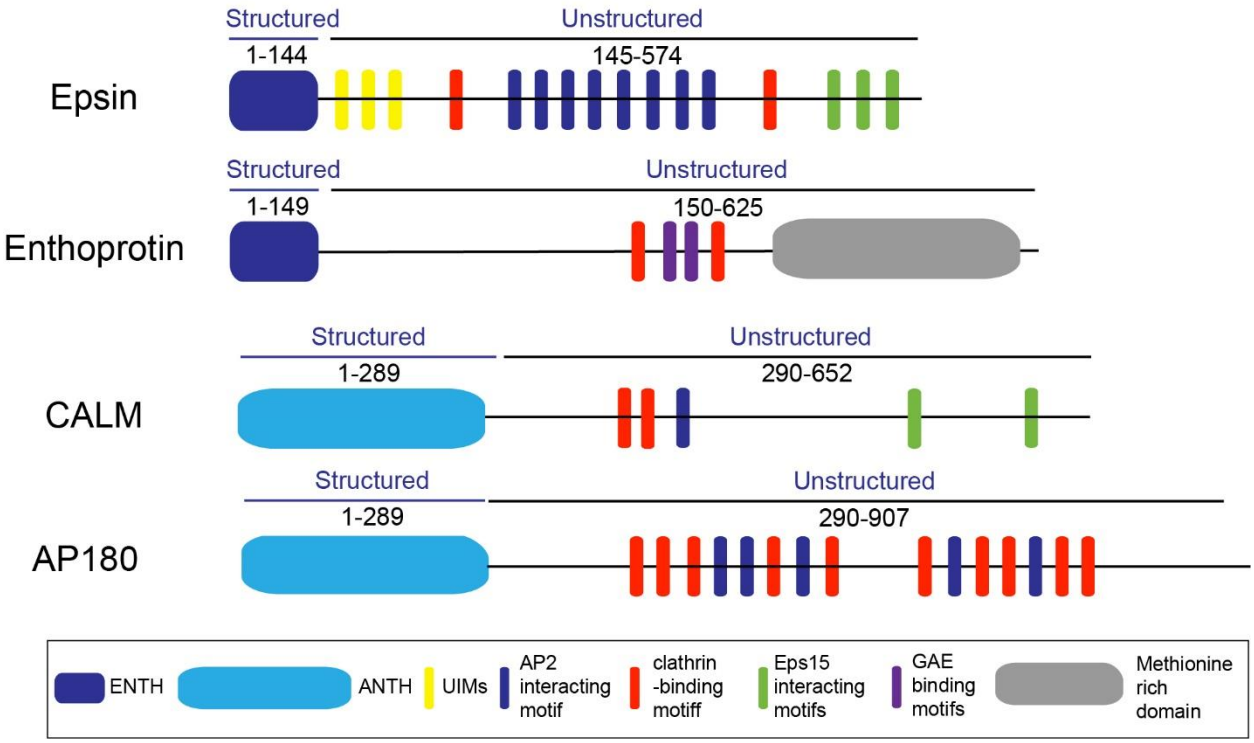

Fig. 1.5 E/ANTH proteins and their domains.

a. Schematic of protein domains of ENTH and ANTH domain proteins epsin, enthoprotin, CALM and AP180 showing the structured ENTH or ANTH domain along with the unstructured regions containing endocytic protein binding sites.

1.4.4 ENTH/ ANTH proteins and their role in inducing membrane curvature in CME

Epsin/AP180 N-terminal homology (E/ANTH) domain proteins is a major protein super family involved in membrane bending at clathrin-coated pit (CCP) budding[39,133] (**Figure 1.5**). Epsin N-terminal homology (ENTH) domain is an evolutionary conserved protein domain associated with CME initiator proteins[133,134]. AP180 N-terminal homology domain is a structurally similar domain to ENTH also associated with CME adaptor proteins. In mammals, ENTH proteins include Epsin 1, Epsin 2, Epsin 3 as well as Enthoprotin and, ANTH proteins include AP180, CALM, HIP1 and HIP1R[133]. ENTH domain upon binding to inositol phospholipids (PtdIns(4,5)P_2) forms an amphipathic helix referred to as α0, which is hypothesized to insert into the bilayer initiating membrane bending[133–135].The N-terminal 1-18 residues in ANTH domain of CALM forms an amphipathic helix binding to inositol phospholipids (PtdIns(4,5)P_2)[127]. The c-terminus of both epsin family and AP180 family have short peptide motifs and protein domains that interact with proteins in clathrin coat complex[133]. These c-terminus regions of Epsin/ AP180 are long natively unstructured regions called intrinsically disordered protein (IDP) domains and have been shown to cause protein crowding[17,18]. In vitro studies have shown that the steric repulsion arising from protein crowding of Epsin/AP180 on the membrane can also drive membrane curvature formation. It is still debated which mechanism plays a stronger role in bending lipid bilayer.

The proteins involved in endocytosis and mechanical stimuli that can regulate these proteins are summarized in Table 1.1.

Endocytosis process	Associated protein or protein complex	Mechanical stimuli	Response to mechanical stimuli	Reference
Macropinocytosis	Rac1 and CDC42	Aspect ratio of cargo	Differentially uptake NPs of aspect ratio 2.1-2.5, by forming filopodia with activation of the actin cytoskeleton.	[72]
	Phosphatidic acid	Membrane stretching	Enrichment of PA in macropinosomes, which act as a platform for mTOR recruitment and activation	[69]
	PLD2	Membrane tension	Activation of PLD2 lead to phosphatidic acid (PA) production, F-actin and PIP2 enriched membrane ruffling in myoblasts	[68]
Phagocytosis	Rac1	Substrate stiffness and membrane tension	Control actin reorganization for cup formation and activate phagocytosis of softer particles.	[46,74]
	Cdc42	Substrate stiffness	Promote actin organization and increase cell elasticity	[46]
	Myocardin-related transcription factor-A (MRTF-A)	Area confinement	Down regulated lead to reduction in M1 macrophage transcription	[45]
	Transient receptor potential vanilloid 4	Substrate stiffness	Extracellular matrix stiffness in the range of inflamed/fibrotic lung promotes TRPV4 activity leading to anti-inflammatory phenotypic change and increase in phagocytic activity	[47]

	(TRPV4) ion channel			
Caveolae-mediated endocytosis	Cav-1	Low shear stress	Cav-1 clustering in lipid rafts and activation of PI3K/Akt/mTOR signaling	[91]
	Cav-1 and Cavin-1	Membrane stretch	Reduction in Cav-1 Cavin 1 interaction by membrane stretch causes caveolae disassembly. Cavin-1 become cytosolic	[82]
	Filamin A	Loss of cell adhesion	Phosphorylation of filamin A, causes loss of linkage between caveolae and actin fibers.	[79]
Clathrin/caveolae independent endocytosis	GPI-anchored proteins	Membrane tension	Drop in tension upregulate CLIC/GEEC pathway and uptake of GPI-anchored protein	[94,97]
	Vinculin	Membrane tension	Inhibit CLIC/GEEC pathway endocytosis to reduce tension	[94]
	TORC2	Membrane tension	Drop in tension causes clustering of TORC2 to PtdIns(4,5)P2-enriched PM domains and induce CIE	[103]
Clathrin-mediated endocytosis	Clathrin	Membrane tension	Reduction in recruitment	[32]
	Actin	Membrane tension	Actin polymerization enable transition of open CCP to closed CCP prior to scission at high tension	[26]
	ENTH domain proteins	Membrane tension	H_0 helix insertion into membrane causes tubule formation at low lateral tension, whereas it reduces membrane rigidity at higher membrane tension	[116]
	N-BAR proteins	Membrane tension	Oligomerization of bar proteins and their interaction with membrane is inhibited by tension	[114]

Table 1.1: Mechanome of endocytosis.

Important mechanosensitive proteins involved in different endocytic pathways. A brief description of mechanical stimuli and response of each protein to that stimulus is provided.

1.5 Dissertation outline

Using epsin as a model of membrane bending proteins, in the following chapters I will investigate how membrane bending in clathrin-mediated endocytosis is regulated by mechanical stimuli. In Chapter 2, I will discuss the role of membrane tension in recruiting epsin into CCPs. Further, I will also present data supporting the presence of tension-sensing alpha helix in structured ENTH region of epsin. In Chapter 3, I will present the role of epsin specifically its disordered domains in stabilizing productive CCPs at high membrane tension. Together from the data presented in Chapters 2 and 3, I propose the model of epsin supporting CME using the complementary action of ENTH and IDP domains. In Chapter 4, I will describe the role of epsin in influenza virus uptake via CME. I will specifically provide evidence into how physical parameters of the virus cargo enable the selective recruitment of epsin into IAV-containing CCPs. Finally, in Chapter 5, I will summarize the important findings from the work and explore the future directions for mechanotransduction of endocytosis.

Chapter 2 Membrane Bending Protein Epsin Mediates Membrane Tension Dependent Recruitment into Clathrin-Coated Structures via Amphipathic Helix Insertion.

The results of this chapter were published in part in Communication Biology (2020). J.G.J., A.A., and A.P.L. conceived the study, J.G.J., C.O., A.A., and A.P.L. designed the experiments, J.G.J. and V.Y. performed the experiments, C.O. carried out the molecular dynamics simulation, J.G.J., A.A., and A.P.L. wrote the paper. All authors commented on the paper and contributed to it.

2.1 Abstract

Membrane tension plays an inhibitory role in clathrin-mediated endocytosis (CME) by impeding the transition of flat plasma membrane to hemispherical clathrin-coated structures (CCSs). However, CME is not completely halted in cells under high tension conditions. Here we find that epsin, a membrane bending protein which inserts its N-terminus H_0 helix into lipid bilayer, supports the nucleation of CCSs at high tension. The recruitment of epsin increases in CCSs in cells with elevated membrane tension, generated either by increasing the area of cell spreading or by osmotic shock. H_0 helix in the ENTH domain of epsin enables its recruitment prior to clathrin to CCP nucleation sites. This discovery is supported by molecular dynamic simulation of the epsin N-terminal homology (ENTH) domain that becomes more structured when embedded in a lipid bilayer. Cells expressing ENTH-deleted epsin no longer have elevated

recruitment of epsin at high tension. The H_0 alpha helix in ENTH was responsible for the loss of tension sensitivity. Together, these findings lead to the conclusion that H_0 alpha helix in ENTH domain of epsin acts as a tension sensor which mediates the tension dependent recruitment of epsin into CCSs.

2.2 Introduction

Clathrin-mediated endocytosis (CME) involves the internalization of cargo by sculpting plasma membrane into 60 -120 nm sized buds, supported by a clathrin protein coat[1]. CME is a well-studied endocytic pathway present in organisms at all developmental stages[1,4,14,105]. It plays a critical role in nutrient uptake, intracellular trafficking, and signal transduction[1,4]. CME is a multi-step process involving (i) initiation of membrane budding with adaptor proteins and membrane bending proteins[39,107,136] (ii) clathrin coat formation[11,16] (iii) maturation of coated pits[26–28], and (iv) dynamin-mediated scission of the buds[1,4,136]. Progression of CME involves extensive deformation of flat plasma membrane to Ω-shaped pits[1,26] which require the activity of dedicated membrane bending proteins.

Epsin/AP180 family is a major family of proteins involved in membrane bending during the initiation of CME[39,134,137]. Epsin, a prominent member of the family, is known to insert its N-terminus amphipathic helix (H_0 helix in epsin N-terminus homology (ENTH) domain) into the bilayer with a wedging effect after binding to PIP_2 to initiate membrane bending[134]. *In vitro* studies have shown that insertion of purified ENTH into giant unilamellar vesicles (GUVs) reduces membrane rigidity and area compressibility modulus of the lipid bilayer[116]. Further, recruitment of ENTH softens the bilayer at high tension and initiates tubulation at low tension[118]. ENTH is shown to recruit selectively to highly curved surface of cylindrical membrane tethers held at different tension[138]. An increase in lipid packing defects at high tension may be key in aiding helix

insertion at high tension from theoretical studies[119,120]. These evidence points to the existence of a tension-sensitive recruitment mechanism of ENTH domain-containing proteins. I hypothesize that these endocytic membrane bending proteins possess the ability to sense membrane tension and elevate their recruitment to plasma membrane to facilitate clathrin-coat budding at elevated tension. There exists an interplay between membrane tension and peripheral protein density that mediates membrane deformation[33]. However, there is still ambiguity in the exact mechanism of ENTH binding at different tensions, and a lack of experimental evidence for tension-mediated recruitment of epsin to clathrin coat nucleation sites in cells. In this chapter, I used the combination of total internal reflection fluorescence (TIRF), mechano-manipulation techniques, automated image analysis, and molecular dynamics (MD) simulation to investigate the tension-responsive recruitment of epsin into clathrin-coated structures (CCSs). I demonstrated that the recruitment of epsin increases with membrane tension in CCSs. Further, using MD simulations and experiments involving epsin mutants, I deciphered the role of H_0 helix in tension sensing and the molecular mechanism of tension-mediated recruitment of epsin.

2.3 Materials and Methods

2.3.1 Cell culture

Retinal pigment epithelial (RPE) cell was a gift from Sandra Schmid (UT Southwestern Medical Centre). The cells were maintained in Dulbecco's Modified Eagle Medium with nutrient mixture F-12 (DMEM/F12) supplemented with 10% (v/v) fetal bovine serum (FBS) and 2.5% (v/v) penicillin/streptomycin at 37^{o}C and 5% CO_2.

2.3.2 Generation of epsin EGFP and EGFP epsin lentiviral constructs

All constructs generated for this work have been sequenced for accuracy. EGFP epsin from pMIEG3 vector (gift from Sandra Schmid, original construct from JoAnn Trejo, UCSD) was amplified with the following primers (Integrated DNA Technologies Inc.) and cloned into pLVX puro vector, using BsrGI and Xbal digestion: Forward primer - 5'-ATAATATGTACAAGTCCGGACTCAGATCTC - 3'; Reverse primer - 5' – GCGGCGTCTAGATTATAGGAGGAAGGGGTT - 3'. Epsin is amplified from pLVX puro vector, using the following primers and cloned into pLVX EGFP puro vector, using XhoI and EcoRI digestion to create epsin EGFP construct: Forward primer 5' – CATCATCTCGAGGCCACCATGTCGACATCATCGCTG - 3'; Reverse primer - 5'-ATAATAGAATTCTCCACTTCCACTTCCACTTCCTAGGAGGAAGGGGTT -3'.
Both constructs were transformed into competent *E. coli* cells (New England Biolabs Inc.) and selected using antibiotics (Ampicillin).

2.3.3 Generation of epsin ΔENTH mutant constructs

Epsin mutant constructs were generated successively by mutagenesis using Q5® Site-Directed Mutagenesis Kit (New England Biolabs Inc.). ENTH domain of epsin was removed using following primers to generate epsin Δ ENTH EGFP: Forward primer 5'-GCCCACGCGCTCAAGACC -3'; Reverse primer 5'- CATGGTGGCCTCGAGATCTGAG -3'. Unstructured IDP region of epsin was removed using following primers to generate epsin ΔIDP EGFP: Forward primer 5'- GGAAGTGGAAGTGGAAGTGGAGAATTCG-3'; Reverse primer 5'- GCGCTCCTCCCGAAGCCG-3'. H_0 helix in ENTH domain of epsin was substituted to histidine using following primers to generate epsin mut-H_0 EGFP: Forward primer 5'-

CACCACCACAACTACTCAGAGGCAGAGATC -3'; Reverse primer 5'-ATGATGATGTGTCGACATGGTGGCCTC -3'. PIP_2 binding site in H_0 helix of ENTH domain was mutated from RRQMK to SSQMS using the following primers to generate epsin mut-PIP_2 EGFP: Forward primer 5'- GATGAGCAATATCGTCCACAACTACTC -3'; Reverse primer 5'-TGGCTGGACAGCGATGATGTCGACATG-3'. All mutant constructs were transformed into competent *E. coli* cells (New England Biolabs Inc.) and selected using antibiotics (Ampicillin).

2.3.4 Lentivirus transduction

Lentiviral vectors encoding epsin or epsin mutants were generated by transfecting 70% confluent HEK 293T for 24 h with a plasmid cocktail. The plasmid DNA cocktail contained 1.875 µg psPAX2, 625 ng pMD2.G, 2.5 µg pLVX vector diluted in 3 mL Opti-MEM (Thermo Fisher) containing 15 µL Lipofectamine 2000 (Thermo Fisher) and 5 mL of DMEM media with 10% FBS (v/v). The plasmid cocktail was replaced with fresh DMEM media containing 10% FBS after 24 h. The supernatant was harvested after 48 h, filtered through 0.3 µm sterile filter and flash frozen using liquid nitrogen.

2.3.5 Stable cell line generation

RPE cells stably expressing EGFP-tagged epsin or epsin mutant and red fluorescent protein (mCherry)-tagged clathrin light chain a (mCherry-CLC) were generated in a two-step process. RPE cells were transduced with retroviruses (encoding mCherry-CLC) in a pMIEG3 vector produced by the UM vector core, followed by FACS sorting (UM Flow Cytometry core) to generate stable RPE cells expressing mCherry CLC. RPE cells expressing mCherry CLC were

further infected with lentivirus encoding EGFP-epsin or epsin mutants followed by antibiotic selection (Puromycin) to generate double stable RPE cells.

2.3.6 Cell spreading on fibronectin islands

Polydimethoxysiloxane (PDMS) stamps with square shapes of size 25 μm and 32 μm were created from a silicon master mold made by using soft lithography. Sylgard-184 elastomer and curing agents (Dow Corning, Midland, MI) were mixed at a ratio of 10:1 (w/w) and casted over the silicon mold and cured at 60 °C overnight. Fibronectin (Sigma) solution (40 μg/ml) was added onto the stamps and incubated for 1 hour at room temperature. The stamps were blown dry using filtered air and placed in conformal contact with UV-ozone-treated PDMS-coated coverslip. Coverslips were spin-coated with a layer of PDMS diluted in hexane (1:20) at 5,000 rpm for 2 minutes. PDMS-coated coverslips enable efficient transfer of stamped proteins. Immediately after stamping, the coverslip was passivated with 0.1% (v/v) Pluronic-F127 (Sigma) for 1 hour, followed by extensive washing with PBS. RPE cells were seeded on the coverslips and allowed to selectively adhere to the square patterns. After 1 hour of seeding, media was changed to remove non-adhering cells. The adherent cells were allowed to fully spread for 5 hours, followed by TIRF imaging.

2.3.7 Osmotic shock

The RPE cells were imaged in three media having different osmolarities: (i) hyper – 440 mmol/kg, (ii) iso – 290 mmol/kg, (iii) hypo – 220 mmol/kg) were used. Hyper-osmotic solution was prepared by adding 150 mM sucrose to phenol red-free DMEM containing 2.5% FBS. Iso-

osmotic solution was DMEM media with 2.5 % FBS. Hypo-osmotic solution was prepared by adding deionized water containing 2.5% FBS to DMEM media containing 2.5% FBS in 1:3 ratio. All media osmolarities were checked on a Vapro osmometer. The cells were imaged between 5 minutes and 35 minutes of adding the different media.

2.3.8 Confocal microscopy

The 3D profiles of cells subjected to different osmotic conditions were imaged using Olympus-IX81 microscope with spinning disk confocal scanner unit (CSU-X1; Yokogawa, Japan), EMCCD camera (iXon X3; Andor, South Windsor, CT), 60× objective (NA = 1.42). A z-step size of 0.2 µm was used. EGFP was used as volume marker. The 3D reconstruction was performed using 3D projection plugin in ImageJ.

2.3.9 Micropipette aspiration

Variation in membrane tension due to osmotic shock was quantified by using micropipette aspiration. Glass micropipettes of inner diameter of ~5 µm were fabricated by pulling borosilicate glass pipette (BF100-50-10; Sutter Instrument) using a micropipette puller (Sutter Instrument). The micropipette was attached to a custom-made stage with pipette holder assembly (MI-10010; Sutter Instrument). An open chamber was made on coverslip seeded with RPE cells using VALAP sealant. The cells were subjected to osmotic shock, using the aforementioned method. The micropipette was made into contact with the cells with the aid of brightfield imaging using an inverted microscope (Nikon TiS) equipped with 20 x objective and a CCD camera (CoolSNAP MYO). A negative hydrostatic pressure of 2.156 kPa was applied to the cell to aspirate the plasma

membrane of cells into the pipette. The ratio of equilibrium protrusion length of membrane (L_p) vs inner radius of pipette was measured for different osmotic conditions.

2.3.10 Live cell imaging *via* total internal reflection fluorescence (TIRF) microscopy

RPE cells expressing the constructs of interest were plated on a coverslip at a low concentration (~ 1.7 x 10^5 cells per 22 x 22 coverslip) and allowed to spread for 12 to 16 hours. TIRF microscopy was performed using a Nikon TiE-Perfect Focus System (PFS) microscope equipped with an Apochromat 100X objective (NA 1.49), a sCMOS camera (Flash 4.0; Hamamatsu Photonics, Japan), and a laser launch controlled by an acousto-optic tunable filter (AOTF). Cells were imaged at 2 s intervals (100 ms exposure) for 5 min at 37 ^{o}C with dual-color excitation of 488 nm and 561 nm lasers (Coherent Sapphire).

2.3.11 Image analysis for CCS dynamics

Single-particle detection, tracking, and lifetime analysis of CCSs from TIRF-M movies were accomplished using custom-written software in Matlab (MathWorks Inc.) as previously described and validated by Aguet et al[15]. Briefly, Gaussian mixture model fitting was used to detect and localize CCSs. mCherry clathrin channel was assigned as the primary detection channel for CCSs detection and EGFP as the associated secondary channel. Then, CCS tracking was performed using μ-track package[139] with a gap-closing feature, which generates trajectories of CCSs by linking the corresponding CCSs in consecutive frames. The intensities of the images were background-corrected along with photo-bleaching correction between time steps. CCSs with lifetime less than 10 s were considered as transient structures and removed from later analysis. Similarly, CCSs with lifetime greater than 120 s were considered as stalled and removed from

downstream analysis. To further filter out the transient structures on the membrane, I also removed structures whose maximum intensity was below an intensity threshold, which was set based on the maximum intensity in the first 6 s of all the CCSs. I generated the lifetime and intensity data for CCSs under two categories (i) CCSs containing EGFP-epsin and (ii) CCSs not containing EGFP-epsin. These were further classified into six cohorts according to their lifetimes (cohorts 10–18, 20–38, 40–58, 60–78, 80–98, and 100–120 s). Within each cohort, the software first realigned and averaged the first time point of intensity time course, yielding the"appearance-aligned" average. The time course was then aligned to the last time point and averaged, yielding the "disappearance-aligned" average. The global average was calculated as the weighted appearance and disappearance-aligned average, weighted towards appearance-aligned trace at the beginning and disappearance-aligned trace in the end. The plateau intensity was calculated as 95% of the maximum intensity values in the intensity profile of a cohort. The proportion of CCSs at each lifetime from 10 to 120 s for each group of cells to obtain the lifetime distribution. Initiation density representing how frequent CCSs appear for a given unit area per unit time was calculated by dividing the median number of the newly appearing CCSs in each frame by the adhesive area of the cell and the interval (1/30 min). Intensity analysis was performed as described previously. For quanitification of early arrival of epsin, aforementioned analysis was repeated with EGFP as the primary detection channel and mCherry as the associated secondary channel.

2.3.12 Molecular dynamic simulations

The MD simulation systems were composed of a bilayer with an ENTH domain of epsin (PDB number 1H0A[134]), a PIP_2 molecule and 99 POPC lipids in the top leaflet and 100 POPC molecules in the bottom leaflet. In addition, the solution consisted of TIP3 (an all-atom model of water) water

molecules with 0.15 mM KCl. The simulations were performed in GROMACS using 303.15 K and 1 bar using CHARMM36 force field[140].

The file taken from the protein data bank contained an ENTH domain of epsin and a PIP_2 head in the inserted configuration. The head group was replaced with the entire lipid preserving the position and original orientation of the head group. Then, the POPC molecules were inserted in a grid pattern in order to construct the bilayer. Finally, the solution with the corresponding KCl concentration was added. All the files detailing the molecule and the equilibration procedure were obtained from CHARMM GUI website[141].

In order to compute different positions of ENTH with respect to the membrane, I pulled the protein sequentially starting from the inserted configuration by imposing a restraining force on the center of mass of the protein. Additional restrains were applied to the PIP_2 lipid to prevent it from leaving the membrane. The pulling proceeds until the protein is not in contact with the membrane. All protein configurations were given an initial equilibration time of 70 ns and a production run of 150 ns.

The secondary structure analysis tool of VMD[142] was applied on the last 100 ns of production run to obtain the secondary structure for each residue in a given frame. The helicity plot was subsequently created by calculating the ratio of frames classified as a helix divided by the total number of frames for each residue.

The area plot for the inserted proteins were obtained using g-lomepro[143]. I used 100 ns production run after an initial equilibration of 100 ns. Since the protein has no restrain of movement along the plane of the bilayer during the simulation, the frames had to be centered around the H_0 helix center of mass.

2.3.13 Statistics and Reproducibility

For intensity, lifetime and initiation density data, the statistical significance was verified by one-way ANOVA test. Subsequently, Bonferroni and Holm multiple comparison test was performed post-hoc between data while considering individual pairs to determine the *p*-values. *, **, and *** was assigned to $p < 0.05$, $p < 0.01$ and $p < 0.001$ respectively.

The experiments were performed at least three times with data collected from multiple cells in each replicate, unless specified otherwise. Number of cells considered for the analysis along with the number of clathrin-coated pit tracks is provided in the corresponding figure captions.

2.4 Results

2.4.1 Epsin recruitment increases as resting membrane tension increases

Epsin is an endocytic adaptor protein recruited to the plasma membrane during initiation of CME to aid in membrane curvature generation[134]. The ability for pits to maintain stable curvatures until they reach maturation is essential for successful completion of a CCS lifecycle[26].

Membrane tension is shown to counteract the stabilization of coated pits by increasing the energy requirement to form a pit[27]. To investigate whether epsin recruitment can counteract varying membrane tension, I manipulated resting or acute membrane tension of RPE cells co-expressing epsin EGFP and mCherry CLC by controlling cell spreading or by applying osmotic shock, respectively.

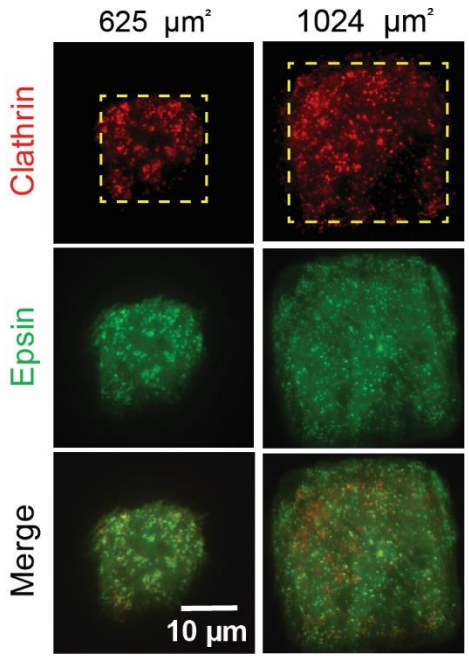

Figure 2.1 RPE cells expressing epsin EGFP and mCherry CLC spread on fibronectin square islands of size 25 and 32 μm.

The resting membrane tension is higher for 32 μm islands.

Resting tension of an adherent cell is related to the membrane tension exerted when the cell is fully spread[144,145]. The resting membrane tension of the cells was controlled by restricting cell spreading on microcontact-printed fibronectin islands of area 625 μm^2 or 1024 μm^2 **(Figure. 2.1)**. Cells spread on a larger area experienced higher membrane tension[32,144]. Using dual color TIRF imaging and an automated algorithm[15], I detected and tracked CCSs and quantified the lifetime, composition (whether both epsin and CLC are present or not), and intensity of fluorescently tagged epsin (EGFP) and CLC (mCherry) in CCSs. Cells imaged had similar expression levels of fluorescent proteins (epsin EGFP and mCherry CLC) between fibronectin islands of area 625 μm^2 or 1024 μm^2 (**Figure. 2.2a**). The intensity traces of CCSs belonging to 60-78 s lifetime cohort showed that the intensity of EGFP epsin is higher in highly spread cells, suggesting epsin recruitment increases with an increase in resting tension **(Figure. 2.2b)**. Interestingly, epsin intensity is already elevated at time 0 when clathrin detection began, suggesting epsin EGFP recruitment may precede clathrin recruitment.

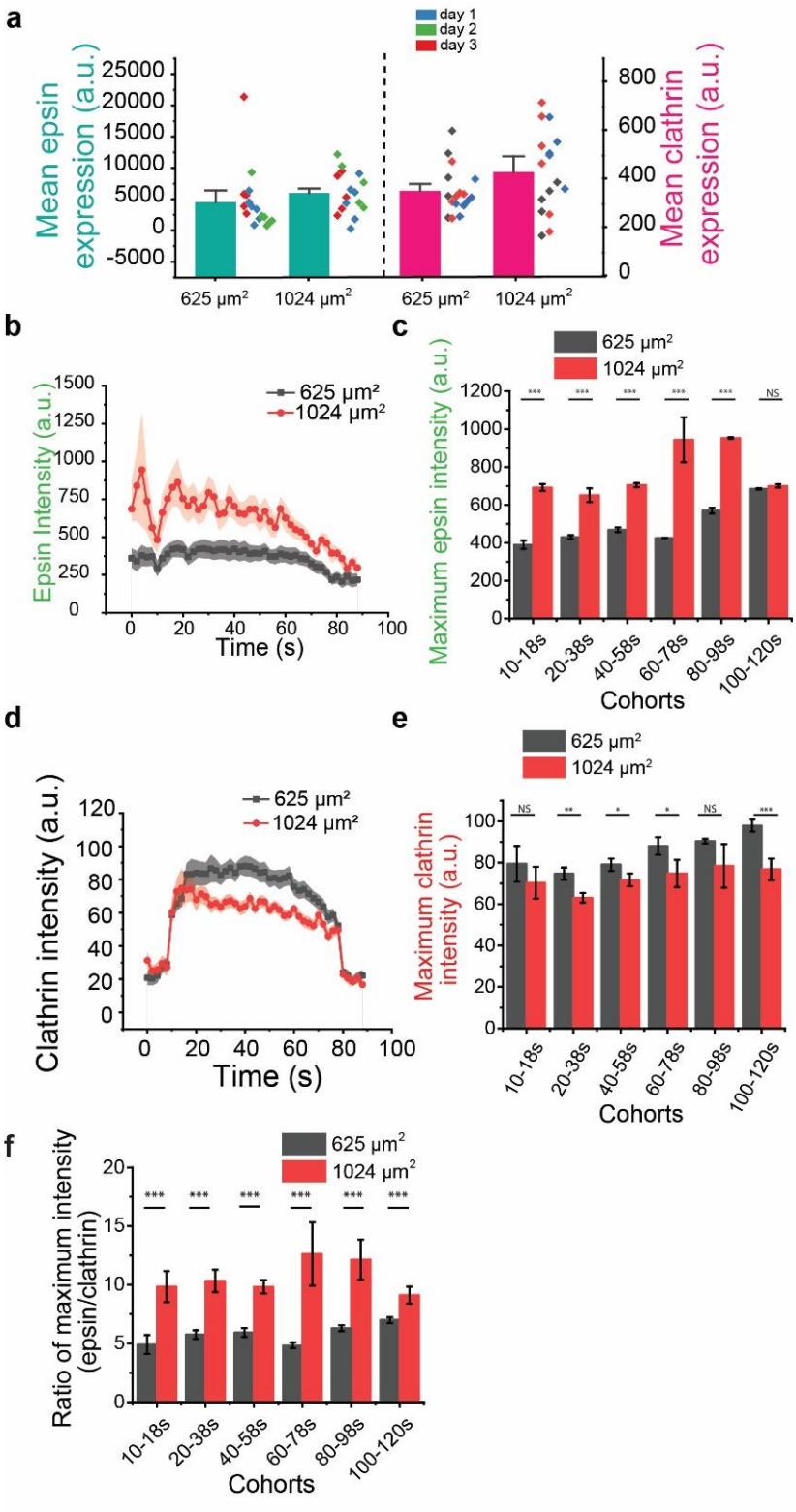

Figure. 2.2 Epsin recruitment increases as resting membrane tension increases.

a. The average bulk expression of epsin EGFP and mCherry CLC in RPE cells used for microcontact printing experiments. Different colored points denote the day of experiment. **b.** The average intensity trace of epsin on 25 µm (black) and 32 µm (red) islands for CCSs with 60 -78 s lifetime. **c** The average plateau intensity of epsin across different CCS lifetime cohorts for cells on 25 µm (black) and 32 µm (red) islands. **d**. The average intensity trace of clathrin in 25 (black) and 32 µm (red) islands for epsin-positive CCPs with 60 -78 s lifetime. **e**. The average plateau intensity of clathrin across different epsin-positive CCP lifetime cohorts. **f**. The ratio of maximum intensity of epsin EGFP and mCherry clathrin across different epsin-positive CCP lifetime cohorts for microcontact printing experiment. For a, b, c, d, e N_{cells} for 25 µm square and N_{cells} for 32 µm square are 18 (N_{tracks} = 17534) and 19 (N_{tracks} = 30188), respectively. The error bars denote standard error. NS denotes not significant. *, **, *** represent $p < 0.05$, $p < 0.01$ and $p < 0.001$, respectively.

Further, the average plateau intensity (i.e., the maximum intensity during a coated pit's lifetime) of epsin in other lifetime cohorts (from 10-18 s to 80-98 s) also showed a higher recruitment of

epsin to CCSs in more spread cells in comparison with the less spread cells **(Figure. 2.2c)**. In contrast, the intensity of mCherry CLC in the 80-98 s lifetime cohort and other lifetime cohorts had a small reduction as resting tension increased (**Figure. 2.2d and Figure. 2.2e**), in agreement with a previous finding[32]. The ratio of epsin to clathrin also increased as the area of fibronectin islands increased **(Figure. 2.2f).** Together, these results indicate that epsin recruitment per clathrin in CCSs increases with increasing resting tension.

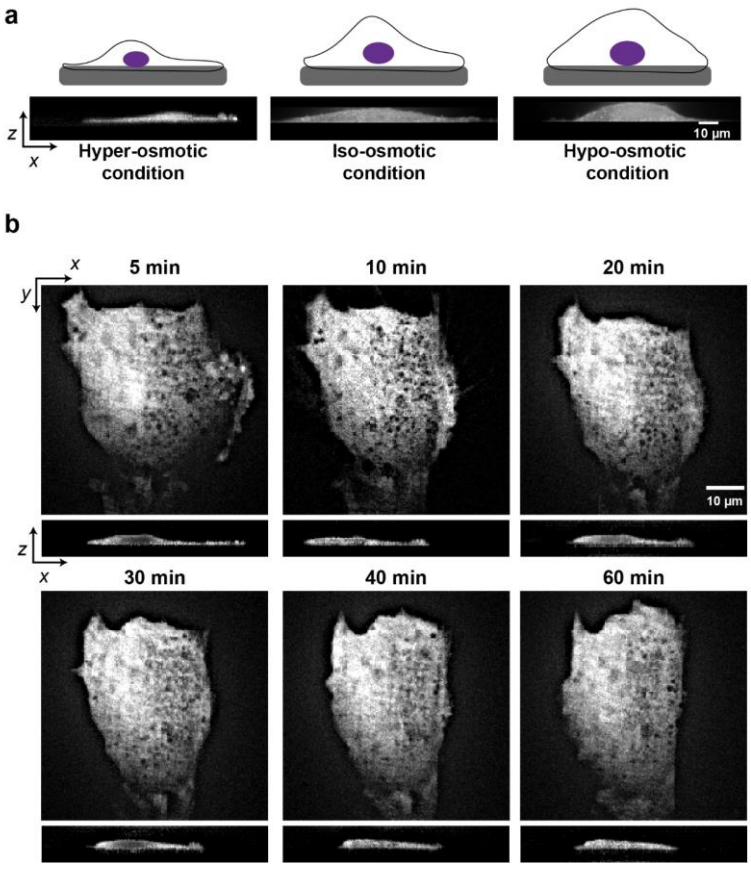

Figure. 2.3. Osmotic shock experiment.

a. Osmotic shock experiment for acute tension drop and spike, as described in the Materials and Methods. Representative confocal cross section images reconstructed from 3D image stacks of cells under hyper-, iso- and hypo-osmotic conditions. **b.** Representative images showing the change in adhesion area and cross section of RPE cell expressing EGFP with time after hypo-osmotic shock.

2.4.2 Epsin recruitment increases as acute membrane tension increases

To investigate whether epsin shows a similar recruitment characteristic in response to acute tension changes, I used osmotic shock to induce acute tension changes in RPE cells. Hyper- and hypo-osmotic shock led to a reduction or increase in cell volume, as evident from 3D cross section of the cells reconstructed from confocal

z stacks **(Figure 2.3a)**. Osmotic shock in cells resulted in retraction of adhered plasma membrane from the cover slip to compensate for the increase in membrane tension and cell volume thereby maintain the homeostasis of the cell membrane (**Figure 2.3b**). Hence, all the imaging experiments were performed in the window between 5 min and 30 min to capture the effect of increased membrane tension before cell recover from osmotic shock by retracting adhered membrane. Micropipette aspiration assay performed in this time interval revealed that membrane aspiration into micropipette reduced from hyper- to iso- to hypo-osmotic condition **(Figure 2.4a-c)**, similar to what was previously reported[146].

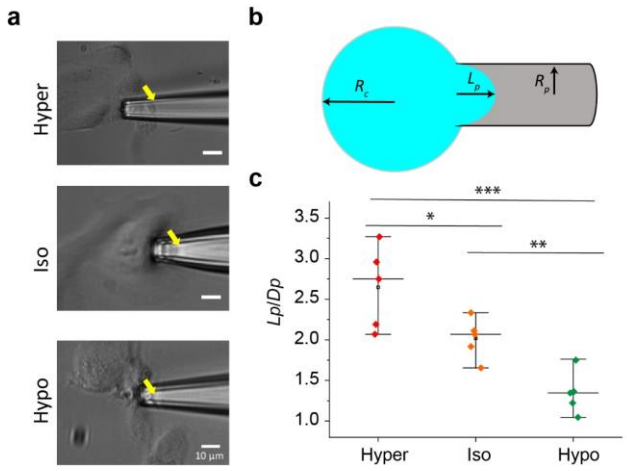

Figure. 2.4. Micropipette aspiration shows osmotic shock increases tension.

a. Plasma membrane aspirated into the micropipette due to negative hydrostatic pressure (ΔP = -2.16 kPa) at hyper-, iso- and hypo-osmotic conditions. **b.** The simplified schematic of plasma membrane aspiration into the micropipette. L_p is the total length of aspiration, R_c is the radius of the cell (assuming spherical shape) and R_p is the radius of the pipette ($D_p = 2R_p$). **c.** L_p/D_p values of cells under hyper-, iso- and hypo-osmotic conditions. *, **, *** represent $p < 0.05$, $p < 0.01$, and $p < 0.001$, respectively.

When imaged by TIRF microscopy, epsin puncta appear to be brighter under hypo-osmotic conditions **(Figure. 2.5)**. Cells imaged had similar expression levels of fluorescent proteins (epsin EGFP and mCherry CLC) between different osmotic conditions (**Figure. 2.6a)**. The intensity traces of CCSs belonging to 60-78 s lifetime cohort showed an increase in intensity of epsin EGFP when the osmolarity of the media was reduced **(Figure. 2.6b)**. The average plateau intensity of epsin in other lifetime cohorts (from 10-18 s to 100-120 s) was also higher

with a decrease in media osmolarity **(Figure. 2.6c)**, a result similar to what I have observed from the resting cell tension experiments. Our osmotic shock experiments suggest an increase in recruitment of epsin accompanies an acute increase in tension. The intensity of mCherry CLC in CCSs in epsin-expressing cells, belonging to 60-78 s lifetime cohort, showed a small increase with the acute increase in tension **(Figure 2.6d)**. CLC plateau intensity in epsin EGFP-recruited CCSs were the same between hyper- and iso-osmotic conditions but significantly increased for hypo-osmotic condition **(Figure 2.6e)**. Intensity profile of epsin starts at a maximum (**Figure. 2.6b**), pointing to a delay in recruitment of clathrin which was used as the primary detection channel in these analyses. To capture the initial intensity profile of epsin, I used epsin as the primary detection channel **(Figure 2.6f)**, and this intensity profile recaptures the trend I have seen when epsin was a secondary channel (**Figure. 2.6b**). Further, the ratio of maximum intensity of epsin and clathrin was lower for hyper-osmotic condition, but it remained in comparable range for iso- and hypo-osmotic condition **(Figure. 2.6g)**. This result is different from changing the resting cell tension experiments where I observed reduced clathrin intensity, suggesting an acute tension increase has a different effect on clathrin assembly.

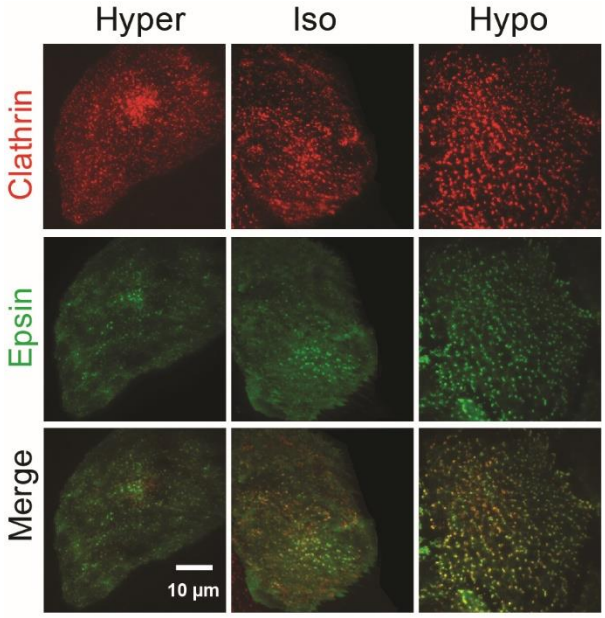

Figure 2.5. Fluorescence images of clathrin and epsin of RPE cells expressing epsin EGFP under different osmotic conditions.

In contrast, clathrin recruitment into CCSs in cells without epsin overexpression **(Figure 2.7a)** was the same when cells were subjected to an acute increase in tension **(Figure 2.7b)**. However,

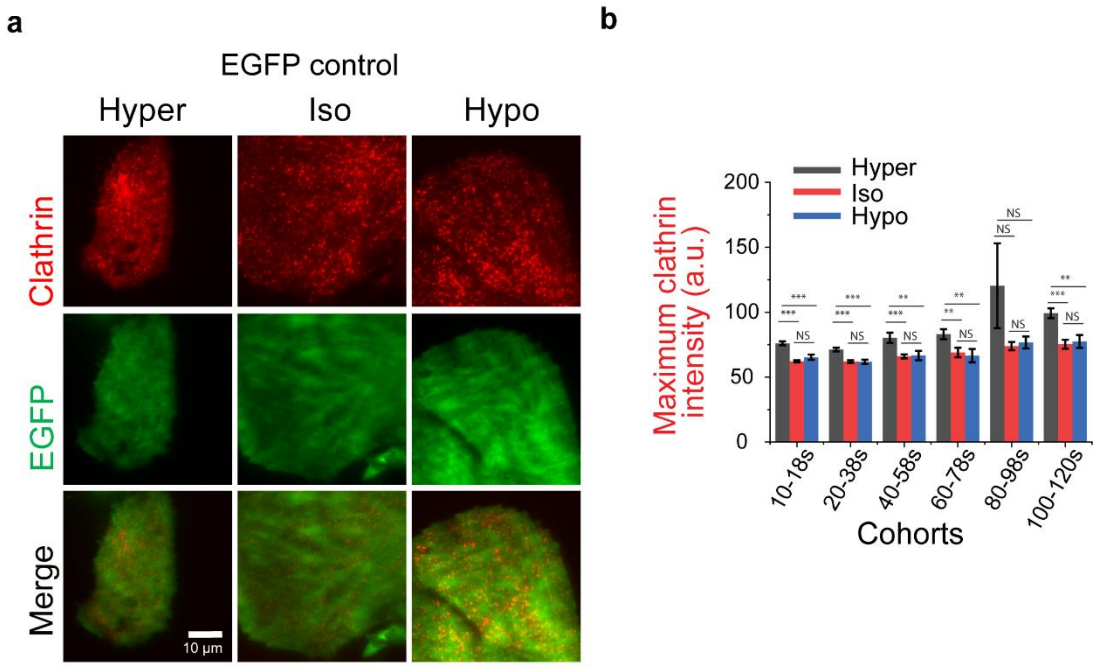

Figure 2.7. Clathrin recruitment into CCPs in EGFP control cells remains unchanged with increase in acute tension and increases during acute tension drop.

a. Representative fluorescence images of clathrin and EGFP of RPE cells expressing EGFP as a control under different osmotic conditions. **b.** The average plateau intensity of clathrin across different CCP lifetime cohorts in RPE cells. For b, N_{cells} expressing EGFP for hyper-, iso-, and hypo-osmotic conditions were 7 (N_{tracks}= 16149), 8 (N_{tracks}= 14315), and 11 (N_{tracks}= 20134), respectively. The error bars denote standard error. NS denotes not significant. *, **, *** represent $p < 0.05$, $p < 0.01$ and $p < 0.001$, respectively.

overexpression of epsin rescues the recruitment of clathrin in CME cohorts at high tension, as shown earlier. This points to the role of epsin in promoting clathrin recruitment when membrane tension is increased acutely.

2.4.3 ENTH domain containing H_0 helix supports tension-mediated nucleation of epsin at CCS sites

The tension response by epsin to changes in resting tension or acute tension variation is unique from other membrane-associated proteins. Typically, elevated tension reduces the

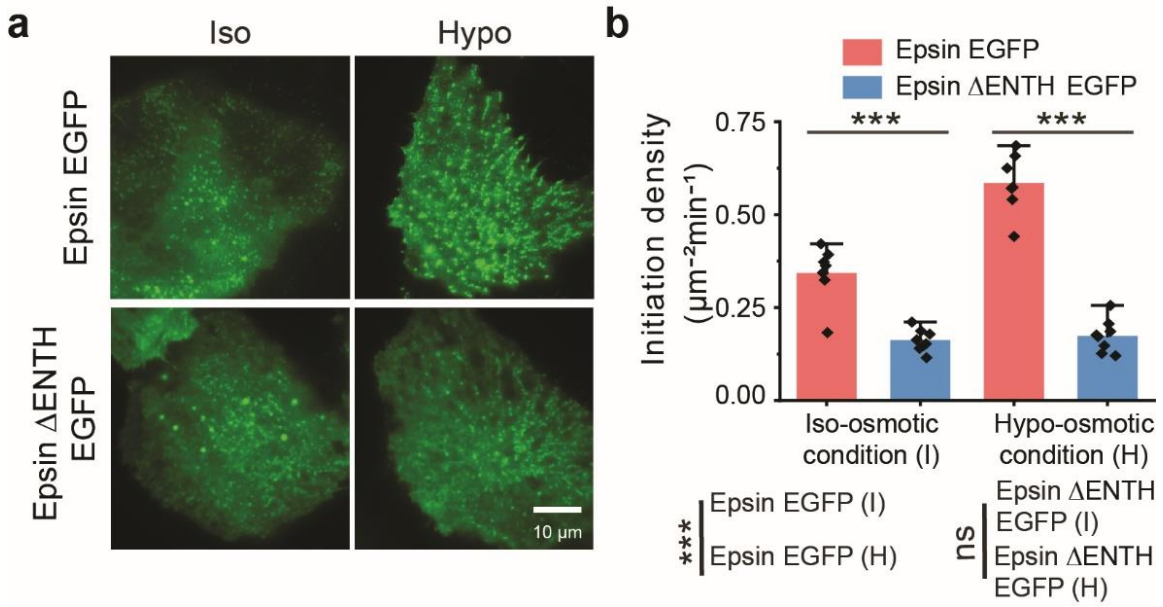

Figure 2.8. ENTH domain supports tension-mediated nucleation of epsin at CCS sites.

a. Fluorescence images of epsin, epsin ΔENTH at control (iso-) and high-tension (hypo-osmotic conditions). **b.** Initiation density of epsin puncta in epsin EGFP (salmon) expressing and epsin ΔENTH (blue) expressing cells under control (iso-osmotic) and high-tension (hypo-osmotic) conditions. For b, N_{cells} expressing epsin EGFP under iso- and hypo-osmotic conditions were 7 (N_{tracks} = 21570) and 7 (N_{tracks} = 24611) respectively, and N_{cells} expressing epsin ΔENTH under iso- and hypo-osmotic conditions were 8 (N_{tracks} = 13400) and 8 (N_{tracks} = 21300) respectively. The error bars denote standard error. NS denotes not significant. *, **, *** represent $p < 0.05$, $p < 0.01$ and $p < 0.001$, respectively.

recruitment of proteins to the membrane[32,68]. Paradoxically, epsin shows an increase of recruitment in response to elevated tension. Since the H_0 helix in the N-terminus of epsin can insert into the bilayer upon membrane binding[134], I hypothesize that this helical insertion contributes to the unique tension response of epsin. To test this hypothesis, I first removed the ENTH domain of epsin, which is the structured N-terminus region of epsin that contains multiple alpha helices, including the H_0 helix. The removal of ENTH domain of epsin did not render it cytosolic **(Figure 2.8a)**, suggesting other parts of epsin can still target it to CCSs. However, it appeared to decrease the number of initiation events of CCSs containing epsin without ENTH compared to full-length epsin **(Figure 2.8b)**. Further, as tension increased, overexpressing full-length epsin led to an

increase in CCS initiation density **(Figure 2.8b)**. This result implies that epsin can sense an increase in membrane tension and respond to it dynamically by increasing CCS nucleation. In contrast, the initiation density of epsin ΔENTH puncta remained unchanged with an increase in membrane tension **(Figure 2.8b)**. This points to ENTH domain playing a role in tension sensitivity of epsin and mediating epsin membrane binding at high membrane tension.

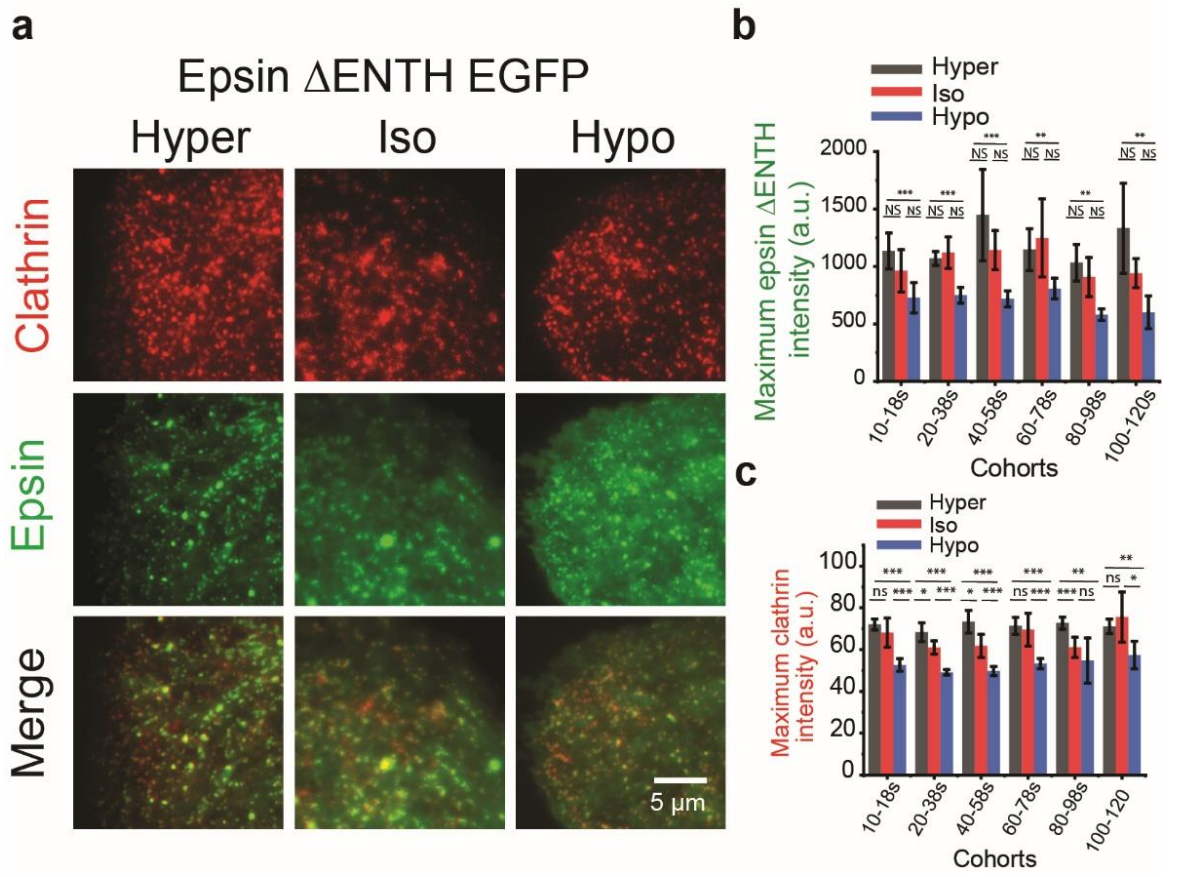

Figure 2.9. Epsin ΔENTH recruitment into CCSs reduces as membrane tension increases.

a. Representative fluorescence images of clathrin and epsin of RPE cells expressing epsin ΔENTH EGFP under different osmotic conditions. The average plateau intensity of epsin ΔENTH EGFP (**b.**) and mCherry Clathrin (**c.**) in different CCS lifetime cohorts in different osmotic conditions. The N_{cells} expressing epsin ΔENTH EGFP for hyper-, iso-, and hypo-osmotic conditions in c. and d. were 12 (N_{tracks}= 19328), 12 (N_{tracks}= 20078), and 12 (N_{tracks}= 31952), respectively. The error bars denote standard error. NS denotes not significant. *, **, *** represent $p < 0.05$, $p < 0.01$ and $p < 0.001$, respectively.

To further delineate the effect of ENTH domain on tension-mediated recruitment of epsin, I analyzed the intensity of epsin ΔENTH in CCSs in cells co-expressing epsin ΔENTH EGFP and mCherry CLC **(Figure 2.9a)**. The average plateau intensity of epsin ΔENTH EGFP in CCPs across multiple lifetime cohorts slightly reduced or remain the same in response to osmotic shock-induced membrane tension increase **(Figure 2.9b)**. Removal of ENTH domain abrogated the elevated epsin

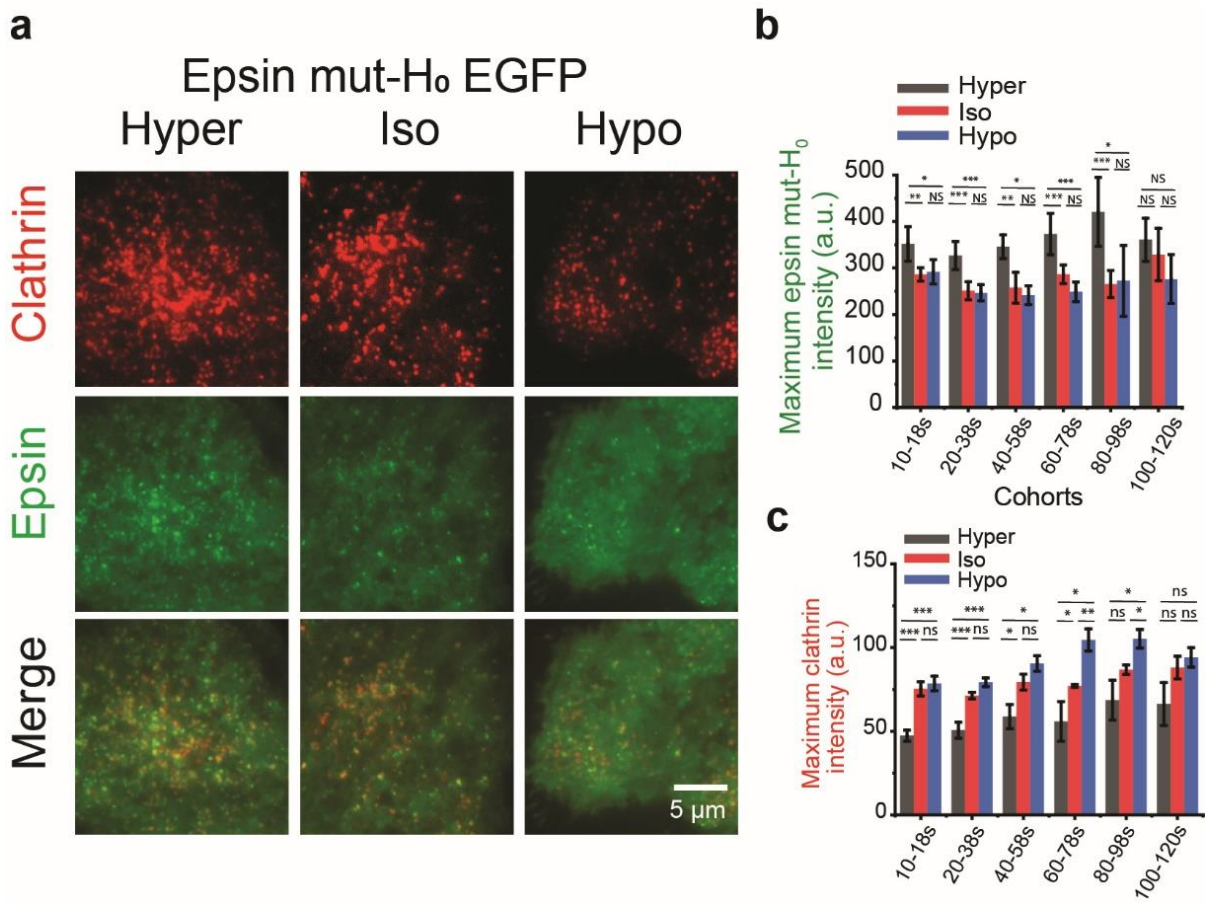

Figure 2.10. Epsin mut-H₀ recruitment into CCSs reduces as membrane tension increases.

a. Representative fluorescence images of clathrin and epsin of RPE cells expressing epsin mut-H_0 EGFP under different osmotic shock conditions. The average plateau intensity of epsin mut-H_0 EGFP (**b.**) and mCherry clathrin (**c**.) in different CCS lifetime cohorts in different osmotic conditions. The N_{cells} expressing epsin mut-H_0 for hyper-, iso-, and hypo-osmotic conditions in c. and d. were 18 (N_{tracks}= 32327), 19 (N_{tracks}= 33354), and 18 (N_{tracks}= 40602), respectively. The error bars denote standard error. NS denotes not significant. *, **, *** represent $p < 0.05$, $p < 0.01$ and $p < 0.001$, respectively.

recruitment to CCSs at high tension. However, the average plateau intensity of clathrin in CCSs with epsin ΔENTH EGFP reduced or remained comparable between iso-osmotic and hypo-osmotic conditions **(Figure 2.9c)**. This hinted the possibility that ENTH domain may be dispensable for epsin-mediated stabilization of clathrin in CCSs.

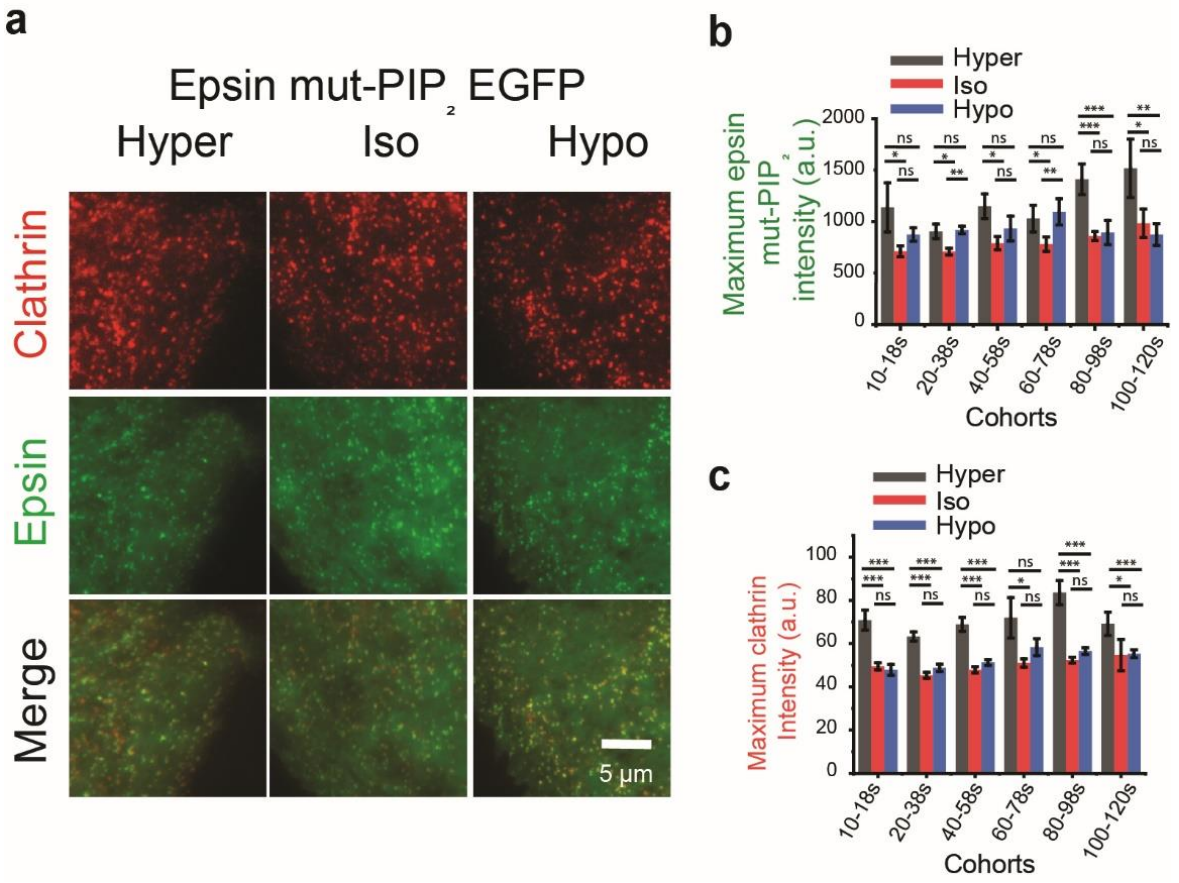

Figure 2.11. Epsin mut-PIP$_2$ recruitment into CCSs reduces as membrane tension increases.

a. Representative fluorescence images of clathrin and epsin mut-PIP$_2$ of RPE cells expressing epsin mut-PIP$_2$ EGFP under different osmotic conditions. The average plateau intensity of epsin mut-PIP$_2$ EGFP (**b.**) and mCherry CLC (**c.**) in different epsin mut-PIP$_2$ positive CCP lifetime cohorts in different osmotic conditions. The N_{cells} expressing epsin mut-PIP$_2$ for hyper-, iso-, and hypo-osmotic conditions in b and c. were 8, 8, and 8, respectively. The error bars denote standard error. NS denotes not significant. *, **, *** represent $p < 0.05$, $p < 0.01$ and $p < 0.001$, respectively.

To understand how removal of ENTH renders epsin unable to sense tension, I next replaced the residues in ENTH which form H_0 helix upon binding PIP_2 [117] to histidine. These mutations prevent the formation of H_0 helix when epsin binds to lipid bilayer and blocks amphipathic helix insertion. Dual-color TIRF imaging **(Figure 2.10a)** and downstream analysis of CCPs with mut-H_0 epsin co-localization shows the loss in epsin mut-H_0's ability to increase recruitment across different lifetime cohorts from an acute tension increase (**Figure 2.10b**), whereas full-length epsin increases in recruitment as membrane tension increases. This confirmed that H_0 helix imparts the tension sensitivity to epsin. This is an important result, as I showed that ENTH domain with amphipathic insertion can sense membrane tension in addition to the already known ability to detect membrane curvature[117,147] and dynamically alter the recruitment pattern of epsin to CCSs. The average plateau intensity of clathrin in CCPs with epsin mut-H_0 EGFP increased slightly or remained in the comparable range as membrane tension increased acutely (**Figure 2.10c**). This suggests that epsin-mediated stabilization of clathrin in CCPs can occur without amphipathic insertion of H_0 into the bilayer.

Further, I mutated the PIP_2 binding site in H_0 helix RRQMK to SSQMS such that PIP_2 binding is not possible. This mutant also showed a similar recruitment behavior as that of epsin ΔENTH and epsin mut-H_0 **(Figure 2.11a and b)**. Epsin mut-PIP_2 also lost the ability to recruit to CCSs with increased membrane tension **(Figure 2.11b)**. I postulate that PIP_2 initiates the coiling

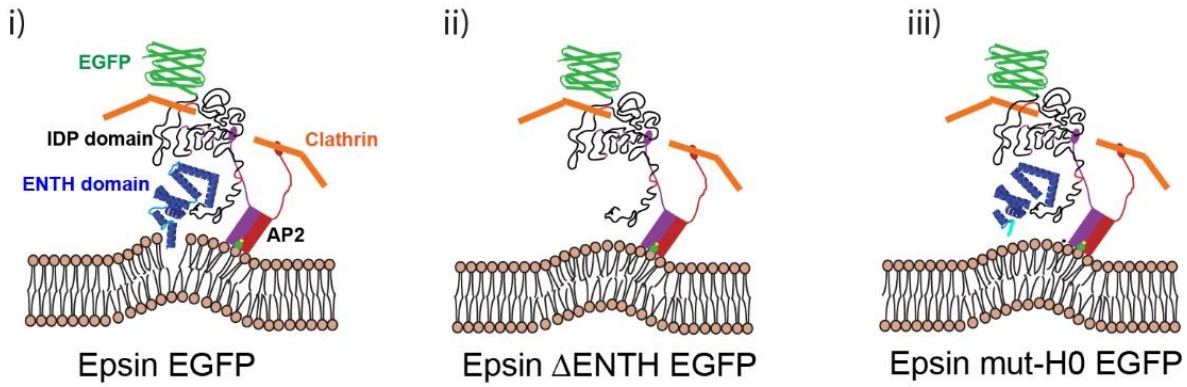

Figure 2.12. Proposed model for (i) epsin EGFP, (ii) epsin ΔENTH EGFP, and (iii) epsin mut-H_0 EGFP nucleation at CCS sites

of H_0 helix and the H_0 senses the changes in membrane tension by detecting changes in the area per lipid. Finally, I reason that endocytic binding domains in C-terminus region of epsin helps its binding to CCSs in the absence of ENTH domain or amphipathic insertion. Based on this assumption, I propose a model for epsin binding for full-length **(Figure 2.12 (i))**, ΔENTH **(Figure 2.12 (ii))**, mut-H_0 **(Figure 2.12 (iii))**.

2.4.4 Atomistic insights into ENTH-membrane interactions.

To substantiate my intuition, my collaborators performed MD simulations to quantify the interactions of ENTH domain with a lipid membrane made of 1-palmitoyl-oleoyl-sn-glycero-phosphocholine (POPC) lipids and a single PIP_2 lipid using CHARM-GUI. The ENTH domain was placed onto the membrane. This led to an instantaneous interaction of the H_0 helix with PIP_2 and the subsequent insertion of the H_0 helix into the membrane. The ENTH domain was then pulled away from the protein. As a consequence, the inserted H_0 helix first transitioned to an adsorbed state, and on further pulling was removed from the membrane into the solution. The three stages of ENTH-membrane interaction are shown in **Figure 2.13a**. It is notable that the secondary structure of the H_0 helix undergoes a transformation based on the degree of lipid interactions **(Figure 2.13a bottom panel)**. **Figure 2.13b** shows the secondary structure analysis as a function

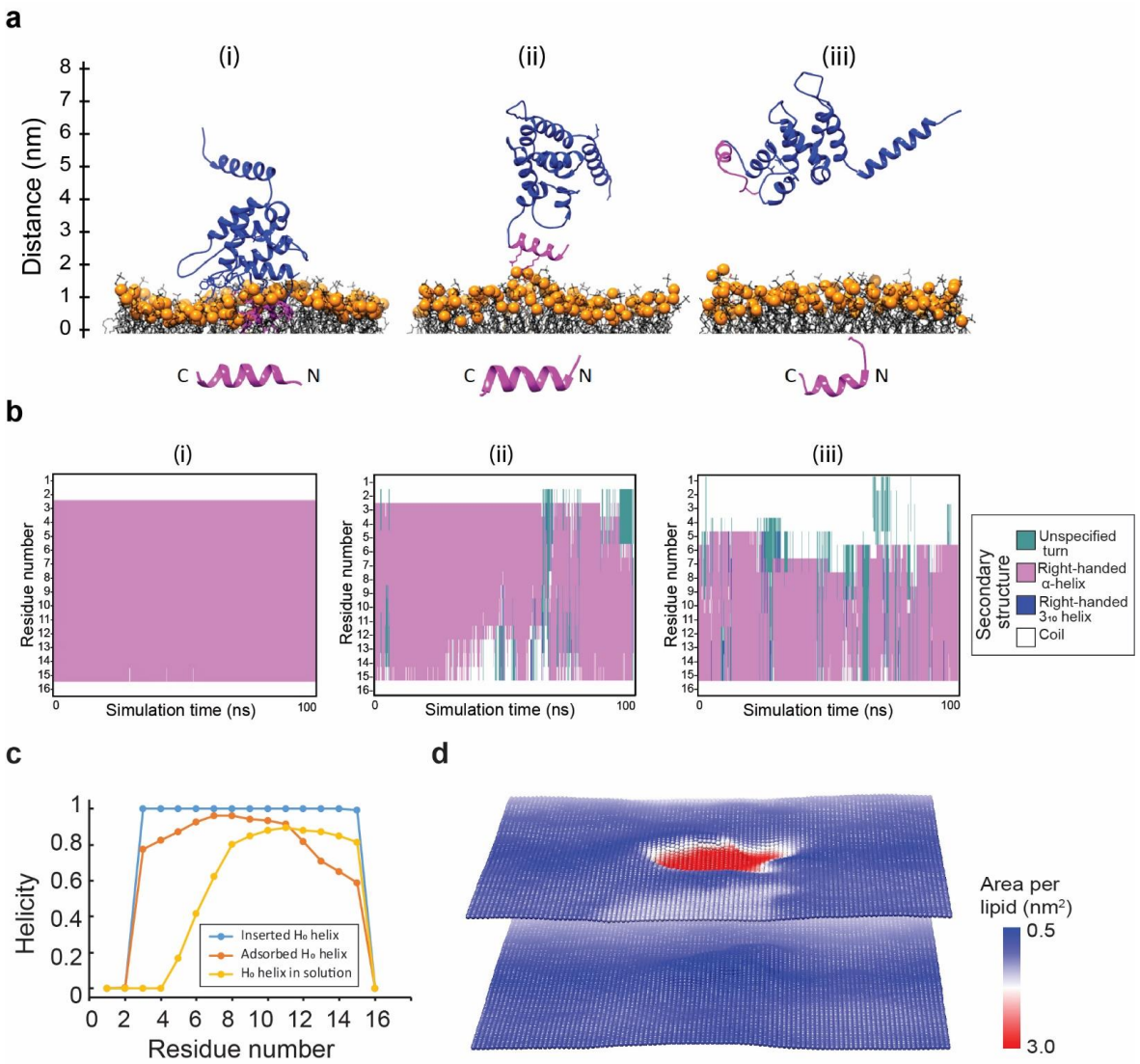

Figure 2.13. Atomistic insights into ENTH-membrane interactions.

a. ENTH domain interacting with POPC membrane with a single PIP_2 lipid and pulled out of the membrane. The H_0 helix shown in magenta is in the inserted (i), adsorbed (ii) and solvent (iii) states. **B.** Secondary structure analysis of each residue of H_0 in the three states shown in (a). **c.** The summary of the analysis in (b). The helicity of H_0 decreases as it undergoes reduced interactions with the membrane. The protein-lipid interactions stabilize the alpha-helix structure of H_0. **D.** The area per lipid plot corresponding to the inserted state shown in Fig. (a). The POPC lipids have a typical area of 0.64 nm^2. The presence of H_0 displaces lipids in the top leaflet. As a result, the effective area per lipid increases in the H_0-occupied domain (red region).

of the three stages of the H_0 helix. In the inserted state, the H_0 has an alpha-helix structure (pink color). In the adsorbed state with reduced lipid interactions, the H_0 helix begins to become

disordered from the N-terminus (teal color). In the final state when H_0 is in the solution, the alpha-helix domain shrinks further transforming into the disordered domain (teal color). The extent of helicity of H_0 helix residues in the three states is summarized in **Figure 2.13c**.

Figure 2.13d shows the areal footprint of the H_0 helix inside the membrane. The plot shows area per lipid in the two leaflets of the membrane. The POPC lipid area is around 0.64 nm^2 (blue color). Because of the H_0 helix insertion, the lipids are moved out of the H_0-occupied domain. This displacement of lipids effectively increases lipid-lipid separation, which in turn results in an increase in the area per lipid (red color). Since the protein sits primarily in the top leaflet, the change in area per lipid is minimal in the bottom leaflet. This areal footprint plot suggests a potential mechanism for tension sensitivity exhibited by epsin. A single H_0 helix occupies an area of 2 nm^2 (red region) and displaces lipids in the membrane. If the membrane has zero resting tension and the lipids are allowed to move freely, there would be no energetic advantage to displacing the lipids. However, if the membrane has a non-zero resting tension (σ), the displacement of lipids would be associated with an energetic incentive of $-\sigma\Delta A$, where ΔA is the area occupied by the H_0 helix. This idea is similar to the notion that explains the tension sensitivity of mechanosensitive channels in bacterial membranes[148,149].

2.4.5 Interfering the formation of H_0 helix inhibits early recruitment of epsin to CCPs.

The earlier observation that the recruitment of epsin EGFP prior to the arrival of clathrin and the importance of H_0 helix insertion prompted us to ask whether masking the ENTH domain might alter epsin recruitment to CCPs. Here I considered epsin with EGFP tagged to the C-terminus and EGFP tagged on the N-terminus (masking the ENTH domain), in addition to epsin ΔENTH EGFP and epsin mut-H_0 EGFP mutants and examined kymographs of different epsin mutants. Using CCP tracks with detection that started at first significant clathrin signal **(Figure 2.14a, detection mode**

1), I determined the order of arrival of epsin with respect to clathrin. Epsin with EGFP attached to the C-terminus arrived at CCPs prior to clathrin, as the kymograph showed more green fluorescence at the beginning of the lifetime track **(Figure 2.14b panel 1)**, pointing to the early recruitment of epsin prior to clathrin and consistent with what I observed in **Figure 2.6b** and **2.6f**. In contrast, the masked ENTH showed synchronous recruitment with clathrin (**Figure. 2.14b panel 2**). This finding is consistent with work of Taylor *et al.* which showed delayed recruitment of epsin compared to AP2, when fluorescent protein is placed in the N-terminus of epsin[150]. Similarly, both epsin ΔENTH EGFP and epsin mut-H_0 EGFP helix mutants showed synchronous recruitment with clathrin **(Figure 2.14b panel 3 and 4)**. These data were further quantified by plotting the normalized intensities of clathrin and epsin until they reached their maximum intensity after performing CCP detection and tracking with epsin as primary channel **(Figure 2.14a, detection mode 2)**. Normalized epsin EGFP recruitment curve was above the mCherry CLC recruitment curve, pointing to early recruitment of epsin **(Figure 2.14c)**. In addition, epsin EGFP reached maximum recruitment prior to mCherry CLC (shown with cyan and magenta arrows). However, cells expressing epsin with masked or deleted ENTH domain or with mutated H_0 helix showed epsin recruitment in synchrony with mCherry CLC **(Figure 2.14 d-f)**. Based on these results, I suggest that epsin EGFP recruitment to membrane precedes clathrin **(Figure 2.14g case i)**, whereas masking ENTH domain with EGFP disrupts or delays the formation of H_0 amphipathic helix insertion into the bilayer (**Figure 2.14g**

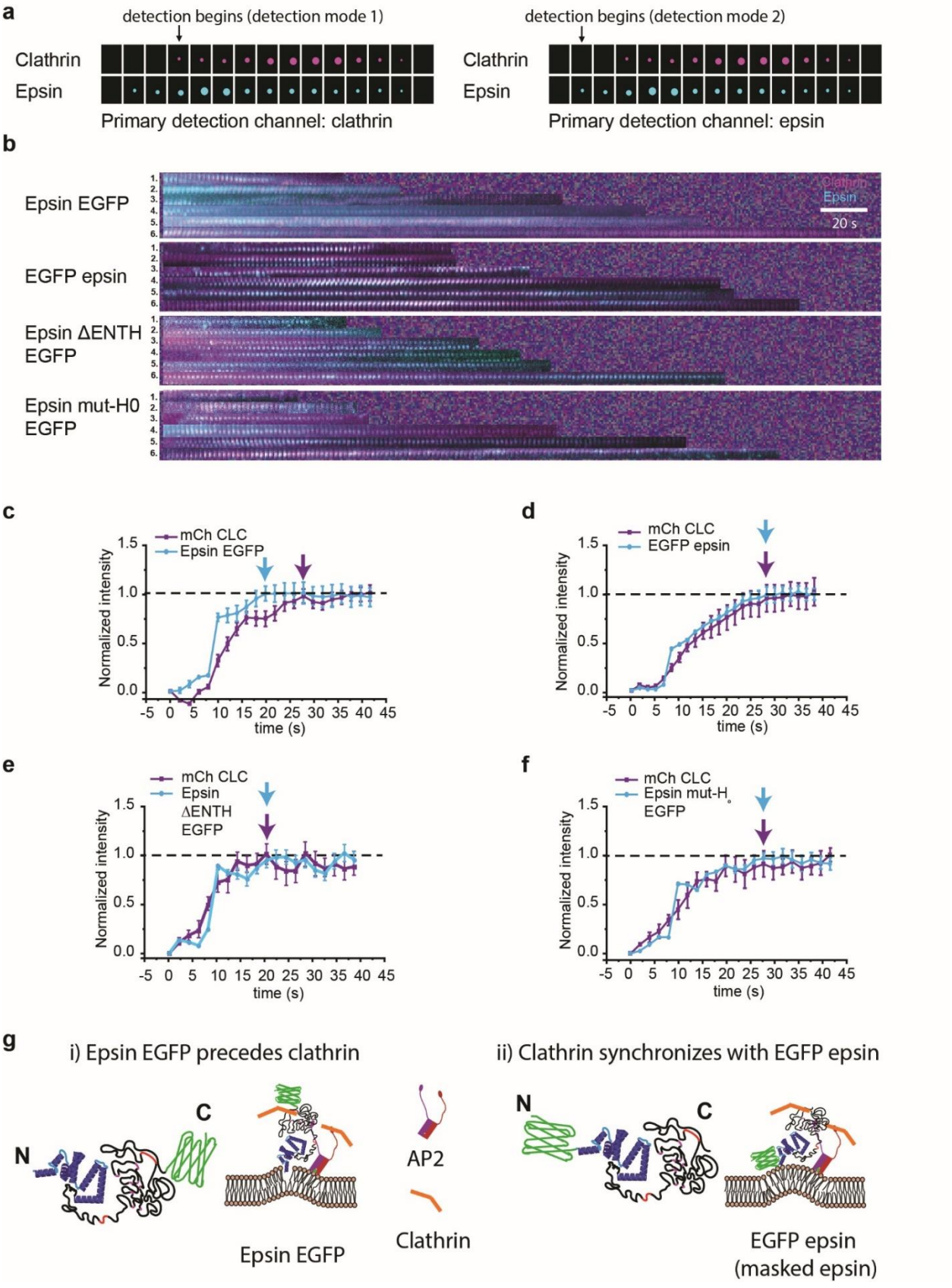
a
detection begins (detection mode 1)
Clathrin
Epsin
Primary detection channel: clathrin
detection begins (detection mode 2)
Clathrin
Epsin
Primary detection channel: epsin
b
Epsin EGFP
EGFP epsin
Epsin ΔENTH EGFP
Epsin mut-H0 EGFP
Clathrin
Epsin
20 s
c
mCh CLC
Epsin EGFP
Normalized intensity
time (s)
d
mCh CLC
EGFP epsin
Normalized intensity
time (s)
e
mCh CLC
Epsin ΔENTH EGFP
Normalized intensity
time (s)
f
mCh CLC
Epsin mut-H0 EGFP
Normalized intensity
time (s)
g
i) Epsin EGFP precedes clathrin
ii) Clathrin synchronizes with EGFP epsin
N
C
AP2
Clathrin
Epsin EGFP
EGFP epsin
(masked epsin)

Figure 2.14. Epsin is recruited prior to clathrin to CCS nucleation sites by amphipathic helix insertion.

a Schematic of two dual-channel detection modes depicting a scenario in which epsin (cyan) appears prior to clathrin (magenta). **b** Kymographs of CCSs with epsin EGFP, EGFP epsin, epsin ΔENTH EGFP and epsin mut-H_0 EGFP (primary detection channel: clathrin). Normalized recruitment of epsin (cyan) and clathrin (magenta) (primary detection channel: epsin) for the 60-78s lifetime cohorts until they reach maximum intensity for (**c**) epsin EGFP, (**d**) EGFP epsin, (**e**) epsin ΔENTH EGFP, and (**f**) epsin mut-H_0 EGFP. **g** Proposed model for epsin recruitment with (i) EGFP in C-terminus and (ii) EGFP in N-terminus. N_{cells} for d, e, f, and g were 9 (N_{tracks} = 34777), 7 (N_{tracks}= 56492), 9 (N_{tracks} = 45754), and 7 (N_{tracks}= 36016), respectively. The error bars denote standard error.

case ii). This is also supported by the synchronous recruitment of epsin mut-H_0 EGFP and epsin ΔENTH with clathrin, as they cannot form H_0 helix upon binding to the membrane.

2.5 Discussion

The increase of epsin recruitment at high tension is dependent on the ENTH domain, and specifically the H_0 helix. My observation that undisrupted activity of ENTH, specifically the amphipathic insertion of H_0 helix, is required for early epsin recruitment would be consistent with its tension-sensing role. Importantly, it is consistent with a previous finding where epsin recruits clathrin to PIP_2-containing lipid monolayer and stimulates clathrin lattice assembly[134] . When ENTH of epsin is masked by N-terminal EGFP, its recruitment to CCS sites synchronizes with clathrin, presumably by binding to AP2 *via* epsin's IDP domain. This is in agreement with my finding that removing the ENTH domain did not inhibit the recruitment of epsin to CCSs but only affected its early recruitment. Because unstructured IDP region contains multiple clathrin

and AP2 binding sites, it is likely that the stability of CCSs at high tension is afforded by the avidity provided by multiple interactions[136]. The importance of multiple interactions is reinforced by the finding that knocking down either CHC or α-adaptin renders full-length epsin cytosolic. Although epsin ΔENTH can be recruited to sites of CCSs, this recruitment is reduced drastically when tension is increased, similar to the behaviors of other membrane-associated proteins when encountering high tension.

Using MD simulation, my collaborators showed that insertion of the H_0 helix into the lipid bilayer enables recruitment of ENTH into the membrane. The simulations also show that membrane-association triggers ordering of H_0 into a helical structure. Because of the favorable H_0–lipid interactions, ENTH prefers to bind to the membrane. Also, the H_0 helix insertion displaces lipids, thereby providing an energetic advantage for epsin recruitment in high membrane tension regime. Tension-induced amphipathic helix insertion could perhaps be a general mechanism for membrane tension sensitivity for other cellular machineries. Any protein with a membrane-embedded segment could be expected to demonstrate tension-sensitivity. However, the propensity to sense tension and undergo recruitment would likely be proportional to the areal footprint of the inserted protein segment. This could be a prime reason that allows an amphipathic helix to act as a tension sensor as it lays tangential to the membrane, displacing a higher number of lipids in contrast to an orientation normal to the membrane. Another potential example of this mechanism could be occurring in nucleation promoting factor N-WASP. Under load, actin networks become denser to support the increased load[151]. In this context, increased membrane tension should therefore promote actin assembly, and this can be achieved by increasing actin filament nucleation. Interestingly N-WASP has an amphipathic helix[152]. Thus,

it is plausible, although highly speculative, that recruitment of N-WASP to the plasma membrane could be tension-sensitive in a fashion similar to epsin.

The ability of H_0 helix to detect curvature versus to generate curvature is an ongoing debate. It is already shown that H_0 helix can preferentially recruit to areas of high curvature [117,138,153]. Our MD simulations show that area per lipid molecule increases as membrane tension increases. Area per lipid values also increase as membrane curvature increases. Membrane scaffolding proteins like BAR proteins and epsin have been shown to recruit selectively to highly curved membrane tethers kept at high tension[138,154]. An increase in tension in this finite membrane tether reduces the tether radius and thereby increasing curvature. Similarly, an increase in area per lipid due to an increase in tension may lead to recruitment of epsin which facilitates membrane bending. Initial membrane bending by nucleating epsin can further increase the local area per lipid around nucleation sites further increasing epsin recruitment. This will lead to a positive feedback loop of membrane curvature sensing and membrane curvature generation.

Although I have identified a new mode of epsin function, I speculate epsin is not unique in mediating tension-responsive recruitment to and stabilization of CCSs. In particular, adaptor protein 180 (AP180) and its homolog clathrin assembly lymphoid myeloid leukemia protein (CALM) both have alpha helices in their N-terminal domains[135] along with an unstructured IDP region consisting of endocytic binding domains[133]. Thus, it is plausible that a similar mechanism could be at play with AP180 and CALM to support CME under high tension environments. Several works using MD simulation and *in vitro* experiments have shown the role of amphipathic helices, specifically H_0 helix, in curvature generation mechanism of N-BAR proteins[117,119,153,155]. It should be investigated whether H_0 helix insertion of these proteins also enables tension-

mediated membrane curvature generation and stabilization. My work also provides some unexpected findings for future investigation. While I mainly focused on the role of epsin in high tension environments, decreasing tension in hypertonic solutions resulted in distinct responses. In particular, steady state density of epsin ΔENTH puncta under a hyper-osmotic condition was significantly higher compared to the iso-osmotic condition. Acute reduction in tension has been shown to trigger PLD2-mediated macropinocytosis in cells[68]. It is also known that rapid reduction in membrane tension leads to excess plasma membrane and cells utilize endocytic mechanism to recycle the lipid bilayer[82,156,157]. It should be further investigated how a low tension environment influences the ability of epsin and family of proteins with amphipathic helices to recruit in a tension responsive manner.

2.6 Acknowledgments

J.G.J., A.A. and A.P.L. conceived the study, J.G.J., C.O., A.A., A.P.L. designed the experiments, J.G.J. and V.Y. performed the experiments, C.O. carried out the molecular dynamics simulation. J.G.J acknowledge the use of the Maxwell/Opuntia/Sabine Clusters and the advanced support from the Research Computing Data Core at University of Houston to carry out the molecular dynamics simulations presented here. J.G.J acknowledge Dominic Ciarelli for helping me with micropipette aspiration. This work was supported by the National Science Foundation NSF-MCB 1561794 to A.P.L. and NSF grants CMMI 1562043 and CMMI 1727271 to A.A.

Chapter 3 Complimentary Action of Structured ENTH Domain and Unstructured IDP Domains of Epsin Supports Clathrin-Mediated Endocytosis at High Tension

The results of this chapter were published in part in Communication Biology (2020). J.G.J., A.A., and A.P.L. conceived the study, J.G.J., C.O., A.A., and A.P.L. designed the experiments, J.G.J. and V.Y. performed the experiments, J.G.J., A.A., and A.P.L. wrote the paper. All authors commented on the paper and contributed to it.

3.1 Abstract

Membrane tension impedes the transition of hemispherical domes to omega-shaped CCSs. Membrane tension also leads to the premature disassembly of CCSs before it can transition to omega-shaped cups. Epsin recruitment is elevated at high membrane tension. Overexpression of epsin in cells leads to the rescue of productive CCPs which successfully internalize from plasma membrane. Removal of ENTH domain does not impede epsin's ability to stabilize productive CCPs. However, removing the intrinsically disordered domain (IDP) from epsin renders it cytosolic. Epsin's binding to adaptor protein 2 and clathrin is critical for epsin's association with CCSs under high tension conditions, supporting the importance of multivalent interactions in CCSs. Together, my results support a model where the ENTH and unstructured IDP region of

epsin have complementary roles to ensure CME initiation and CCS maturation are unimpeded under high tension environments.

3.2 Introduction

Membrane tension has been shown to play an inhibitory role in CME during the membrane deformation process preventing the transition from a flat membrane to hemispherical domes[27,28] and the transition from hemispherical domes to Ω-shaped pits[26–28]. Yet, CME is observed ubiquitously in cells under different membrane tension regimes and this points to the existence of tension-sensitive molecular mechanisms supporting CME[26,108,156]. Actin-mediated transition of hemispherical domes to Ω-shaped pits at high tension was established by Boulant *et al*[26,158]. However, how membrane-associated proteins aid to overcome the elevated energy barrier needed to initiate budding remains an open question. In Chapter 2, I discussed how epsin utilizes amphipathic H_0 helix in ENTH domain to detect membrane tension and recruit in a tension responsive manner. However, whether this tension responsive recruitment plays a physiological role in rescuing CME at high tension remains to be investigated. Amphipathic helix insertion of H_0 helix in epsin and its role in initiating membrane bending during CME is well studied[117,133,159]. Epsin also has a C-terminus intrinsically disordered protein (IDP) region containing multiple binding sites to endocytic constituent proteins like clathrin and AP2 which stably dock epsin in the endocytic pit[133,160–162]. An alternate hypothesis proposed recently posits the C-terminus IDP domain of epsin initiates membrane bending *via* steric crowding[17,18]. Here, I used the combination of super-resolution live cell imaging including structural illumination microscopy (SIM-TIRF) imaging , mechano-manipulation techniques, and automated image analysis, to characterize CCSs according to their morphology and fate of internalization. Using these characterizations, I

demonstrate the role of IDP domain of epsin in stabilizing CCSs in high tension environments. My work establishes a mechanism involving complimentary roles of ENTH and IDP domains of epsin in recruitment into and stabilization of CCSs in a high-tension environment.

3.3 Materials and Methods

3.3.1 Generation of epsin mutant constructs

Epsin mutant constructs were generated successively by mutagenesis using Q5® Site-Directed Mutagenesis Kit (New England Biolabs Inc.). Clathrin binding domain 1 (CBD1) was deleted using following primers to create epsin ΔCBD1 EGFP **(Figure 3.1 (i))**: Forward primer 5'- TTCACAACCCCAGCCCCT-3'; Reverse primer 5'-AGATGACTCCTCCTTGCCC-3'. Clathrin binding domain 2 (CBD2) is deleted from epsin EGFP and epsin ΔCBD1 EGFP using following primers to create epsin ΔCBD2 EGFP **(Figure 3.1 (ii))** and epsin ΔCBD 1 & 2 EGFP **(Figure 3.1 (iii))**: Forward primer 5'-TCACTGGTGAGCCGACCA-3'; Reverse primer 5'-GGCTGCATTAGGGCCTAG-3'. Epsin amino acid sequence containing endocytic binding cites CBD1, CBD2 and AP2 binding motifs were deleted using following primers using to create epsin Δ EBD EGFP**(Figure 3.1 (iv))**: Forward primer 5'-TCACTGGTGAGCCGACCA-3'; Reverse primer 5'-AGATGACTCCTCCTTGCCC-3'. Unstructured IDP region of epsin was removed using following primers to generate epsin ΔIDP EGFP **(Figure 3.1 (v))**: Forward primer 5'-GGAAGTGGAAGTGGAAGTGGAGAATTCG-3'; Reverse primer 5'-GCGCTCCTCCCGAAGCCG-3'. All mutant constructs were transformed into competent *E. coli* cells (New England Biolabs Inc.) and selected using antibiotics (Ampicillin).

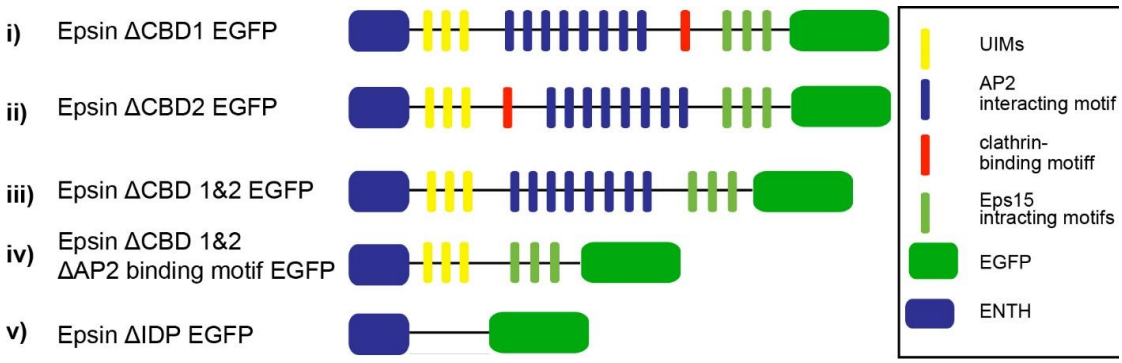

Figure 3.1 Epsin mutants.

Epsin EGFP mutants generated by deleting binding domains (i) clathrin-binding domain1 (CBD1), (ii) clathrin-binding domain 2 (CBD2), (iii) clathrin-binding domain 1 and 2 (CBD1 & 2), (iv) CBD1 & 2 and region containing repeated DPW motifs binding to AP2 and (v) entire unstructured region of the protein deleted (ΔIDP).

3.3.2 shRNA knockdown

shRNA constructs for epsin/alpha adaptin/clathrin heavy chain (CHC) were created in pLKO.1 vector by the UM vector core. Lentiviruses encoding shRNAs of interest were generated using the lentivirus transduction method described in Chapter 2. RPE cells were infected with the viruses and selected using antibiotic selection (Puromycin). All downstream assays (TIRF imaging or Western blotting) were performed on day 5 of transduction and the level of knockdown was confirmed by Western blot analysis.

3.3.3 Osmotic shock

The RPE cells were imaged in three media having different osmolarities: (i) hyper – 440 mmol/kg, (ii) iso – 290 mmol/kg, (iii) hypo – 220 mmol/kg) were used. Hyper-osmotic solution was prepared by adding 150 mM sucrose to phenol red-free DMEM containing 2.5% FBS. Iso-osmotic solution was DMEM media with 2.5 % FBS. Hypo-osmotic solution was prepared by adding deionized water containing 2.5% FBS to DMEM media containing 2.5% FBS in 1:3 ratio.

All media osmolarities were checked on a Vapro osmometer. The cells were imaged between 5 minutes and 35 minutes of adding the different media.

3.3.4 Actin cytoskeleton disruption

RPE cells overexpressing epsin EGFP and mCherry clathrin were incubated with Latrunculin A (0.5 µM) (Thermo Fisher Scientific) for 30 minutes prior to TIRF imaging for disrupting actin cytoskeleton.

3.3.5 Live cell imaging *via* structural illumination microscopy in total internal reflection fluorescence mode (SIM-TIRF)

RPE cells expressing the constructs of interest were plated on a MatTek dish at a concentration of ~ 1.7 x 10^5 cells per dish for 12 to 16 hours. SIM-TIRF **(Figure 3.2a)** was performed using a Nikon N-SIM microscope equipped with an Apochromat 100X objective (NA 1.49) and a sCMOS camera (Flash 4.0; Hamamatsu Photonics, Japan). Epsin EGFP was imaged using 488 nm laser with exposure time of 200 ms, with nine images taken in TIRF mode with linear translation of Moire pattern for SIM reconstruction. Similarly, mCherry clathrin was imaged using 561 nm laser with exposure time of 500 ms. Time interval between each set of SIM reconstruction images were 5 sec. Dual color SIM-TIRF images for epsin EGFP and mCherry clathrin was performed using DeltaVision OMX SR system (GE) equipped with 60x 1.42 NA objective and a sCMOS camera. Epsin EGFP and mCherry clathrin were imaged using 488 nm and 561 nm lasers respectively, with exposure times of 50 ms. Nine images were taken in ring TIRF mode with angular translation of Moire pattern for SIM reconstruction.

3.3.6 Live cell imaging *via* superresolution confocal microscopy

RPE cells expressing the constructs of interest were plated on a MatTek dish at a concentration of ~ 1.7 x 10^5 cells per dish for 12 to 16 hours. Superresolution confocal microscopy **(Figure 3.2b)** was performed using an Olympus IXplore Spin Confocal Imaging Microscope with a 100X objective (UPLSAPO100XS, NA 1.35). The superresolution imaging was achieved using Yokogawa CSU-W1 Scanner with SoRa 50 µm disk. Dual color localized super-resolution images were obtained using two sCMOS camera (Flash 4.0; Hamamatsu Photonics, Japan). Apical surface of RPE cells where imaged for Epsin EGFP and mCherry clathrin using 488 nm and 561 nm lasers respectively, with exposure times of 100 ms and 200 ms respectively. Time interval between images were 2 sec. The images where analyzed using FIJI (ImageJ).

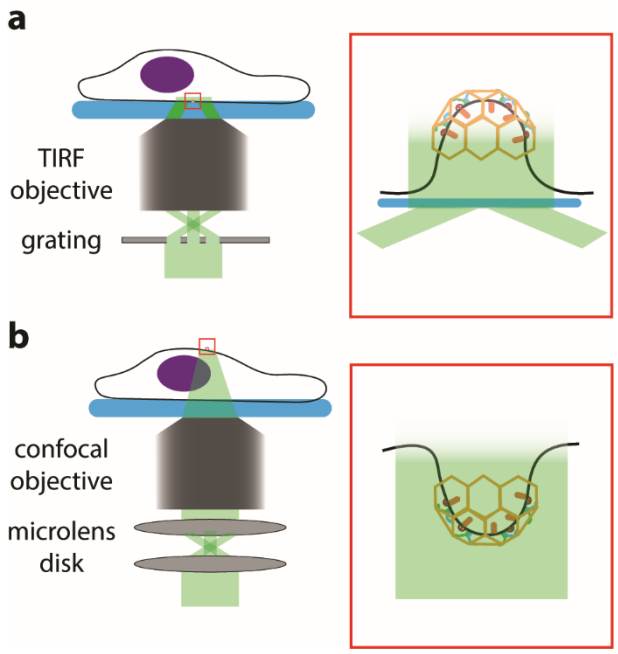

Figure 3.2 Live-cell super-resolution of CCSs

a. TIRF-SIM setup to image CCPs on basal side of cell. **b.** Super-resolution confocal setup to image CCPs on apical side of cell

3.3.7 Image reconstruction and analysis for SIM-TIRF

Images captured in Nikon N-SIM system was reconstructed into SIM images using Nikon Elements software. Reconstructed images were further equalized in intensity across time period using Nikon Elements software. CCSs were detected and tracked using Trackmate plugin in FIJI (ImageJ)[163]. A detector with Laplacian of Gaussian Filter is applied to detect CCSs with a quadratic

fitting scheme for subpixel localization and estimated blob size parameter of 500 nm. A simple Linear Assignment Problem (LAP) tracker was applied with a maximum linking and gap closing distance of 500 nm and maximum gap closing of 2 frames. CCSs were characterized into abortive, productive and stalled structures based on their morphology (whether or not CCSs form ring structures) and lifetime. Using lifetimes limits for abortive, productive and stalled CCS, the fraction of CCSs belonging to each category was determined.

3.3.8 Transferrin uptake assay

RPE cells expressing epsin mutants were serum-starved for 4 h. Cells were subjected to hypo- and iso-osmotic shock for 10 min and then allowed to uptake transferrin Alexa 647 (25 µg/ml) (Thermo Fisher) for a further 10 min, followed by acid wash (acetic acid buffer pH 3.0) and immediate fixation with 4% paraformaldehyde (Electron Microscopy Sciences) in PBS for 10 min. For imaging surface receptor-ligand co-localization, acid wash was not performed. The intensity of transferrin Alexa Fluor 647 was calculated using epifluorescence signal and normalized to bulk mCherry CLC intensity.

3.3.9 Western blot

RPE cells were lysed with RIPA buffer (Thermo Fisher) containing protease inhibitor on ice for 10 min. 25 µL of lysate mixed with sample buffer (1:1 ratio) (Bio-Rad) was loaded per lane in a 10% SDS-PAGE gel (Bio-Rad). The proteins were transferred to nitrocellulose membrane and blocked for 1 h with 3% BSA solution (in PBS). Primary antibodies against epsin (Abcam: ab75879 (1:500 dilution)), CHC (Abcam; ab2731 (1:500 dilution)), α-adaptin (Abcam: ab2807 (1:100 dilution)) were used to quantify the expression levels of the respective proteins in epsin

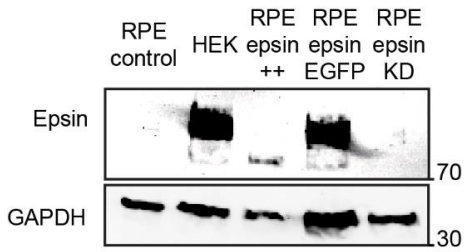

Figure 3.3 Western blot showing the expression of epsin in RPE cells and HEK cells (highest epsin expression shown), RPE cells overexpressing WT epsin, epsin EGFP and knockdown of epsin, with GAPDH as a loading control.

overexpressed cells, epsin/CHC/α-adaptin knockdown cells and wild type cells **(Figure 3.3)**. Blots with primary antibody and 1:1000 dilution of anti-GAPDH antibody were incubated overnight followed by 1 h incubation of secondary antibody conjugated to Dylight 680 nm or Dylight 800 nm. The blots were imaged using an LiCor imaging system or an Azure imaging system.

3.4 Results

3.4.1 Live-cell super-resolution microscopy can visualize the formation of productive CCPs.

CCSs can be classified into three categories based on their ability to internalize into cytosol from the cell membrane where they are nucleated. These three categories follow distinct fate during their lifetimes, (i) Abortive CCSs, which are coated structures which dissemble before they reach maturation[164–166], (ii) productive CCPs, which are coated structures that undergo initiation,

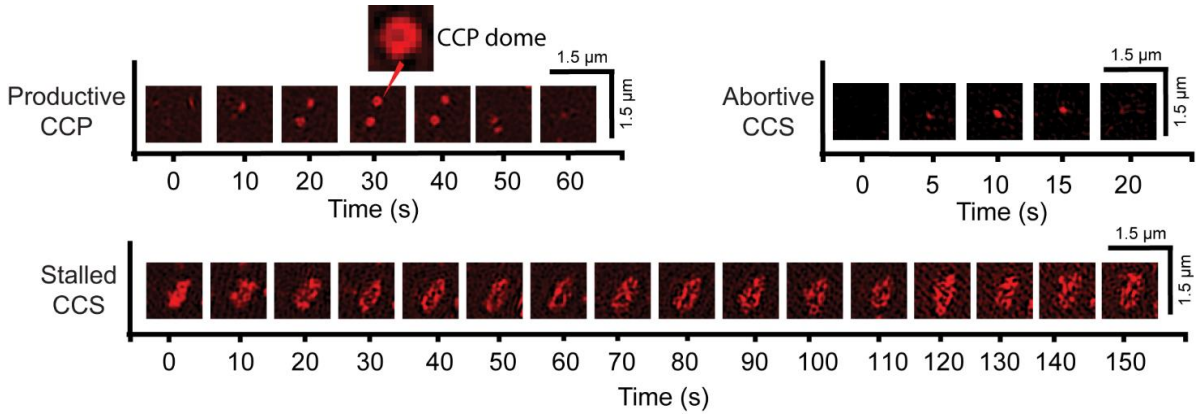

Figure 3.4 Categories of CCSs based on morphology

Lifetime montage of CCS/CCP (marker: mCherry CLC) classified as abortive, productive and stalled imaged using SIM-TIRF. The formation of a CCS dome (manifested as a ring in SIM-TIRF) is shown with a red arrow.

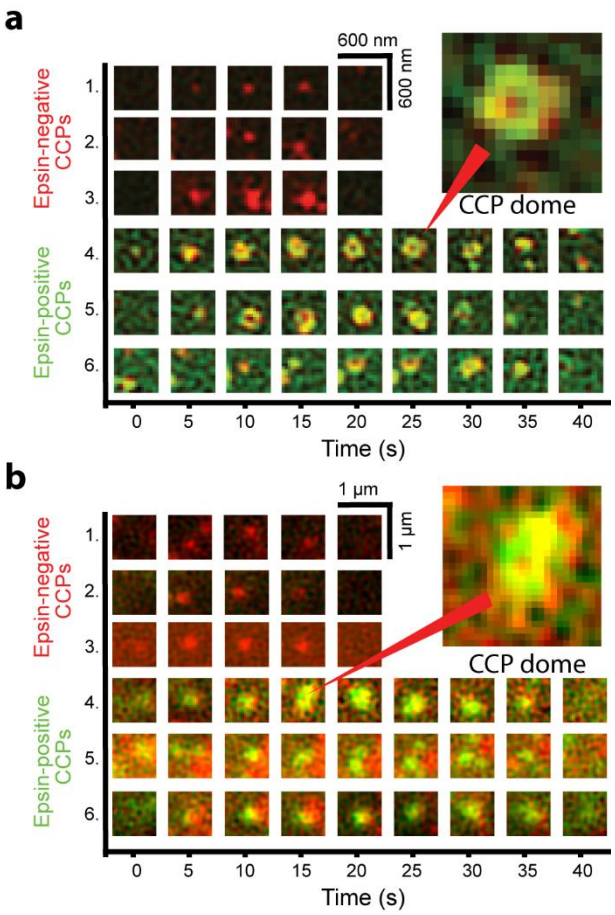

Figure 3.5. Dual color super-resolution images of CCSs in basal and apical layers of cells.

a. Lifetime montage of CCSs (red: mCherry CLC) at the basal layer of cells with or without recruitment of epsin (green) using dual color SIM-TIRF. **b.** Lifetime montage of CCSs (red: mCherry CLC) at the apical layer of cells with or without recruitment of epsin (green) using dual color super-resolution confocal imaging.

assembly, and transition to coated-pits followed by membrane scission and internalization, and (iii) stalled CCSs, which are persistent, non-internalizing coated structures in the imaging field[11,26]. Using SIM-TIRF super-resolution imaging of RPE cells stably expressing mCherry-clathrin light chain (CLC), I was able to visualize the distinct categories of CCSs **(Figure 3.3)**. Lifetime analyses of CCSs have shown that abortive CCSs have a lifetime less than 20 s[15,128,167] and stalled CCSs have a lifetime above 120 s[11,15,26]. Under SIM-TIRF field, a matured CCS reaches a domed shape, manifested as a ring (**Figure 3.4**, shown with red arrow) to form a productive CCP [168]. The track of a productive CCP shows the evolution of a point signal into a ring structure, subsequently transitioned to a point signal, and finally disappeared from the SIM-TIRF field **(Figure 3.4)**. By comparison, an abortive CCS did not transition from a point signal to a ring structure and disappeared from the SIM-TIRF field within a short time. Stalled CCSs were often clusters of CCSs in the shape of interconnected rings, which remained persistently in the

SIM-TIRF field. Dual color SIM-TIRF imaging was used to identify co-localization of epsin and clathrin in CCSs formed at the basal layer of cells **(Figure 3.5a)**. Formation of productive CCPs on the apical surface of cells were imaged using super-resolution confocal imaging along with the colocalization of epsin and clathrin in productive CCPs **(Figure 3.5b)**.

3.4.2 Overexpression of epsin in cells reduces abortive CCSs and supports productive CCPs at high tension.

Previous work from my lab have shown that retinal pigment epithelial (RPE) cells spread on large fibronectin islands (to induce high membrane tension) exhibited an increase in proportion of abortive CCSs and smaller CCPs[31,32]. RPE cells expressing epsin at endogenous level, overexpressing epsin, and overexpressing epsin EGFP were imaged under iso-osmotic (control - 290 mmol/kg osmolarity) and hypo-osmotic conditions (high tension - 220 mmol/kg osmolarity) using SIM-TIRF **(Figure 3.6a)**. RPE cells have low endogenous expression of epsin compared to cell lines like HEK, hence overexpression of epsin WT or epsin EGFP in RPE cells was used **(Figure 3.3)**. The cells were imaged between 5 and 35 minutes after adding the new osmotic media. This is to ensure that the imaging was performed before the cells re-equilibrate their shape[11,169]. Cells under iso-osmotic conditions showed similar proportions of abortive CCSs irrespective of epsin expression level **(Figure 3.6b)**. However, overexpressing epsin-EGFP led to a reduction in the percentage of abortive CCSs compared to endogenous expression or overexpression of WT epsin under iso-osmotic condition. On the other hand, when membrane tension was increased under hypo-osmotic conditions, cells expressing endogenous level of epsin showed an appreciable increase in abortive CCSs, consistent with previous findings[32]. In contrast, overexpression of WT epsin or epsin EGFP both maintained the same percentages of abortive CCSs under hypo-osmotic condition compared to iso-osmotic condition **(Figure 3.6b)**.

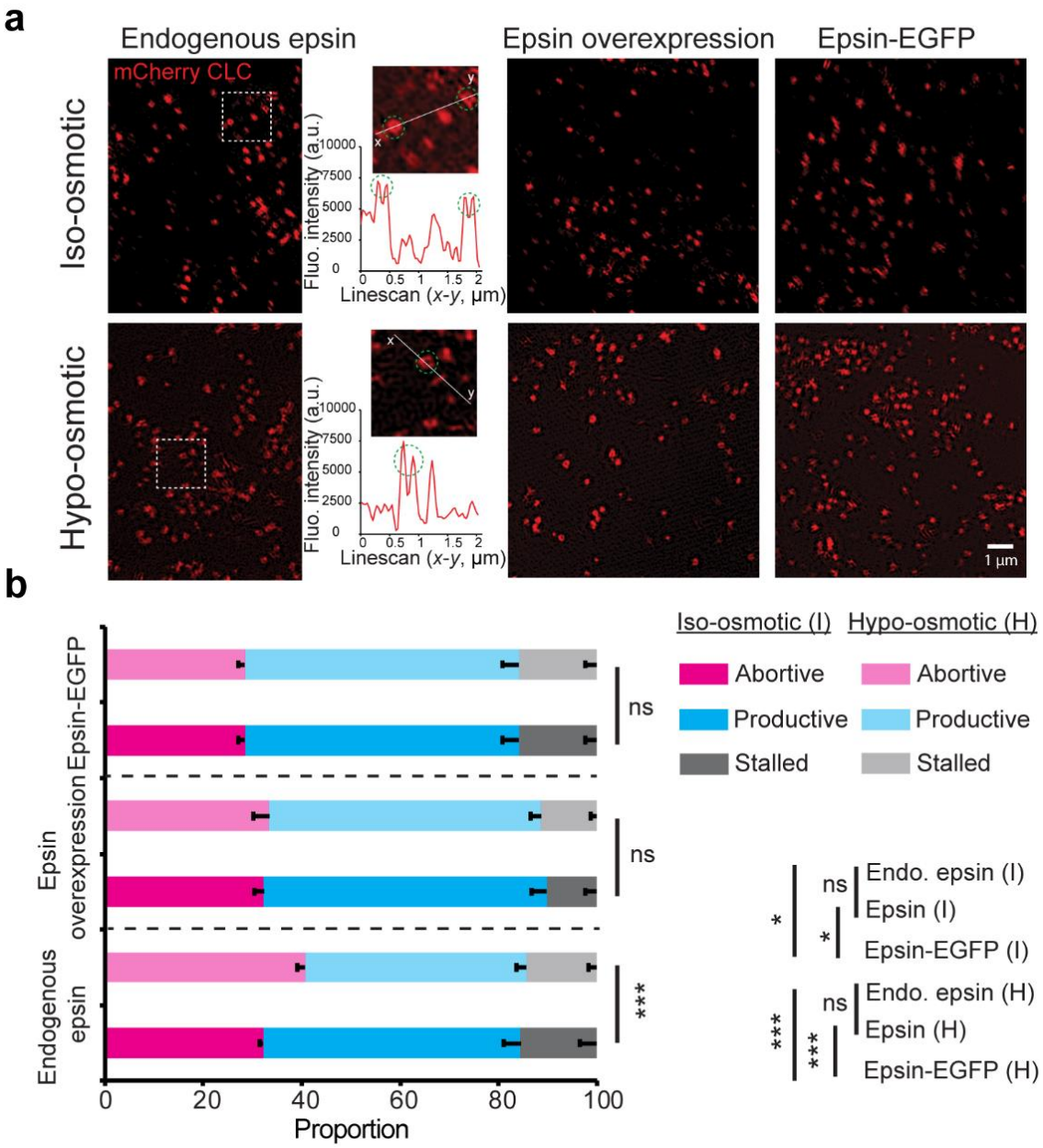

Figure 3.6. **Overexpression of epsin in RPE cells reduces population of abortive CCSs at high tension.**

a. SIM-TIRF images of clathrin in RPE cells expressing epsin at endogenous levels, overexpressing epsin, and overexpressing epsin EGFP under iso-osmotic (control- 290 mmol/kg) and hypo-osmotic (220 mmol/kg) conditions. The formation of a CCS dome (highlighted by green circles) is depicted using intensity line scans. **b.** Percentage of abortive, productive and stalled CCPs/CCSs in cells expressing endogenous epsin, overexpressing epsin, and overexpressing epsin EGFP under iso-osmotic (control) and hypo-osmotic conditions. For b, the number of CCSs analyzed for endogenous epsin, epsin overexpression, and epsin EGFP overexpression were 26,240 (iso) and 16,918 (hypo), 17,914 (iso) and 14,722 (hypo), 31,776 (iso) and 41,949 (hypo), respectively taken from 6 cells under each condition.

to cells overexpressing WT epsin. As a result, overexpression of WT epsin had a larger fraction of productive CCPs compared to epsin EGFP overexpression. Further dual color SIM-TIRF imaging of basal surface of cells and super-resolution confocal imaging of apical surface of cells show co-localization of epsin in CCPs which were productive **(Figure 3.5a and b)**. To confirm the effect of epsin expression on productiveness of CCPs, I performed transferrin uptake assay in iso- and hypo-osmotic conditions for RPE cells expressing endogenous level, overexpressing epsin, and overexpressing epsin EGFP. Normalized transferrin uptake reduced with increased membrane tension in RPE cells expressing epsin at endogenous level, whereas both overexpression of epsin

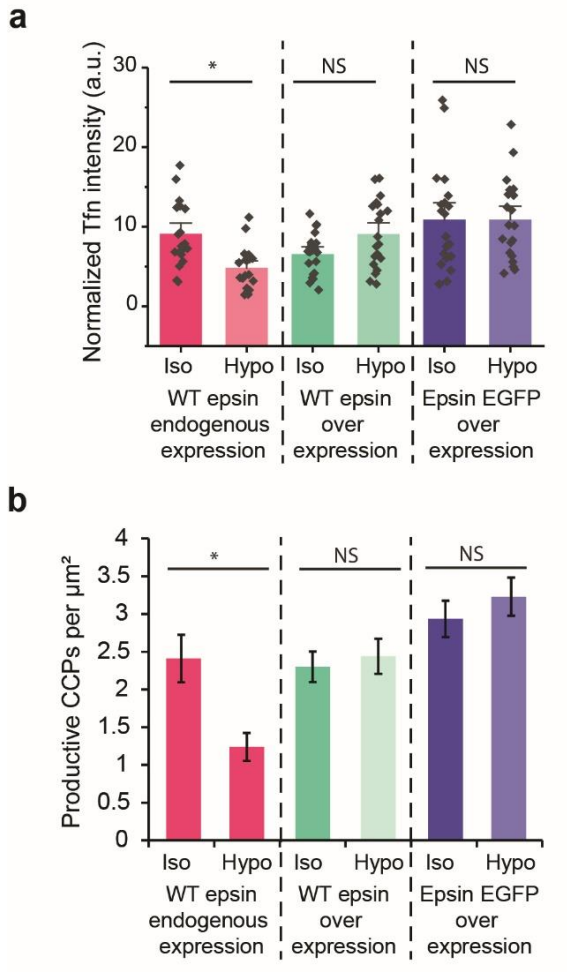

Figure 3.7. Overexpression of epsin support the formation of productive CCPs and cargo uptake at high tension.

a. Transferrin Alexa 647 intensities in RPE cells with endogenous expression of WT epsin, overexpression of WT epsin and overexpression of epsin EGFP under iso- and hypo-osmotic conditions. The intensities were normalized with bulk mCherry clathrin intensity. The number of cells for iso- and hypo-osmotic conditions were 20 each for WT epsin endogenous expression, WT epsin overexpression and epsin EGFP expression. The experiment was performed once. The error bars denote standard error. **b.** The number of productive CCPs per μm^2 of cell area in RPE cells with endogenous expression of WT epsin, overexpression of WT epsin and overexpression of epsin EGFP under iso- and hypo-osmotic conditions during 5-minute duration of SIM-TIRF microscopy. NS denotes not significant. *, **, *** represent $p < 0.05$, $p < 0.01$ and $p < 0.001$, respectively.

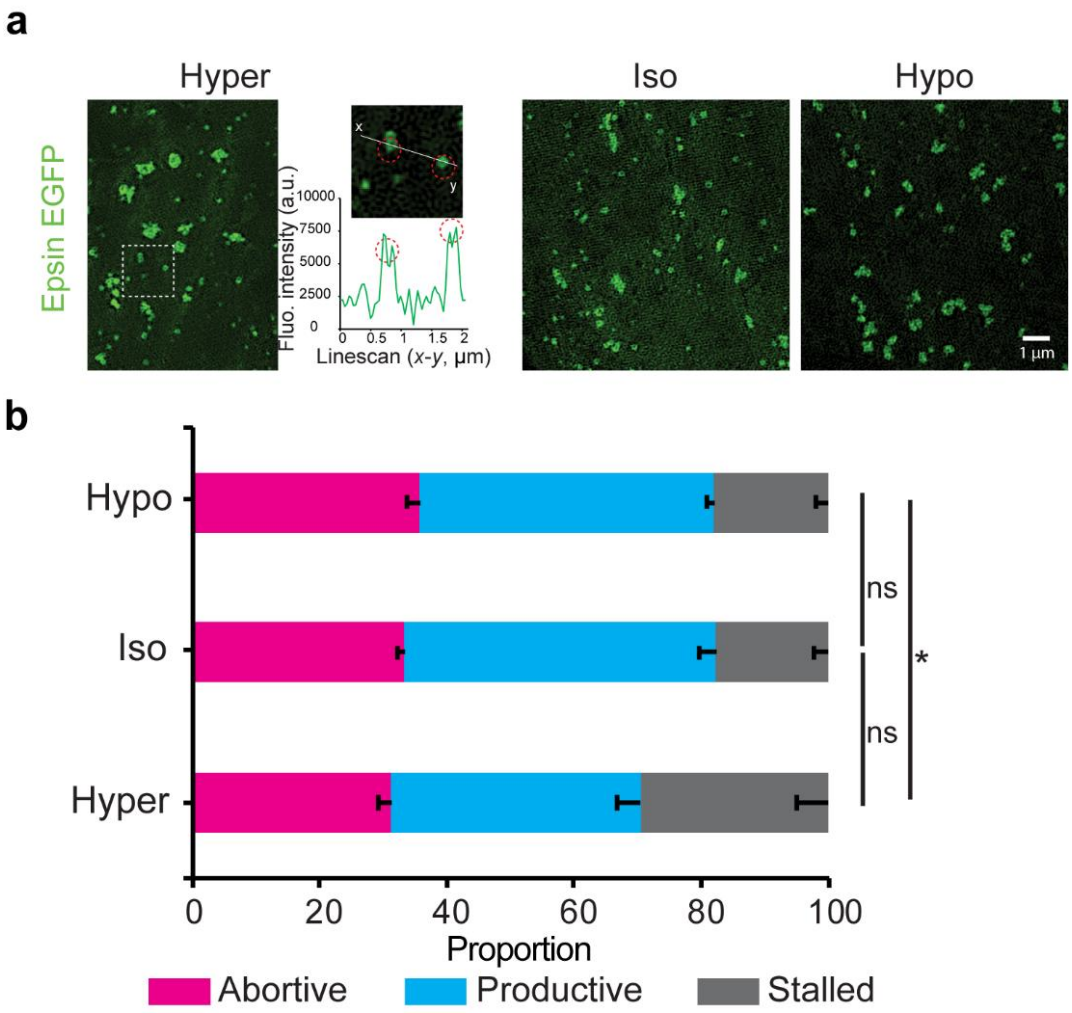

Figure 3.8. **Overexpression of epsin in RPE cells reduces population of abortive CCSs at high tension.**

a. SIM-TIRF images of epsin EGFP in RPE cells under hyper- (440 mmol/kg), iso- (290 mmol/kg) and hypo-osmotic (220 mmol/kg) conditions. The formation of a CCS dome (highlighted by red circles) is depicted using intensity line scan. **b.** Percentage of abortive, productive, and stalled epsin EGFP structures under hyper-, iso- and hypo-osmotic conditions. For b, the number of epsin EGFP structures analyzed were 31,404 (hyper), 36,536 (iso), and 31,085 (hypo), 31,776 (iso) respectively taken from 6 cells under each condition. The error bars denote standard deviation. NS denotes not significant. *, **, *** represent $p < 0.05$, $p < 0.01$ and $p < 0.001$, respectively.

WT and epsin EGFP showed no significant changes in transferrin uptake with increased membrane tension **(Figure 3.7a)**. The uptake of transferrin in iso- and hypo-osmotic conditions for RPE cells with endogenous level epsin, overexpressing epsin, and overexpressing epsin EGFP closely correlated with the nucleation density of productive CCPs **(Figure 3.7b)**. Further, membrane-

associated structures with epsin EGFP were imaged at hyper- (low tension - 440 mmol/kg osmolarity), iso- (control - 290 mmol/kg osmolarity) and hypo- (high tension - 220 mmol/kg osmolarity) osmotic conditions **(Figure 3.8a)**. As membrane tension increased, the percentage of abortive structures with epsin recruitment increased only slightly **(Figure 3.8b)**. However, at low tension, epsin recruitment resulted in CCS clustering and stalling **(Figure 3.8b)** This stalling and clustering is consistent with *in vitro* observation of epsin tabulation and clustering seen at low tension in GUVs[17,18,116,118]. Even though clusters of CCSs which are stalled remained in the TIRF field during the acquisition period, they showed dynamic rearrangement of CCS rings including merging and splitting of rings. Some clusters showed disappearance of CCSs from the boundary of the stalled clusters.

3.4.2 Epsin recruitment is increased in productive CCPs upon disrupting actin.

I repeated the osmotic shock experiments in RPE cells overexpressing epsin EGFP after disrupting actin cytoskeleton using Latrunculin A. As shown previously[26], increase in tension together with disruption of actin led to significant stalling of CCSs **(Figure 3.9a-d)**. Actin cytoskeleton supports the transition of open CCPs to form closed Ω-shaped structures which is internalized after dynamin-mediated scission[26]. The intensity of epsin increases for hypo-osmotic condition in comparison with iso-osmotic condition for productive and stalled CCSs and remained unchanged for abortive CCPs. However, when actin cytoskeleton was disrupted, intensity of epsin recruitment increases into both productive and abortive CCPs compared to the cells without actin disruption **(Figure 3.9e)**. This behavior was not seen in stalled CCSs which showed the intensity of epsin remaining unchanged for cells with or without actin disruption. The increase of epsin intensity in productive CCPs suggest that increased recruitment of epsin may rescue the

internalization of CCPs by enabling the transition of open to closed pit morphology under high tension in the absence of actin.

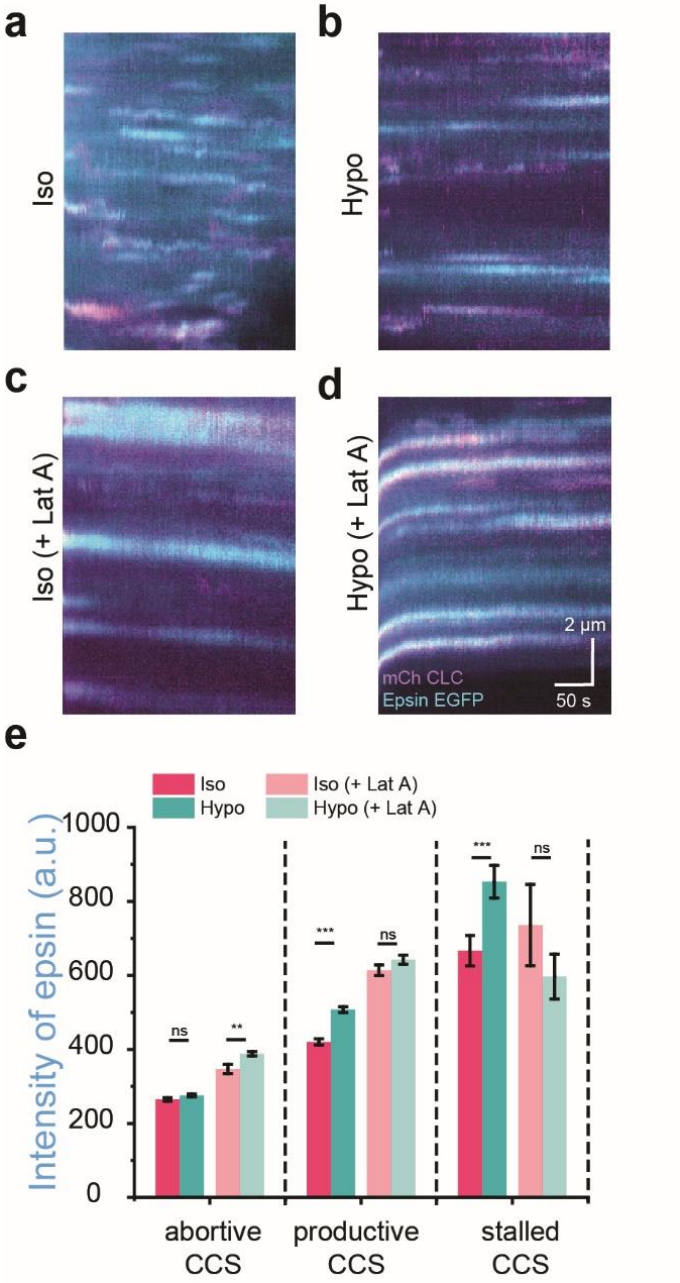

Figure 3.9. Epsin recruitment increases in CCSs under actin disruption.

Kymographs of CCSs in RPE cells overexpressing epsin EGFP (cyan) and mCherry clathrin (magenta) under, **a.** iso-osmotic condition, **b.** hypo-osmotic condition, **c.** iso-osmotic condition and 0.5 µM Latrunculin A treatment, **d.** hypo-osmotic condition and 0.5 µM Lat A treatment. **e.** Intensity of epsin for abortive, productive and stalled CCSs under iso-osmotic condition and hypo-osmotic condition with and without Latrunculin A treatment. For e, the number of cells for iso-, hypo-osmotic conditions without Latrunculin A and iso-, hypo-osmotic conditions with Latrunculin A were 12 (N_{tracks}=15235),12 (N_{tracks}=14147) and 12 (N_{tracks}= 15640), 12 (N_{tracks}= 19360) respectively. The error bars denote standard error. NS denotes not significant. *, **, *** represent $p < 0.05$, $p < 0.01$ and $p < 0.001$, respectively**.**

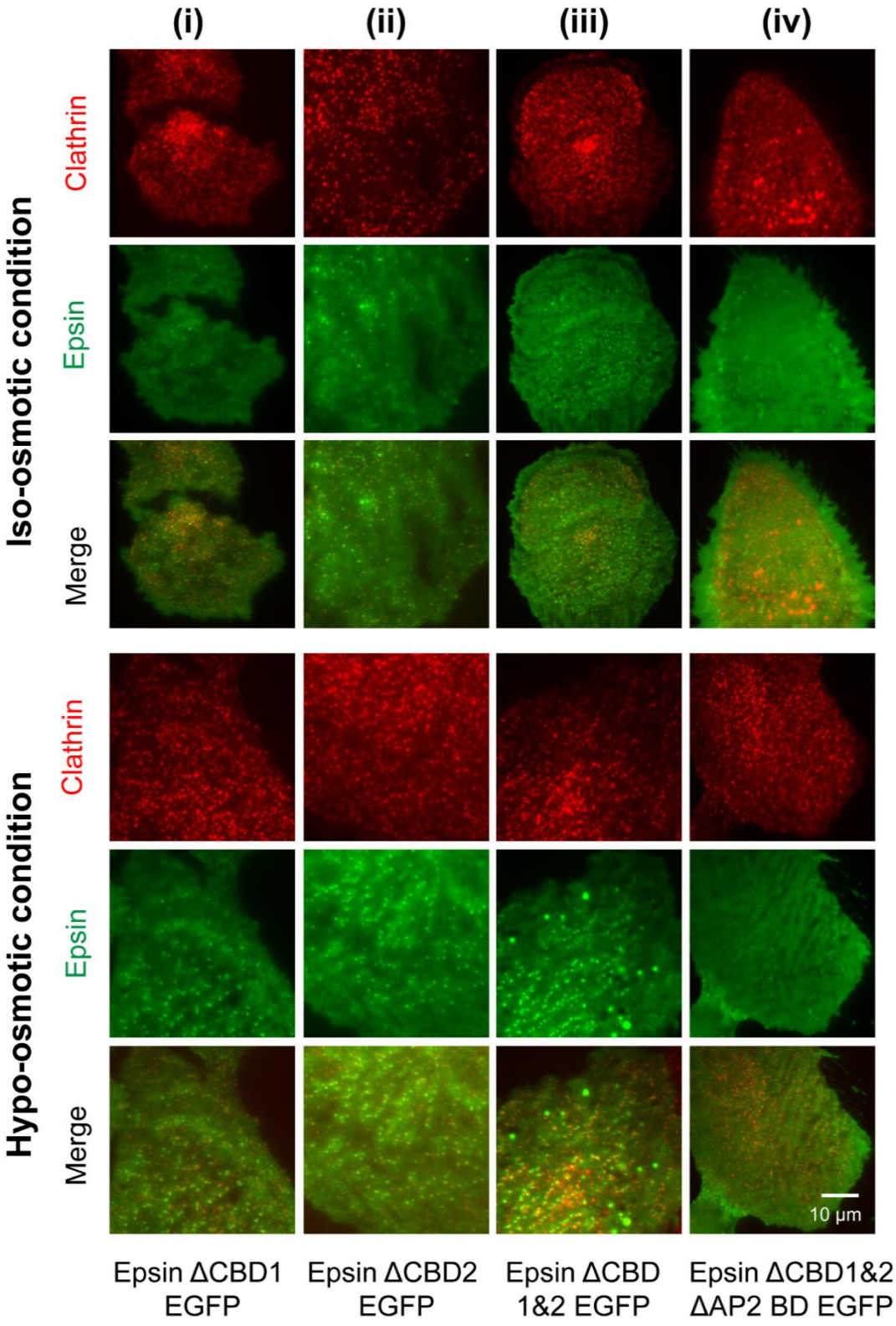
(i)
(ii)
(iii)
(iv)
Iso-osmotic condition
Clathrin
Epsin
Merge
Hypo-osmotic condition
Clathrin
Epsin
Merge
10 µm
Epsin ΔCBD1 EGFP
Epsin ΔCBD2 EGFP
Epsin ΔCBD 1&2 EGFP
Epsin ΔCBD1&2 ΔAP2 BD EGFP

Figure 3.10. Removal of AP2 and clathrin binding sites render epsin cytosolic.

Representative fluorescence images of cells overexpressing EGFP-tagged epsin and epsin mutants under iso- (top panel) and hypo- (bottom panel) osmotic conditions**.** Cells overexpressing (i) epsin ΔCBD1 EGFP, (ii) epsin ΔCBD2 EGFP, (iii) epsin ΔCBD1&2 EGFP, (iv) epsin ΔCBD1&2 and ΔAP2 binding domains EGFP along mCherry CLC is shown.

3.4.3 Endocytic protein binding sites of epsin is necessary for its stable recruitment into CCSs.

To determine which domains are responsible for the stabilization effect of epsin, I progressively removed binding domains from epsin within the unstructured IDP region **(Figure 3.1)**. Removal of clathrin binding domain (CBD) 1 (LMDLADV) or CBD2 (LVDLD) did not affect epsin recruitment into CCSs **(Figure 3.10 (i) to (iii))**[170]. Simultaneous removal of CBD1

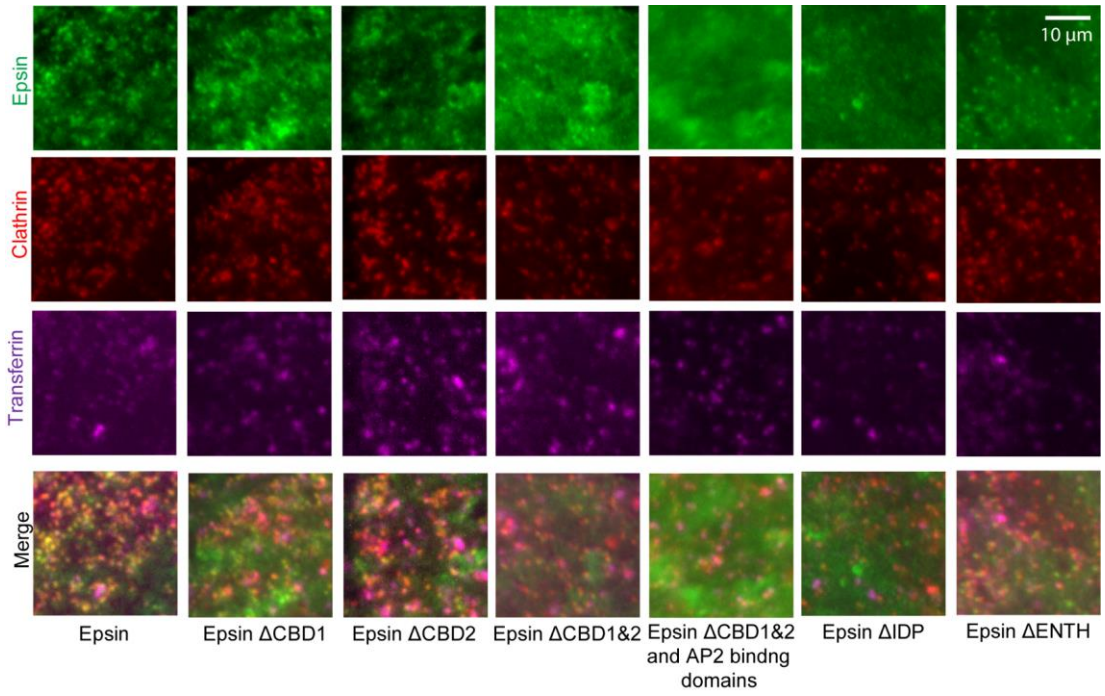

Figure 3.11. Transferrin uptake in cells overexpressing EGFP-tagged epsin and epsin mutants.

Representative fluorescence images of cells expressing epsin EGFP, epsin ΔCBD1 EGFP, epsin ΔCBD2 EGFP, epsin ΔCBD1&2 EGFP, epsin ΔCBD1&2 and ΔAP2 binding domains EGFP, epsin ΔIDP EGFP, epsin ΔENTH EGFP, along with mCherry CLC and Alexa Fluor 647 transferrin (25 µg/ml with 10 min incubation).

and CBD2 also did not inhibit formation of epsin puncta **(Figure 3.10 (iii))**, nor was the number of epsin puncta in these mutants affected by an acute increase in membrane tension *via* osmotic shock (**Figure 3.10 (i) to (iii)**, top and bottom panel). However, removal of DPW repeat motifs,

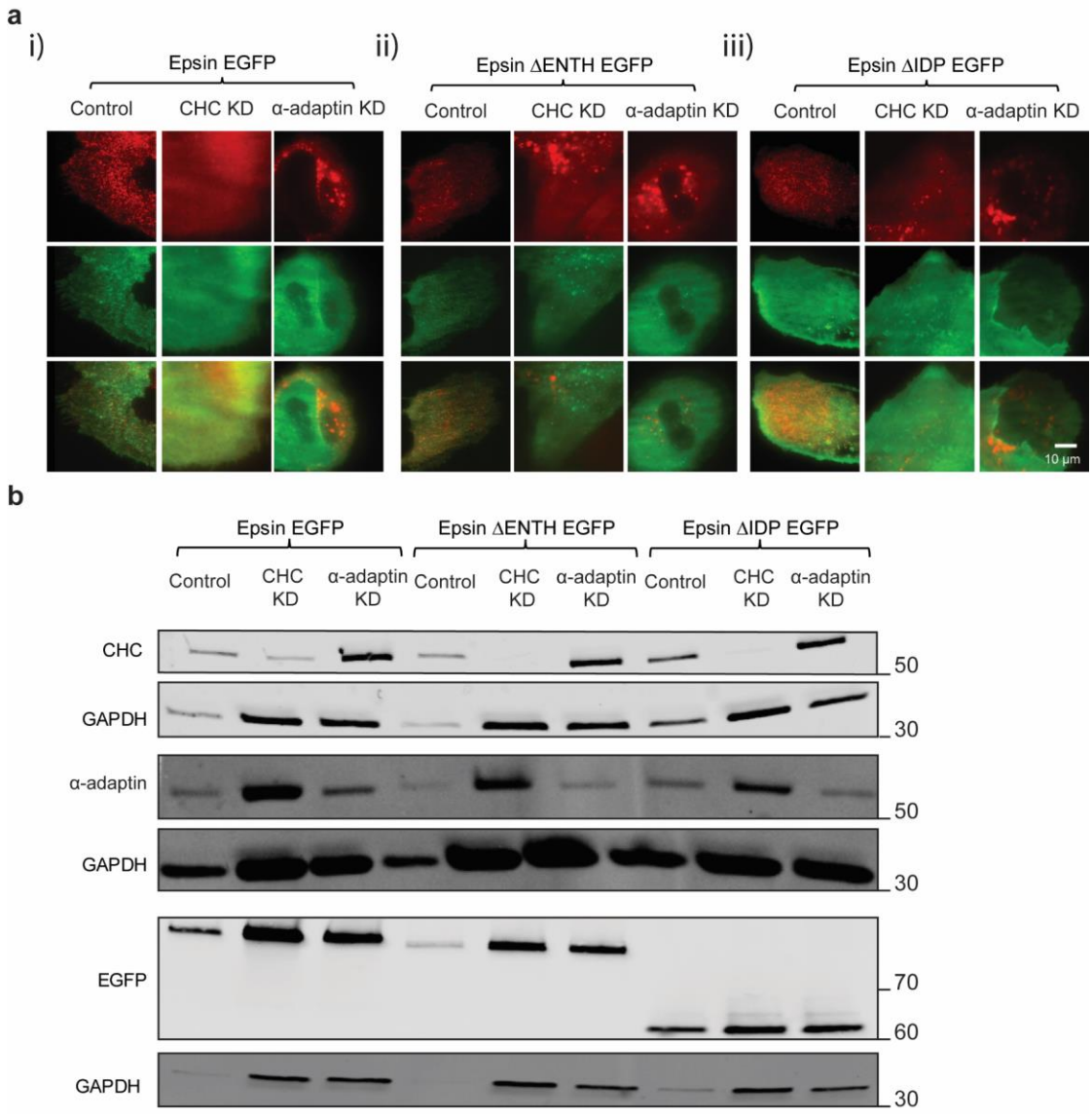

Figure 3.12. Knocking down clathrin heavy chain or AP2 subunit disrupts the recruitment of epsin..

a. Representative fluorescence images of (i) full length epsin EGFP, (ii) epsin ΔENTH EGFP and (iii) epsin ΔIDP EGFP, along with mCherry CLC in RPE cells with control (scramble shRNA), clathrin heavy chain (CHC) shRNA knockdown, and α-adaptin shRNA knockdown. **b.** Western blot showing the knockdown of CHC and α-adaptin, with GAPDH as a loading control. EGFP panel shows the expression of fusion protein epsin EGFP, epsin ΔENTH EGFP, and epsin ΔIDP EGFP.

which bind to AP2 subunit along with CBD1 and CBD2, renders epsin cytosolic **(Figure 3.10 (iv))**. Using a transferrin uptake assay, I showed that overexpression of epsin mutants did not adversely affect the cargo recruitment and internalization *via* CME **(Figure 3.11)**, suggesting that mutant epsins did not impact CME. Consistent with earlier findings, removing the unstructured IDP region of epsin containing all the endocytic binding sites also resulted in epsin being cytosolic, and this is true under all tension conditions (**Figure. 3.12a (iii)** and **Figure 3.13a**). This implies that ENTH, which is the structured domain of epsin containing H_0 helix, alone cannot stabilize epsin recruitment to CCSs, but it requires the AP2 and clathrin binding sites in the C-terminus unstructured region of the protein. This is an important result as I have shown that ENTH domain mediates tension-dependent nucleation of epsin and *in vitro* studies have shown ENTH domain alone is recruited to pre-curved lipid bilayers containing PIP_2[134,147]. To further confirm the requirement of AP2 and clathrin binding to stabilize epsin recruitment to plasma membrane, I used shRNA knockdown of clathrin heavy chain (CHC) or α-adaptin in AP2 subunit **(Figure. 3.12a and b)**. Knocking down CHC or α-adaptin that blocks the formation of CCSs also inhibited the formation of epsin puncta **(Figure. 3.12a)**. This behavior was observed in full-length epsin, epsin ΔENTH and epsin ΔIDP expressing cells. This provides support that binding of epsin to CHC and AP2 is necessary for stable recruitment of epsin and the ENTH domain alone cannot support plasma membrane recruitment (**Figure. 3.13b**).

3.4.4 Bi-directional stabilization of epsin recruitment to CCSs and curvature of CCS domes is mediated by the unstructured domain of epsin.

Productive CCPs (lifetime 20-120 s) internalize into cytoplasm without prematurely dissembling or stalling on the membrane. My SIM-TIRF data showed that overexpression of epsin supports the maturation of CCSs to productive CCPs. Furthermore, dual color SIM-TIRF data

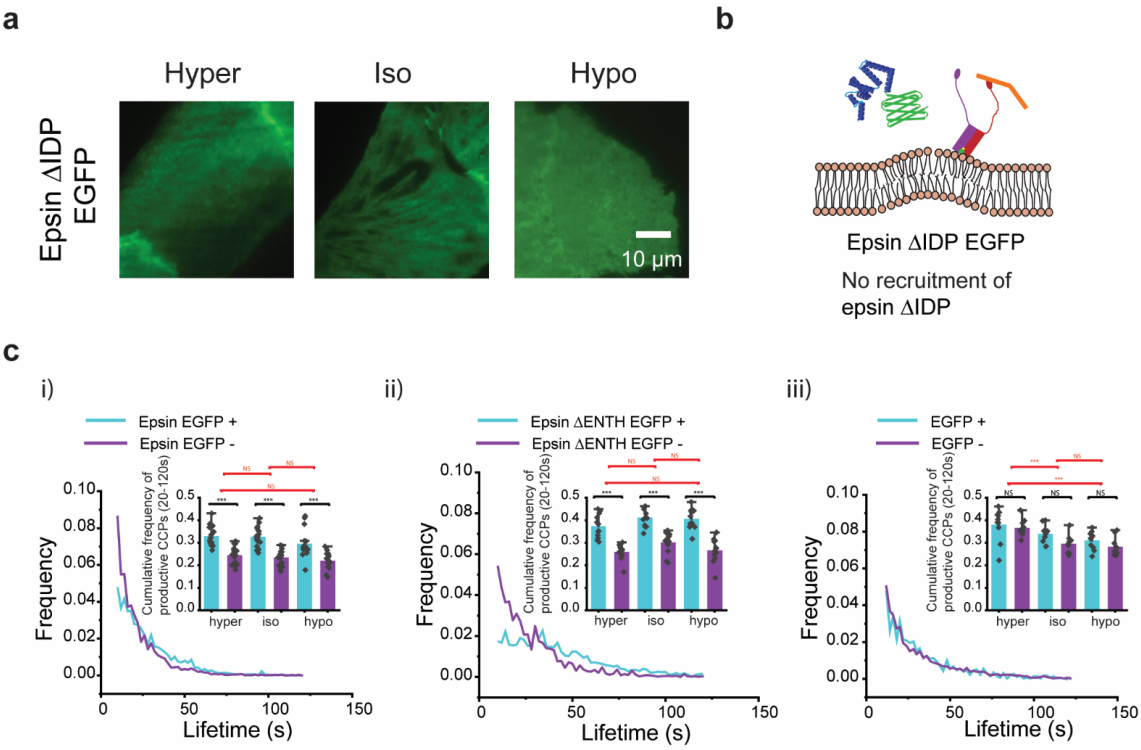

Figure 3.13. Bi-directional stabilization of epsin recruitment in CCSs and curvature of CCS domes to form productive CCSs is mediated by unstructured IDP region.

a Fluorescence images of epsin ΔIDP under different tension conditions (hyper-, iso- and hypo-osmotic conditions). **b** Proposed model of interaction between a CCS and epsin ΔIDP. **c** The lifetime distribution of CCSs with (cyan) or without (magenta) epsin EGFP for iso-osmotic condition for (i) full length epsin with C-terminus EGFP, (ii) epsin ΔENTH EGFP, and (iii) EGFP (control). Inset shows cumulative frequencies of mature CCSs with lifetimes 20-120 s for the different osmotic conditions indicated. The N_{cells} expressing epsin EGFP for hyper-, iso-, and hypo-osmotic conditions in c. were 19 (N_{tracks} = 38282), 19 (N_{tracks}= 58574), and 16 (N_{tracks} = 32644) respectively. The N_{cells} expressing ΔENTH EGFP epsin for hyper-, iso-, and hypo-osmotic conditions in c. were 12 (N_{tracks}= 19328), 12 (N_{tracks}= 20078), and 12 (N_{tracks}= 31952), respectively. The N_{cells} expressing EGFP for hyper-, iso-, and hypo-osmotic conditions in c. were 12 (N_{tracks}= 23670), 14 (N_{tracks}= 24615), and 13 (N_{tracks}= 23424), respectively. The error bars denote standard error. NS denotes not significant. *, **, *** represent $p < 0.05$, $p < 0.01$ and $p < 0.001$, respectively.

showed that the presence of epsin tagged with EGFP preferentially supports the formation of productive CCPs (shown by the preferential formation of rings when epsin is present (green) in **Figure. 3.5c**), suggesting that epsin may stabilize productive CCPs. To determine the effect of the epsin recruitment on the stability of CCSs, I classified CCS tracks as with or without co-

localization with epsin tagged with EGFP. I found that the fraction of productive CCPs in a cell is higher in epsin-containing CCPs **(Figure. 3.13c (i))**. I also found that there was no statistically significant change in the fraction of productive CCPs between hyper-, iso- and hypo-osmotic-treated cells **(Figure. 3.13c (i) inset)**. Similarly, cells having CCSs with epsin ΔENTH recruitment also showed an increase fraction of productive CCPs **(Figure. 3.13c (ii))**, again independent of membrane tension. As a control, I looked at whether cells expressing EGFP had the same fraction of productive CCPs in different tension conditions. For this analysis, I used the false positive puncta detection from the secondary channel (EGFP) to classify pits as EGFP-positive (EGFP +) and EGFP-negative (EGFP -). Comparison of the fractions of productive CCPs which are EGFP + and EGFP - showed no difference between them **(Figure. 3.13c (iii))**, unlike epsin-positive CCSs in epsin or epsin ΔENTH expressing cells which showed significant increases in the population of productive CCPs. As tension increased, the fraction of productive CCPs decreased for cells expressing only EGFP, consistent with the previous finding from my lab[32]. Altogether, these findings show that epsin supports the formation of productive CCPs. With the help of endocytic binding sites in the IDP domain that confers steric crowding, epsin is able to stabilize curvature of CCS domes. ENTH domain, however, does not play an active role in providing this stabilization effect. Together, these results demonstrate a bi-directional stabilization of epsin recruitment by binding to AP2 and CHC and stabilization of productive CCPs due to binding of epsin to AP2 and CHC, both mediated by the unstructured IDP region of epsin.

3.5 Discussion

Membrane tension is known to be a regulating factor of different endocytic pathways[26,68,108,156]. Prior experimental evidence points to actin dynamics in supporting the

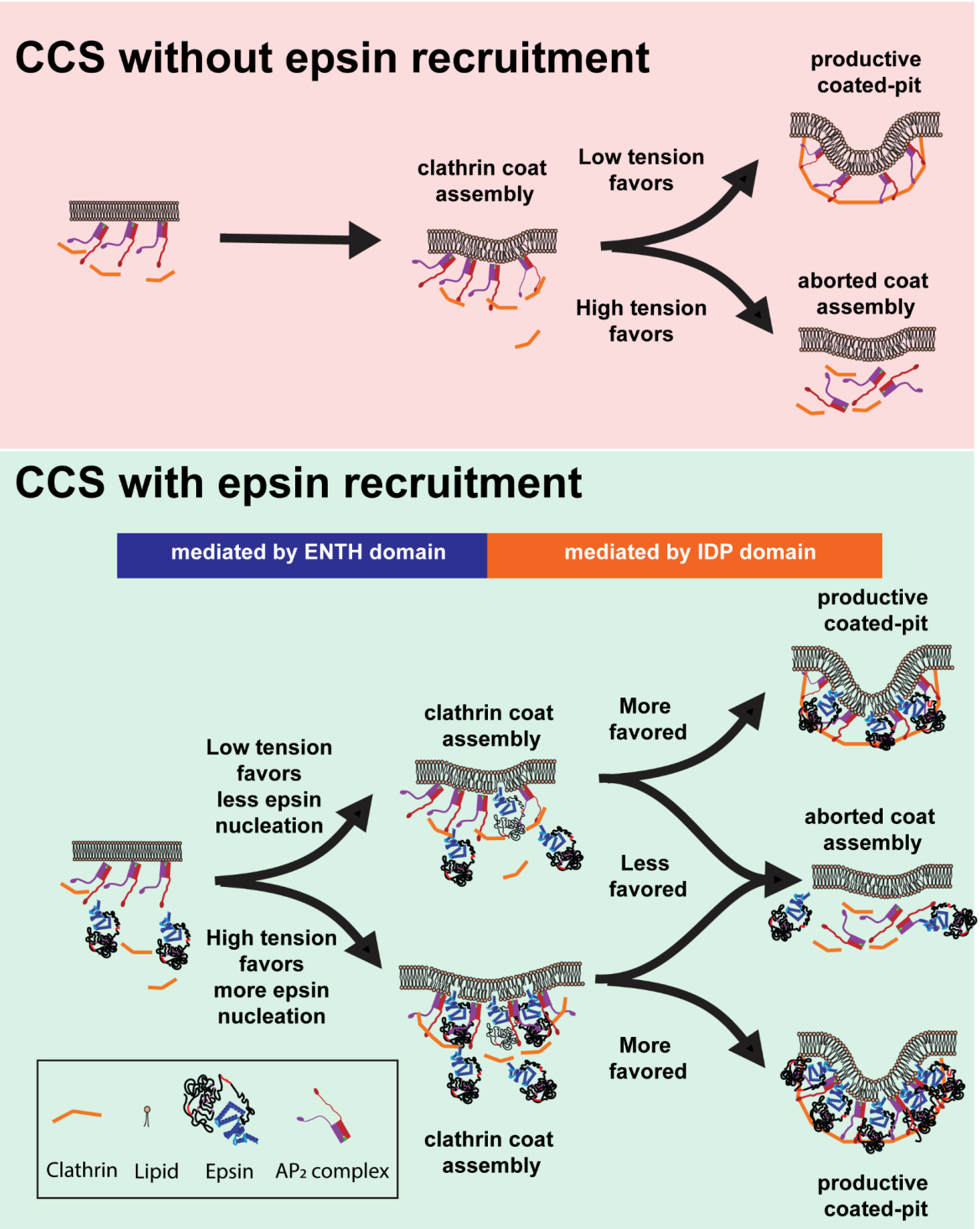

Figure 3.14. Summary of the role of epsin in CCS formation under different tension environments.

Epsin provides enhanced CCS stability compared to CCSs without epsin. At high tension, more epsin molecules are recruited to counteract elevated tension and to provide stability to CCSs. The AP2 and clathrin binding of epsin primarily impart the additional stability to coated pits by anchoring constituents of CCS complex together.

tension[26]. However, it has been puzzling how cells overcome the transition from flat membrane to hemispherical domes during CME at high tension. The exact mechanism of curvature formation in CCPs is hotly debated[11,126,168,171] and whether membrane tension and presence of membrane bending proteins during CCP initiation control fate of the CCP is an open question. Here I uncovered epsin's ENTH and IDP domains play complementary roles to ensure the completion of CCS maturation under high tension environments **(Figure 3.14)**.

Under a SIM-TIRF field, a productive CCS track shows evolution of the hemispherical dome manifested as a ring[168]. I found that overexpressing epsin or epsin EGFP in cells support the maturation of coated pits at high tension. Utilizing dual-color TIRF imaging, I showed that epsin EGFP recruitment into CCSs increases with an increase in resting membrane tension or acute membrane tension. I showed that masking ENTH domain activity in epsin (i.e. by placing EGFP at the N-terminus end of epsin) blocks the early recruitment of epsin to the CCS sites. The IDP domain provides binding to AP2 and clathrin, which is required for epsin's ability to stabilize CCSs, since ENTH domain alone is cytosolic. My finding is important as most membrane-associated proteins disassemble or dissociate from the lipid bilayer as membrane tension increases[32,68,82]. The complementary actions of ENTH and unstructured IDP region of epsin enable it to detect membrane tension variations to support the flat-to-dome transition in high tension environments. Interestingly, I find that epsin is recruited early before clathrin, in contrast to what Taylor *et al.* reported[150]. This is due to the fact that Taylor *et al.* used a N-terminus epsin fusion protein which blocks ENTH function. Thus, my findings would be consistent with ENTH's role in tension sensing.

Previously, Brady *et al.* showed that both ENTH and C-terminal domain of epsin regulate its dynamic interaction with CCSs in *Dictyostelium*[172]. Similarly, work in yeast from the

Wendland lab have shown that ENTH domain of epsin is essential for endocytosis by binding to phosphoinositides and other endocytic constituents like clathrin as well as playing a role in downstream signaling through Cdc42 signaling pathway[173–175.] In contrast, my experiments showed that the C-terminus IDP domain that contains AP2 and clathrin binding sites are sufficient for epsin to target to CCSs. Further, Zeno *et al.* found that disordered domains enhance curvature sensitivity of structured domains[147]. Similarly, I found that the synergy between a structured (i.e. ENTH) domain and an unstructured (i.e. IDP) domain can achieve membrane tension sensing[147].

Although the H_0 helix can insert into the membrane and acts as the tension sensor, my data does not support that ENTH alone as the curvature generation machinery. The ability of the unstructured IDP region to tether different endocytic proteins (AP2, clathrin), besides generating steric pressure, is partly responsible for the stabilization effect of CCSs under high tension (i.e., epsin-positive CCSs have a larger fraction of productive structures). I speculate that steric repulsion by the bulky unstructured IDP region also plays a role in inducing and stabilizing the curvature of the dome structure[17,18]. While stable epsin recruitment to CCSs requires the presence of CHC and AP2, once epsin is recruited to CCSs it supports the formation of CCS dome with the help of its unstructured IDP region. Interestingly, cells overexpressing epsin-EGFP have more productive/stalled CCSs under high tension compared to cells overexpressing epsin. The EGFP following the unstructured IDP region increases its bulkiness and therefore steric pressure. My work implies the existence of a bi-directional stabilization between endocytic components of CCSs and IDP-mediated curvature generation.

Elevated membrane tension plays an inhibitory role in CME[27,28]. I believe cargo uptake via CME is dependent on the total number of productive CCPs on the cell membrane. Transferrin

uptake in cells reduced as membrane tension increased in RPE cells with endogenous level epsin. My SIM-TIRF data showed that increase in membrane tension reduced the number of productive CCPs in RPE cells. However, the number of productive CCPs did not reduce when epsin was overexpressed. This result is in good agreement with my transferrin uptake assay which showed similar rate of uptake for cells overexpressing epsin under different membrane tension conditions. This reinforces my finding that epsin plays an integral role in membrane curvature stabilization under high tension which is necessary for the formation of productive CCPs.

It has been suggested recently that lowering membrane tension increases caveolar cluster formation[83]. Interestingly, there appeared to be more clusters of CCSs in my SIM-TIRF images under hyper-osmotic conditions. Although clusters of CCSs have been postulated to be non-terminal endocytic events[125], it will be intriguing to see if these represent local hot spots where membrane tension is low. There exist multiple endocytic proteins like AP2 and FCHo that perform the same function of membrane curvature generation and stabilization in CME[11,106,176]. Further, epsin is not expressed at elevated levels in all cell types. There were also a significant proportion of CCPs which did not have epsin recruitment. Hence, more research should be done in exploring the presence of these redundant membrane sculpting mechanisms in CME. It will also be interesting to know how the arrival time of different adaptor proteins may regulate their membrane bending capabilities. It may be the case that different membrane bending proteins may facilitate curvature generation and stabilization in a spatiotemporally regulated manner[39,150,156].

Finally, how might epsin's recruitment to CCSs under high tension be important to cell physiology? Changes in cell tension are expected to trigger various cell signaling responses. Epsin has a ubiquitin-interacting motif (UIM) with the dual function of binding ubiquitin and promoting ubiquitylation. Thus, regulating epsin recruitment to CCSs has important implication

of ubiquitinated cargo endocytosis[130] and signaling. The association of epsin with ubiquitinated cargo is negatively regulated by clathrin[177]. An increase in resting cell tension increases epsin recruitment and decreases clathrin recruitment. Coupled with the increased stability of epsin-positive CCSs, my findings would suggest that high membrane tension would impact ubiquitinated cargo endocytosis and signaling. The intersection of mechanosensing and endocytic regulation remains an under-studied area that will have profound implications in mechanotransduction.

3.6 Acknowledgments

J.G.J., A.A. and A.P.L. conceived the study, J.G.J., C.O., A.A., A.P.L. designed the experiments, J.G.J. and V.Y. performed the experiments. J.G.J acknowledge Aaron Taylor and Eric Rentchler from UM microscopy core for helping us with TIRF-SIM imaging. This work was supported by the National Science Foundation NSF-MCB 1561794 to A.P.L. and NSF grants CMMI 1562043 and CMMI 1727271 to A.A.

Chapter 4 Biomechanical Role of Epsin in Influenza A Virus Entry

4.1 Abstract

Influenza A virus (IAV) utilizes clathrin-mediated endocytosis for cellular entry. Membrane bending protein epsin is a cargo-specific adaptor for IAV entry. Epsin interacts with ubiquitinated surface receptors bound to IAVs via its ubiquitin interacting motifs (UIMs). My investigation shows that CALM, a structurally similar protein to epsin lacking UIMs shows weaker recruitment to IAV-containing clathrin-coated structures (CCSs) compared to epsin. Removal of ENTH domain of epsin containing the N-terminus H_0 helix, which detects changes in membrane curvature and membrane tension, reduces the ability of epsin to be recruited to IAV-containing CCSs. In agreement with this finding, mutations in ENTH domain preventing the formation of H_0 helix also led to reduction in recruitment of epsin to IAV-bound CCSs and subsequent reduction in internalization of spherical IAVs. However, internalization of filament-forming IAVs were not affected by the inhibition of H_0 helix formation in ENTH domain of epsin. Together, these findings support the hypothesis that epsin plays a biomechanical role in IAV entry.

4.2 Introduction

Clathrin-mediated endocytosis (CME) plays an essential role in signal transduction and nutrient uptake in eukaryotic cells[7]. CME is the most frequent mode of entry for small and medium-size viruses like Influenza A virus, Semliki Forest virus, Foot-and-mouth disease virus, vesicular stomatitis virus, Rhinovirus (HRV2) and Adeno 2 virus[178]. Further, viruses like SARS-

CoV2, HIV and Dengue virus use CME as one of their modes of cellular entry[179–183]. Most of these viruses cause serious illness in humans and livestock, and present a major challenge to global health care system and economy[184–188]. Viral entry via CME is an energetically costly biomechanical process involving plasma membrane wrapping and clathrin-coat assembly around the virus particle[36,189,190]. The shape, size, stiffness and other physical characteristics of the particle control the energy requirement of this process[156,189–191]. The mechanisms that drive the internalization of these viral particles are not completely understood, specifically how the physical properties of the virus influence the internalization via receptor-mediated endocytosis. Better understanding of the biomechanics of viral entry is necessary not only in developing better therapeutics against infectious diseases, but also in designing viral vector and nanoparticle-based drug delivery systems[192–195].

In this chapter, I will explore the internalization of Influenza A virus (IAV) via CME pathway. Influenza is a major challenge to public health due to the associated hospitalizations, mortality risk as well as the frequent appearance of new strains capable of causing pandemics[187,196]. IAVs bind to sialic acid on the cell surface and are internalized through multiple endocytic pathways[197]. Currently it is not known which specific sialic acid-containing receptor binds to IAV hemagglutinin (HA) to trigger endocytosis of the virion[197,198]. It is postulated that IAV receptors exhibit strong cell tropism or they use more than one receptor for entry[197]. But it is known that IAVs elicit downstream signaling in cells via phosphorylation and ubiquitination of surface receptors[199,200]. The majority of plasma membrane bound IAVs utilize CME for cellular entry[201], and it has been shown that IAVs uses epsin-1 as a cargo specific adaptor for cellular entry via CME[130]. Ubiquitin interactive motifs (UIMs) in epsin 1 bind to ubiquitinated cell surface receptors at the site of IAV binding leading to the internalization of IAVs via CME.

In Chapters 2 & 3, I discussed the role of epsin 1 in promoting and stabilizing clathrin coat assembly at high membrane tension conditions. I showed that H_0 helix in the N-terminus of epsin acts as a tension sensor. Previous works have shown that H_0 helix in ENTH/ANTH proteins can detect and generate membrane curvature[127,134]. I hypothesize that in addition to being cargo specific adaptor for IAVs, epsin 1 also plays a biomechanical role in curvature and clathrin coat assembly stabilization during the viral entry via CME. Clinical isolates of IAVs have filamentous virions compared to spherical laboratory strains, and research have suggested that different endocytic pathways are may be utilized by the IAV strains to internalize based on their particle morphology[202–204]. By utilizing the curvature sensing ability of H_0 helix, epsin may enable the entry of IAVs of different morphology via CME by detecting the local change in membrane curvature upon viral binding. In this chapter, using full-length epsin and epsin mutant without functional H_0 helix as well as IAVs of different morphologies, I investigated the biomechanical role of epsin in IAV entry. I used live cell lattice light sheet microscopy to image the viral entry via apical and basal surface of RPE cells. Further, I quantified the co-localization of epsin and its mutant with different strains of IAVs using TIRF microscopy and 3D-SIM (structured illumination microscopy). The bulk uptake of different strains of IAVs into RPE cells expressing proteins of interest were quantified using flow cytometry.

4.3 Materials and Methods

4.3.1 Cells and reagents

Stable RPE cells overexpressing WT epsin or expressing epsin EGFP or epsin EGFP mutants and mCherry clathrin light chain (Clc) were generated as described in Chapters 2 and 3. Stable cells expressing EGFP Clc were transiently transfected with CALM mCherry (Addgene). For

transfection, cells at 70% confluency were transfected with the desired DNA constructs using lipofectamine 2000 (Invitrogen) in Opti-MEM (Gibco). These cells were cultured in Dulbecco's Modified Eagle Medium with nutrient mixture F-12 (DMEM/F12) supplemented with 10% (v/v) fetal bovine serum (FBS) and 2.5% (v/v) penicillin/streptomycin at 37°C and 5% CO_2.

4.3.2 Generation of Influenza A Virus strains with different morphologies

Influenza A virus (H3N2: strain A/Aichi/2/68) was purchased from ATCC. Influenza A viruses H1N1: A/WSN/1933 and its mutant strains were generated by Akira Ono's Lab (University of Michigan). WSN WT, a lab adapted strain of H1N1: A/WSN/1933 strain was generated by Ono lab utilizing a reverse genetics sytem[205] by transfecting HEK293T cells with 8 genome segment of Influenza virus followed by further propagation in MDCK culture. Viruses of different morphology were generated by replacing the M segment encoding M1 and M2 structural proteins of IAV[206]. WSN WT strain is known to produce spherical IAV morphology. WSN-UdM strain which forms filamentous IAVs were generated by replacing M segment of WSN-WT with M segment of H3N2: A/udorn/1972 strain[206] **(Figure 4.1)**. Isogenic control (WSN-UdM1A) of WSN-UdM was generated by point mutation in M segment of WSN-UdM which abrogate the ability of producing filamentous particles. Plaque forming units (p.f.u), which show the viral titer of IAV variants were determined using plaque formation assay.

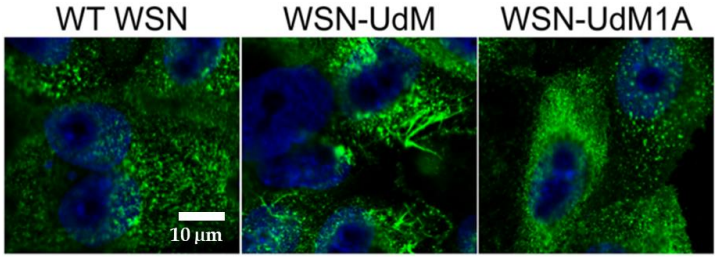

Figure 4.1. Spherical and filamentous IAV morphologies.

MDCK cells producing spherical (WSN WT), mixed population of filamentous and spherical (WSN-UdM) and isogenic spherical (WSN UdM1A) IAVs. Signal are detected by immunostaining for HA (non-permeabilized). Images obtained by Ono Lab.

4.3.3 Fluorescence labeling of IAV

IAVs were labeled with lipophilic dye DiD (Invitrogen). 100 µL original virus stocks of each strain were incubated with 1 µL of 1 mM DiD dissolved in DMSO at room temperature with gentle vortexing. Unincorporated dye was removed by centrifugation at 5000 *g* followed by media exchange using Amicon Ultra-15 centrifugal filter units (MilliporeSigma). Labeled IAVs were visualized using epi-fluorescence microscopy (**Figure 4.2**).

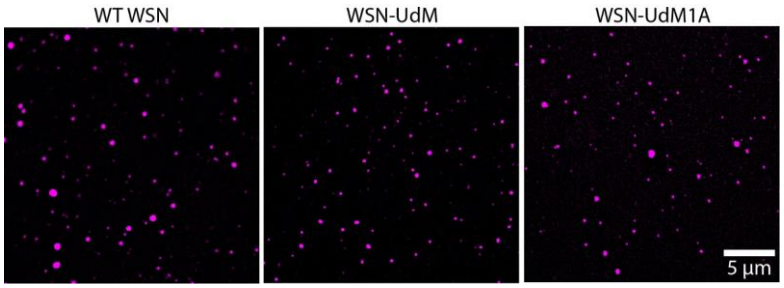

Figure 4.2. Fluorescence labeled IAV particles.

WSN WT, WSN-UdM and WSN-UdM1A IAV particles labeled with DiD lipophilic dye.

4.3.4 Actin cytoskeleton disruption

RPE cells overexpressing epsin EGFP or epsin mut-H_0 EGFP and mCherry Clc were incubated with Latrunculin A (0.5 µM) (Thermo Fisher Scientific) for 30 minutes at 37 ºC for disrupting actin cytoskeleton prior to influenza viral infection.

4.3.5 Inhibiting clathrin-mediated endocytosis

RPE cells stably expressing epsin EGFP or epsin mut-H_0 EGFP and mCherry Clc were incubated with Pitstop 2 (20 µM) (Abcam) for 15 minutes at 37 ºC for inhibiting CME prior to influenza viral infection.

4.3.6 TIRF microscopy

RPE cells stably expressing epsin EGFP or epsin EGFP mutants and mCherry Clc or transiently expressing CALM mCherry and EGFP Clc were seeded on glass-bottom dishes (#1.5,

Mat-tek Corp.) 12 to 16 h prior to experiment. DiD tagged Influenza A virus ($7 – 8 \times 10^6$ PFU/ml) were added to the dishes and incubated at 37^oc for 1 h. Immediately after, the cells were washed with PBS and fixed using 4% paraformaldehyde for 10 min on ice. TIRF microscopy was performed to image the colocalization of IAVs at the basal layer of cells using a Nikon TiE-Perfect Focus System (PFS) microscope equipped with an Apochromat 100X objective (NA 1.49), a sCMOS camera (Flash 4.0; Hamamatsu Photonics, Japan), and a laser launch controlled by an acousto-optic tunable filter (AOTF). Fixed Cells were imaged at 100 ms exposure with excitation of 488 nm (EGFP), 561 nm (mCherry), 640 nm (DiD) lasers (Coherent Sapphire).

4.3.7 3D structured illumination microscopy

RPE cells stably expressing epsin EGFP or epsin mut-H_0 EGFP and mCherry clathrin were seeded on 8-well chamber culture slide (#1.5, Nunc Lab-Tek) 12 to 16 h prior to each experiment. Cells were infected with labelled WSN-WT and WSN-UdM IAVs for 1 hr. Immediately after, the cells were washed with PBS and fixed using 4% paraformaldehyde for 10 min on ice. 3D-SIM was performed using a Nikon N-SIM microscope equipped with an Apochromat 100X objective (NA 1.49) and a sCMOS camera (Flash 4.0; Hamamatsu Photonics, Japan). Images were acquired in 3D SIM mode with nine images taken at each z depth of 200 nm of each color with linear translation of Moire pattern for SIM reconstruction. EGFP epsin, mCherry clathrin and DiD labelled IAVs were acquired at each z-step with 488 nm, 561 nm, and 640 nm excitation at exposure times of 100 ms, 100 ms and 50 ms respectively.

4.3.8 Live-cell lattice light sheet microscopy

RPE cells stably expressing epsin EGFP or epsin mut-H_0 EGFP and mCherry clathrin were seeded on 8-well chamber culture slide (#1.5, Nunc Lab-Tek) 12 to 16 h prior to each experiment. DiD tagged Influenza A virus (7 – 8 x 10^6 PFU/ml) were added to each well and immediately mounted on the microscope. Viral entry to the whole cell volume was imaged for a duration of 30 min using ZEISS lattice lightsheet 7 (44.83X/1.0 NA Objective at 60^o angle to the cover glass, Pco.edge 4.2 CLHS sCMOS camera). The whole volume of a cell was imaged in 30 s with an acquisition sequence of 15 ms exposure for 488 nm, 561 nm and 640 nm excitations at individual imaging depth. Lightsheet images were deskewed, deconvolved, drift corrected and transformed to cover glass orientation using Zeiss Zen 3 software. Deskewed, transformed image in cover glass orientation has a voxel size of 145 nm x 145 nm x 145 nm.

4.3.9 Colocalization analysis for fixed cells.

IAVs and CCS puncta with proteins of interest were detected by performing Gaussian mixture model fitting using custom-written software in Matlab (MathWorks Inc.) as previously described in Aguet et al[15]. Percentage of IAVs colocalized with epsin, epsin mutants, CALM and Clc were calculated. If detection mask of individual IAVs overlapped with detection masks of protein puncta, such IAVs were counted as colocalized with the corresponding protein. Further, the strength of recruitment of proteins to IAV-containing CCSs were determined. Around each detected IAV colocalized with proteins of interest, an annulus region was considered with an outer-radius two times and inner-radius equal to the radius of the IAV. Ratio of average intensity of proteins in the IAV puncta and in the annulus region around IAV was calculated. Proteins were considered preferentially recruited to the IAV puncta if the intesity ratio was greater than 1. The

intensity ratio of the epsin, epsin mutants, CALM and Clc were compared to determine the relative strength of recruitment.

4.3.10 IAV particle tracking for lattice light sheet microscopy

Individual trajectories of IAVs were detected and tracked using Trackmate plugin in FIJI (ImageJ)[163] from the deskewed and transformed 3D time lapse images of viral entry. A detector with Laplacian of Gaussian filter is applied to detect IAVs with a quadratic fitting scheme for subpixel localization and estimated blob size parameter of 3 µm. A simple Linear Assignment Problem (LAP) tracker was applied with a maximum linking and gap closing distance of 3 µm and maximum gap closing of 2 frames. Using a custom written software in MATLAB (Mathworks Inc.), time-lapse montage of IAV particle images (3 x 3 µm) overlayed with corresponding epsin EGFP and mCherry Clc images were generated by utilizing the spatial and time coordinate of IAVs tracked by Trackmate. Subsequently, using edge detection, epsin and clathrin puncta in the montage co-localizing with the IAV tracks were detected. An IAV track was considered colocalized with epsin or clathrin if it had overlapping epsin or clathrin puncta in more than three consecutive frames. IAV tracks were classified into three population, (i) IAV tracks which are clathrin and epsin positive, (ii) IAV tracks which are clathrin positive and epsin negative, (iii) IAV tracks which are clathrin and epsin negative.

4.3.11 Flow cytometry

RPE cells expressing different epsin constructs were plated in 24 well plates 12 to 16 h prior to each experiment. Cells were infected with DiD-tagged Influenza virus ($7 – 8 \times 10^6$ PFU/ml) at 37 ºC for a time course from 1 h to 4 h. Immediately after, the cells were washed with PBS and lifted with trypsin EDTA (0.25%, Gibco), and resuspended in 4% paraformaldehyde fixing

solution for 10 min on ice. Cells were analyzed by Guava EasyCyte Flow cytometer for IAV uptake. Flow cytometry data was analyzed using Flowing Software (Turku Bioscience).

4.4 Results

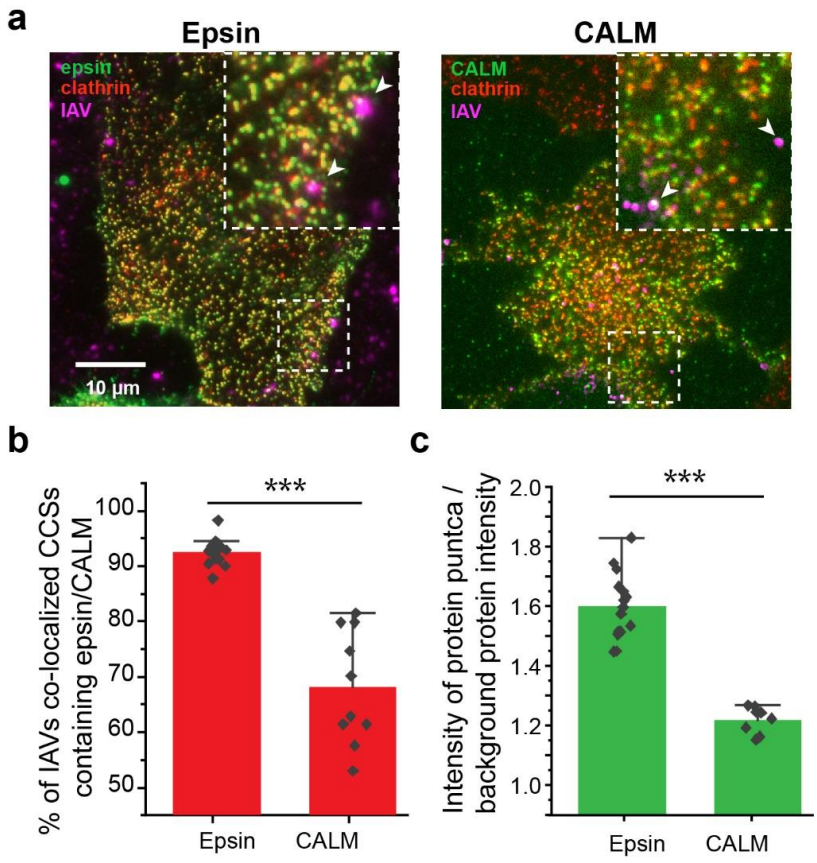

Figure 4.3. Colocalization of IAVs to ENTH/ANTH proteins containing CCSs.

a. IAVs bound to surface of RPE cells overexpressing epsin EGFP or CALM mCherry. White arrows in inset shows IAVs bound to cell surface **b.** Percentage of IAVs colocalizing with epsin and CALM to the total number of IAVs bound to the surface. **c.** Ratio of puncta intensity to background intensity of proteins colocalized with surface bound IAVs. For b and c, N_{cells} expressing epsin EGFP were 15 and N_{cells} expressing CALM mCherry were 10. The error bars denote standard error. *** represent $p < 0.001$.

4.4.1 IAVs co-localize with clathrin-coated structures (CCSs) containing ENTH/ANTH proteins.

Influenza A virus is known to enter cells via CME by hijacking the activity of endocytic associated proteins[201,207]. ENTH/ANTH proteins play an important role in membrane curvature formation during CME[133,208]. To study how ENTH/ANTH proteins are involved in IAV entry, I utilized stable RPE cells expressing epsin EGFP, an ENTH family protein or transiently expressing CALM mCherry, an ANTH

family protein. Both RPE clones stably expressed mCherry Clc or EGFP Clc respectively and allowed me to track CCSs. These cells were infected with DiD-labelled IAVs (H3N2: strain A/Aichi/2/68) for 1 h, before fixation. The cells were imaged using TIRF microscopy to determine colocalization of IAVs with epsin EGFP or CALM mCherry (**Figure 4.3a**).

Colocalization analysis of IAVs with epsin EGFP shows 90% of IAVs localizing in CCSs containing epsin (**Figure 4.3b**). Colocalization of IAVs with CALM mCherry-containing CCSs were lower at around 65%. Further, the strength of recruitment of epsin or CALM to IAVs was measured by quantifying the ratio of intensity of protein puncta versus the background protein intensity of CCSs containing epsin or CALM colocalized with an IAV. This ratiometric quantification showed higher recruitment of epsin compared to CALM to CCSs budded at IAV binding sites. Even though CALM is structurally similar to epsin, it does not possess UIMs which is shown to interact with ubiquitinated surface receptors bound to IAVs[130,133]. Both results confirm earlier findings that epsin is a cargo-specific adapter for CME of IAVs[130].

4.4.2 Bulk uptake of IAVs is not affected by the overexpression of WT epsin in RPE cells.

I utilized flow cytometry to study the bulk uptake of DiD labelled IAVs (H3N2: strain A/Aichi/2/68) by RPE cells expressing different epsin constructs. I looked at the rate of uptake with time and found that IAV uptake increased from 0 h to 1 h to 4 h as expected (**Figure 4.4a**), in epsin EGFP overexpressing RPE cells. About 10% of RPE cells overexpressing epsin EGFP internalized DiD-labelled IAVs after 1 hour of incubation. About 25% of RPE cells overexpressing epsin EGFP had internalized IAV at the end of 4 hour incubation. To study whether overexpression of epsin increase the internalization of IAVs, RPE cells expressing endogenous level of epsin and overexpressing epsin WT were incubated with DiD labeled IAVs for 4 hours. Contrary to what was expected, overexpression of wild type epsin did not increase the uptake of IAVs compared to

RPE cells with endogenous expression (**Figure 4.4b**). Around 23% of RPE cells with endogenous expression and 22% of RPE cells with epsin WT overexpression clones had internalized IAVs at the end of 4 hour. This result also confirm the findings of Chen and Zuang[130] which showed the expression level of epsin do not control the rate of infection of IAVs in BSC-1 cells.

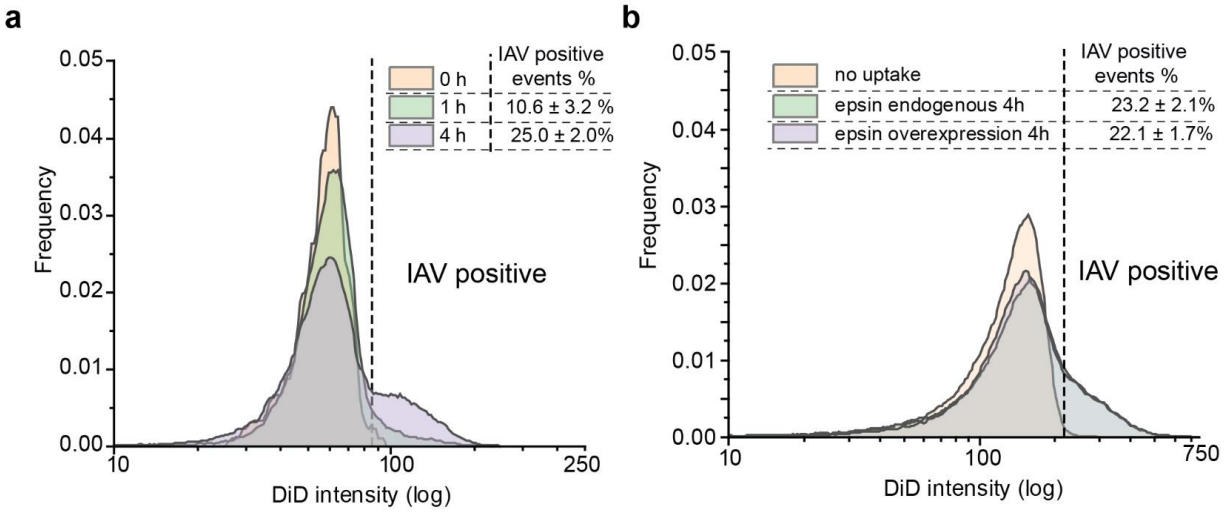

Figure 4.4. Bulk uptake of IAVs is not affected by overexpression of epsin.

a. Flow cytometry histograms showing IAV uptake at 0 hr (no infection), 1 hr and 4 hr in RPE cells overexpressing epsin EGFP. **b.** IAV uptake (4 hr) in RPE cells with endogenous expression of epsin and overexpression of epsin WT. Percentage of cells with IAV internalization is shown in the inset. Experiments were repeated n = 3 and standard deviation is provided in the inset.

4.4.3 Colocalization of IAVs to CCSs and internalization are disrupted by overexpression of epsin mutants without functional ENTH domain.

In Chapters 2 and 3, I showed that ENTH domain of epsin is biomechanically active. The H_0 helix in the N-terminus of ENTH domain acts as a tension sensor and can detect changes in area per lipid in the lipid bilayer. Overexpression of epsin did not affect the bulk uptake of IAV in RPE cells. It has been shown previously that removal of UIMs from epsin can reduce the colocalization

of IAVs with CCSs[130]. I investigated whether removal of biomechanically active ENTH domain also elicit a similar disruption of IAV colocalization with epsin-containing CCSs.

RPE cells stably expressing epsin ΔENTH EGFP and mCherry Clc were infected with DiD-labelled IAVs (H3N2: strain A/Aichi/2/68) for 1 h, before fixation. The cells were imaged using TIRF microscopy to determine the colocalization of IAVs with CCSs containing epsin without ENTH domain (**Figure 4.5a**). IAVs show reduced colocalization with CCSs containing epsin ΔENTH EGFP compared to CCSs containing epsin EGFP (**Figure 4.5b**). Ratio of puncta intensity to background intensity in CCSs with epsin ΔENTH EGFP colocalized with IAVs was lower than that of IAVs colocalizing with epsin EGFP (**Figure 4.5c**). This points to the reduction in strength of recruitment of epsin to CCSs containing IAVs upon removing the ENTH domain. Epsin ΔENTH still possess functional UIMs which mediate the biochemical interaction of IAVs with epsin. This finding may point to a biomechanical role of ENTH domain in localizing IAVs to CCSs. Further colocalization analysis showed using live cell imaging in subsequent sections confirmed this finding.

Using flow cytometry, the bulk uptake of IAVs by RPE cells overexpressing epsin ΔENTH EGFP was quantified. I showed earlier that the overexpression of epsin in RPE cells did not increase IAV uptake. However, RPE cells overexpressing epsin ΔENTH EGFP showed reduced internalization of IAVs compared to cells overexpressing epsin EGFP (**Figure 4.5d**). RPE cells with mutated H_0 helix also showed similar reduction of internalization of IAVs compared to full length epsin. Both results point to disruption of ENTH domain activity abrogates the ability of epsin to act as a cargo-specific adaptor for IAV entry.

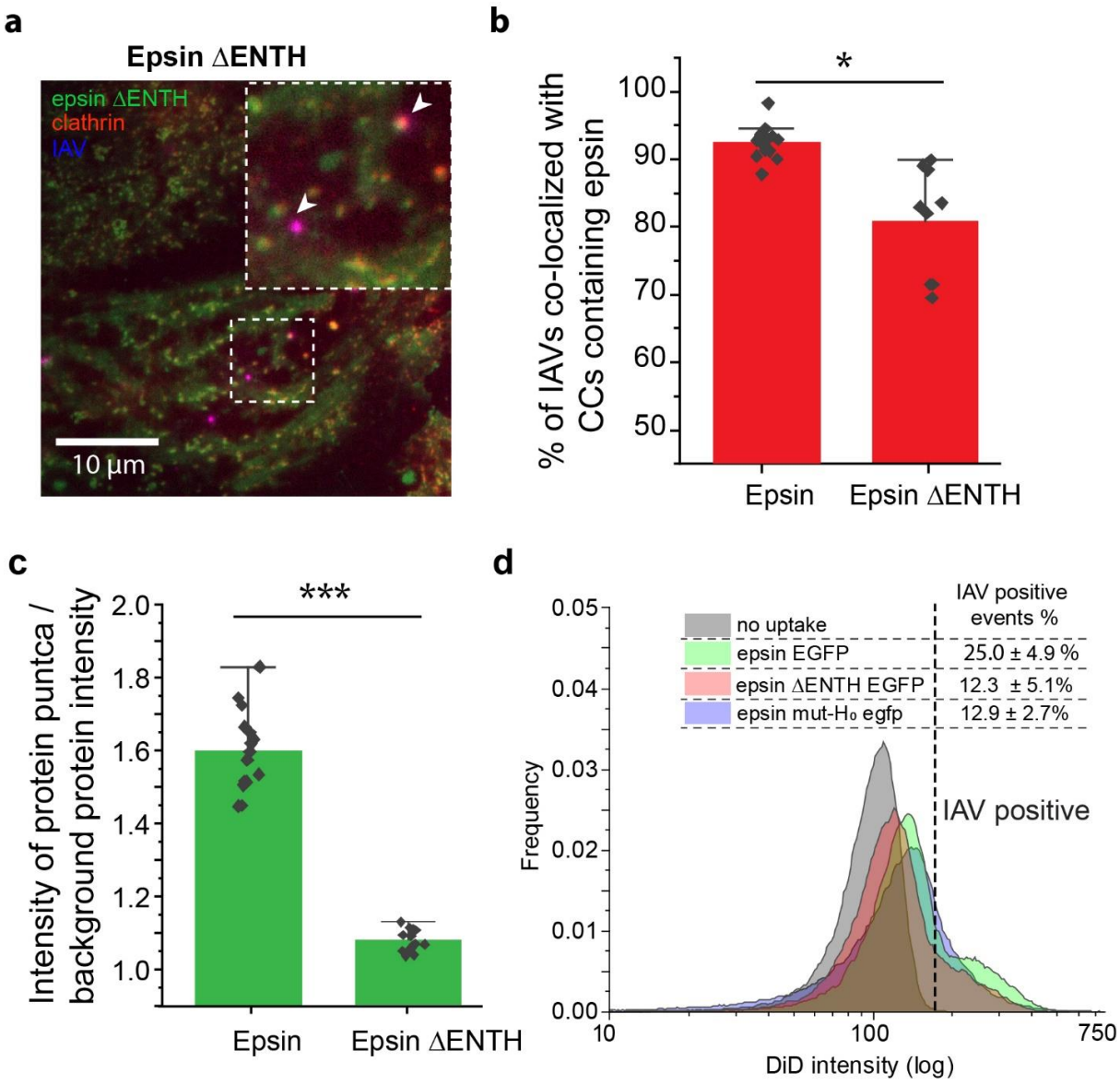

Figure 4.5. Colocalization to CCSs and internalization of IAVs is disrupted in cells overexpressing epsin without a functioning ENTH domain.

a. IAVs bound to surface of RPE cells stably expressing epsin ΔENTH EGFP and mCherry Clc. White arrows in inset show IAVs bound to cell surface. **b.** Percentage of IAVs containing CCSs colocalizing with epsin and epsin ΔENTH . **c.** Ratio of puncta intensity to background intensity of proteins colocalized in IAV containing CCSs **d.** IAV uptake (4 hr) in RPE cells stably expressing epsin EGFP, epsin ΔENTH EGFP and epsin mut-H_0 EGFP. Percentage of cells with IAV internalization is shown in the inset. Experiments were repeated n = 3 and standard deviation is provided in the inset. For b and c, N_{cells} expressing epsin EGFP were 15 and N_{cells} expressing CALM mCherry were 10. The error bars denote standard error. *, *** represent $p < 0.05$ and $p < 0.001$ respectively.

4.4.4 Visualization of IAV entry via CME using lattice light sheet microscopy

CME is often visualized in live cells using TIRFM. However, visualizing viral entry via CME in live cells using TIRFM is not ideal as most entry events occur at the apical side of the cell. Hence, I utilized lattice light-sheet microscopy to track the IAV entry into cells via CME. As lattice

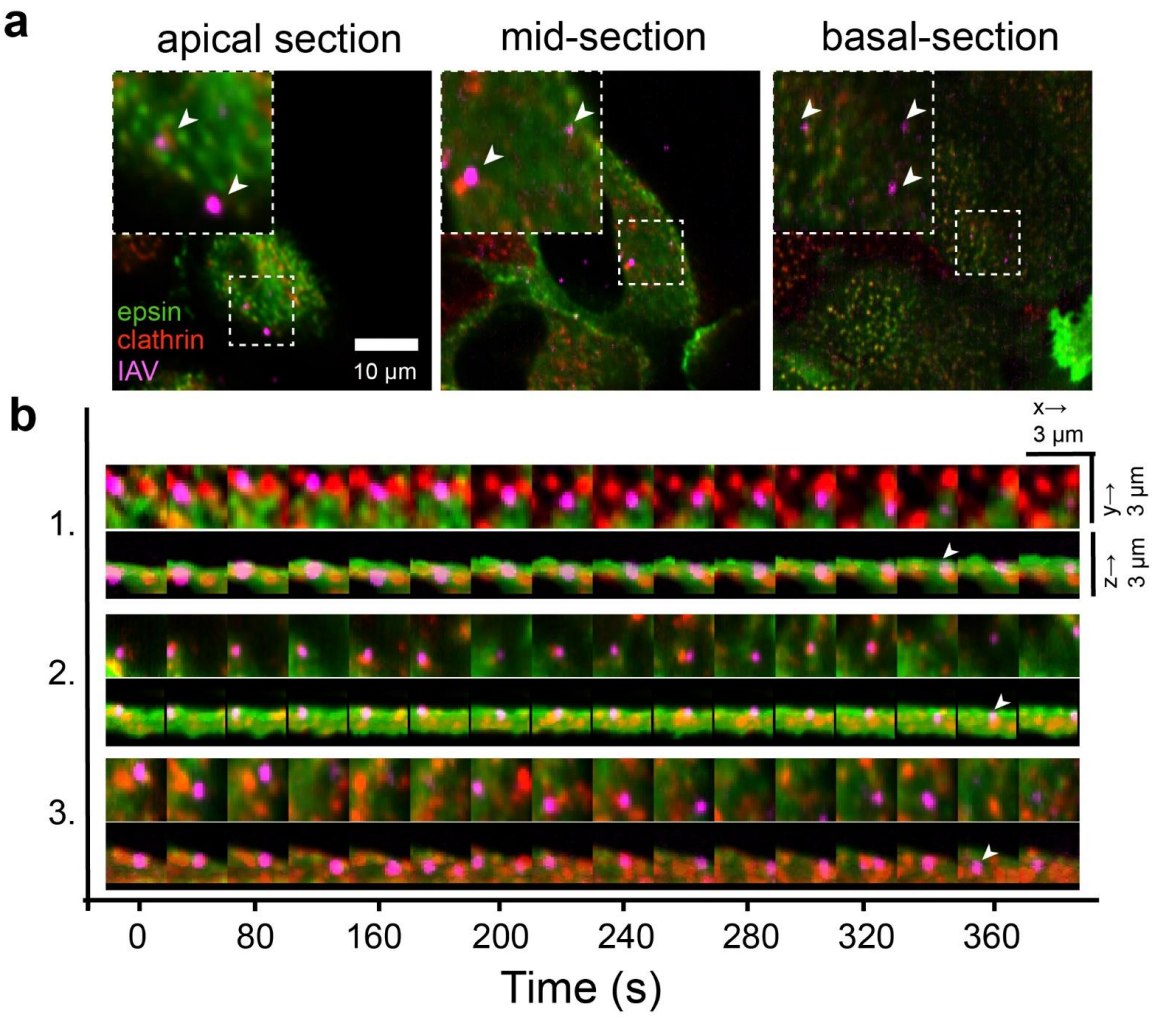

Figure 4.6. IAV internalization visualized using lattice light sheet microscopy.

a. Different sections of RPE cells overexpressing epsin EGFP and mCherry Clc. IAVs are shown with white arrows (inset). **b.** Three example trajectories of IAV (magenta) internalization in *x-y* and *x-z* spatial orientations. The fully internalized IAV is shown using white arrows.

light sheet microscopy performs volumetric imaging of cells, it can visualize the entire cell surface

enabling simultaneous imaging of IAV internalization in apical and basal sections of the cells (**Figure 4.6a**). From the volumetric movies of cells, 3-dimensional tracking was performed using Trackmate to detect and track IAVs binding to the cell surface followed by internalization via CME or non-CME mechanism. The time lapse montages of IAV entry in *x*-*y* and *x*-*z* spatial orientation provide information on when the IAV is internalized by the cell and whether epsin and/or clathrin colocalized with the particular viral particle under consideration (**Figure 4.6b**). We used epsin EGFP as a volume marker to visualize the cytoplasm near plasma membrane where IAVs bind. In *x*-*z* projection of time lapse images of tracked IAV, internalization is characterized by IAVs completely entering the illuminated cytoplasm (shown in white arrows in **Figure 4.6b**). For IAVs bound to the apical section of cells, internalization requires the *z*-position of the IAV moved towards the basal direction of the cell. Together, lattice light sheet microscopy provides an attractive alternative to conventional microscopy techniques to visualize IAV entry.

4.4.5 Cellular entry of filament-forming IAVs via CME

CME is the most well-characterized pathway for IAVs to gain cellular entry. Clathrin-coated vesicles canonically has spherical morphology[1]. We speculate that the shape of the cargo particle may play an important role in the mode of endocytic pathway utilized for cellular entry. Filamentous IAVs have been shown to utilize macropinocytosis as a mode of cellular entry[203]. Thus, I investigated whether epsin plays any role in the internalization of filament-forming IAVs. Our collaborators in the Ono lab generated IAVs which form filaments (WSN-UdM) by replacing the M domain of spherical virus producing IAV strain H1N1: A/WSN/1933 with the M domain of H3N2: A/udorn/1972 strain. The formation of IAV filaments were confirmed in MDCK cells infected WSN-UdM by non-permeabilized immunostaining against influenza surface protein, Hemagglutinin (HA) (**Figure 4.1**). However, DiD-labelled WSN-UdM particles did not show

filamentous nature under TIRFM (**Figure 4.2**). This may be due to the possibility that majority of individual rod-shaped IAVs are around 100-300 nm in size[206] and hence the unevenness of their morphology is below optical resolution limit by TIRF microscopy.

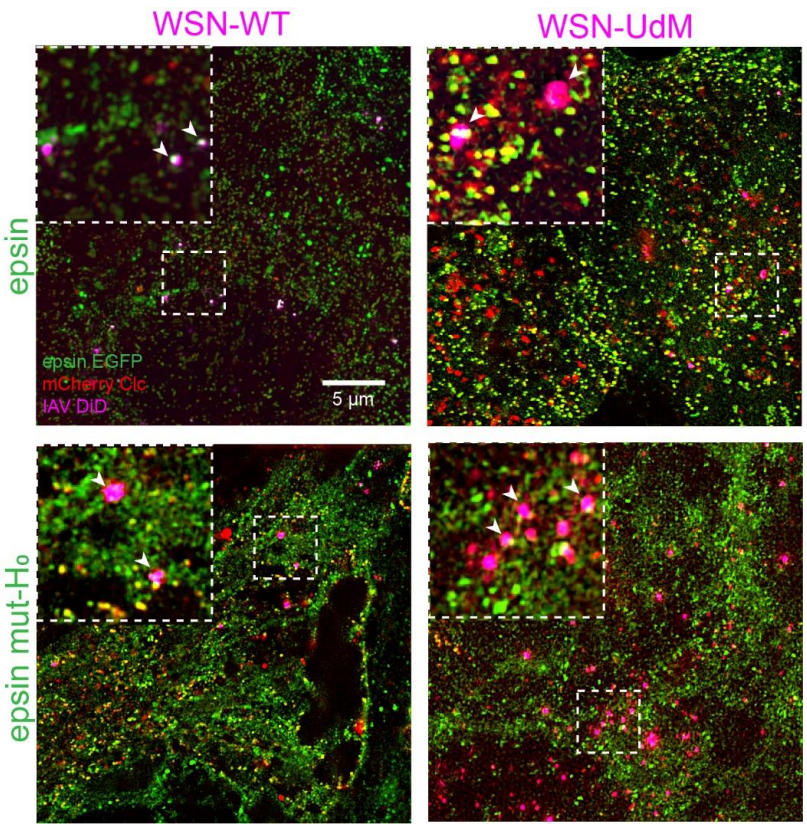

Figure 4.7. Colocalization of spherical and filament-forming IAVs to CCSs.

3D SIM images (maximum intensity projection) of spherical (WSN-WT) and filament-forming (WSN-UdM) viruses bound to CCSs in apical section of RPE cells stably expressing epsin EGFP or epsin mut-H_0 EGFP and mCherry Clc. White arrows in inset show IAVs bound to CCSs on the cell surface.

Even though the canonical shape of a CCS is spherical, non-spherical cargos are internalized via CME[209]. I utilized 3D-structural illumination microscopy (SIM) to visualize the colocalization and morphology CCSs with spherical WSN-WT and filament-forming WSN-UdM on the apical surface of the cell (**Figure 4.7**). Maximum intensity projection of 3D-SIM images of apical surface of RPE cells infected with WSN-WT and WSN-UdM for 1 hr showed colocalization of both viral strains to CCSs. Further both strains were recruited

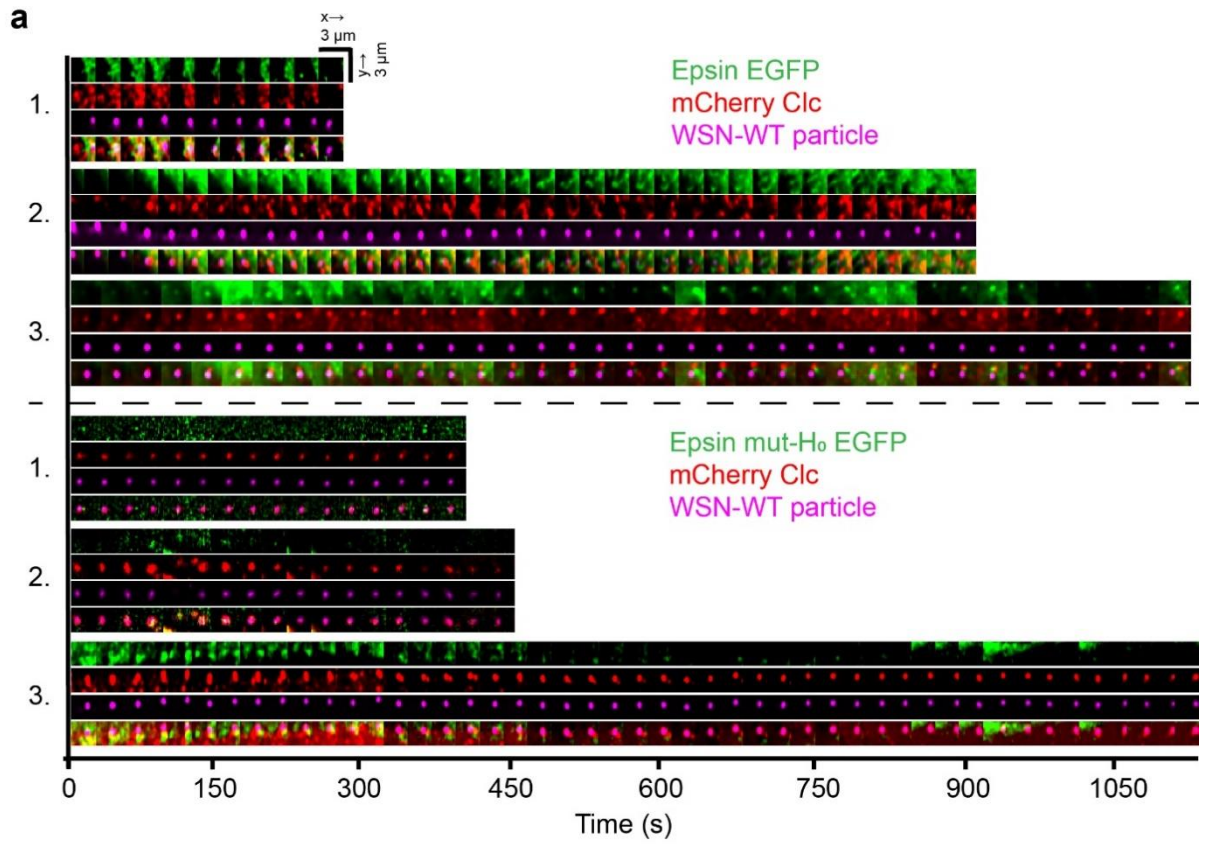
a
x→
3 µm
y→
3 µm
Epsin EGFP
mCherry Clc
WSN-WT particle
1.
2.
3.
Epsin mut-H₀ EGFP
mCherry Clc
WSN-WT particle
1.
2.
3.
0
150
300
450
600
750
900
1050
Time (s)

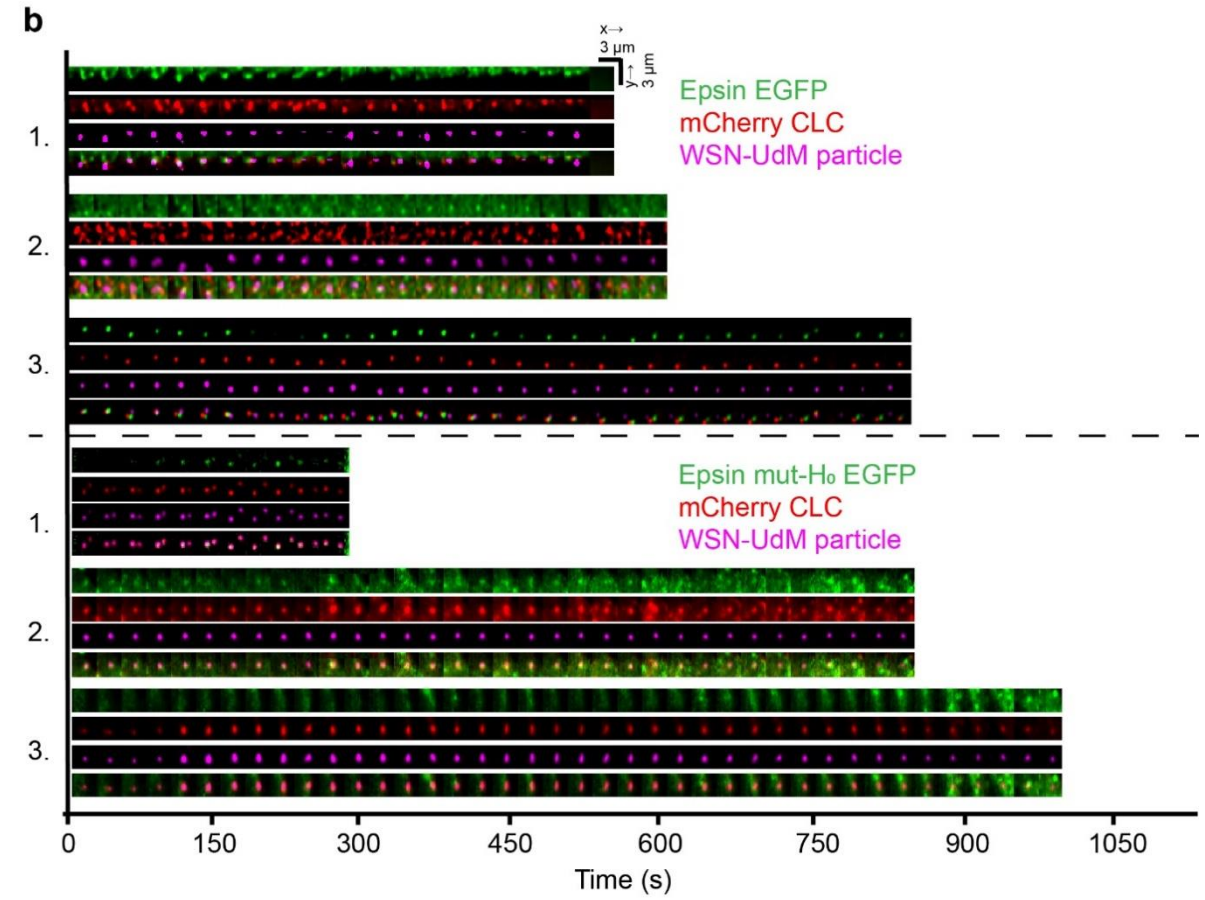
b
x→
3 µm
y→
3 µm
Epsin EGFP
mCherry CLC
WSN-UdM particle
1.
2.
3.
Epsin mut-H₀ EGFP
mCherry CLC
WSN-UdM particle
1.
2.
3.
0
150
300
450
600
750
900
1050
Time (s)

Figure 4.8. Both spherical and filament forming IAVs co-localize and internalize via CCSs.

a Time lapse montages of WSN-WT particles co-localizing with epsin EGFP and mCherry Clc (top panel) and epsin mut-H_0 EGFP and mCherry Clc (bottom panel). **b** Time lapse montages of WSN-UdM particles co-localizing with epsin EGFP and mCherry Clc (top panel) and epsin mut-H_0 EGFP and mCherry Clc (bottom panel).

into CCSs containing epsin EGFP. However, I was not able to delineate significant variations in the morphology of CCSs associated with spherical and filament-forming IAVs.

To understand the particular difference in dynamics of internalization of spherical and filament-forming IAVs via CME, I used live cell imaging with lattice light sheet microscopy to visualize the IAV tracks. I investigated the mode of internalization of WSN-WT and WSN-UdM in RPE cells stably expressing epsin EGFP or epsin mut-H_0 EGFP and mCherry Clc. It has been shown previously that filamentous viruses use macropinocytosis as the preferred mode of endocytosis for cellular entry[203]. I hypothesized that WSN-UdM particles may show lower colocalization and internalization via CCSs as it is shown to form IAV filaments. Surprisingly, time-lapse montages of IAV tracks showed both WSN-WT and WSN-UdM particles internalizing primarily through CME (**Figure 4.8a and 4.8b**). Around 75% of WSN-WT particles and WSN-UdM particles were bound to CCSs during cellular entry **(Figure 4.9a)**. Further, WSN-UdM particle containing CCSs showed strong recruitment of epsin and epsin mut-H_0 compared to WSN-WT bound CCSs. I quantified the strength of recruitment of epsin and epsin mut-H_0 to WSN-WT bound CCSs and WSN-UdM bound CCSs by quantifying the maximum ratio of intensity in the puncta to background from individual IAV tracks. WSN-WT bound CCSs showed high strength of recruitment for epsin EGFP compared to epsin mut-H_0 (**Figure 4.9b**). However, WSN-UdM bound CCSs showed only a small reduction in strength of recruitment for epsin mut-H_0 compared

full length epsin. These findings were in agreement with the 3D-SIM images of WSN-UdM showing colocalization with both epsin and epsin mut-H_0. These findings suggest that interference in H_0 helix formation in epsin does not majorly impact the recruitment of epsin to WSN-UdM bound CCSs.

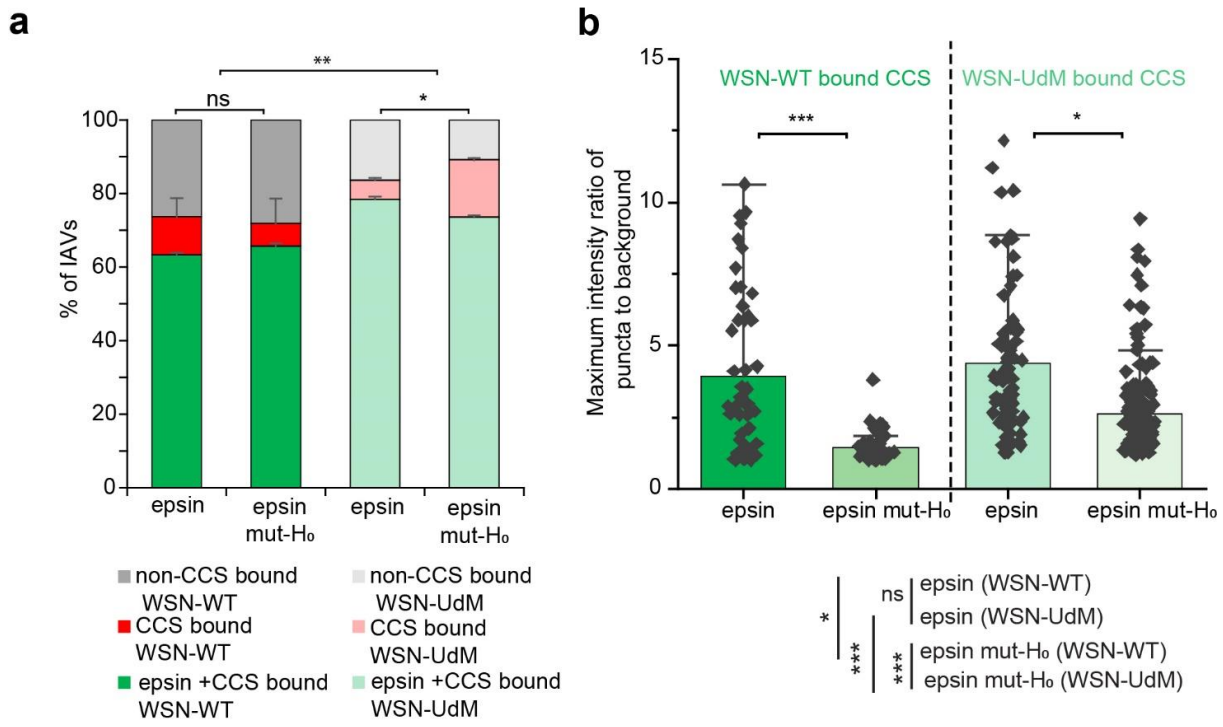

Figure 4.9. CCSs containing filament-forming IAVs strongly recruit epsin.

a. Percentage of WSN-WT and WSN-UdM particles bound to CCSs colocalizing with or without epsin or epsin mut-H_0. **b.** Maximum ratio of puncta intensity to background intensity of epsin or epsin mut-H_0 colocalized with IAV-containing CCSs. For a and b, N_{IAV} tracks for WSN-WT in cells expressing epsin EGFP, WSN-WT in cells expressing epsin mut-H_0 EGFP, WSN-UdM in cells expressing epsin EGFP and WSN-UdM were 91, 105, 180, 225 respectively and corresponding N_{cells} were 18, 14, 15, 21 respectively. The error bars denote standard error. ns represent not significant. *, ** and. *** represent $p < 0.5$, $p < 0.01$ and $p < 0.001$ respectively.

Mutations in H_0 helix of epsin have shown to reduce the bulk uptake of spherical IAVs. Similarly using flow cytometry-based IAV uptake experiments, I investigated whether mutations in epsin mut-H_0 impact the bulk uptake filament-forming IAVs. Filament-forming WSN-UdM viruses show higher uptake than spherical WSN-WT particle **(Figure 4.10a)**. Isogenic clone of WSN-

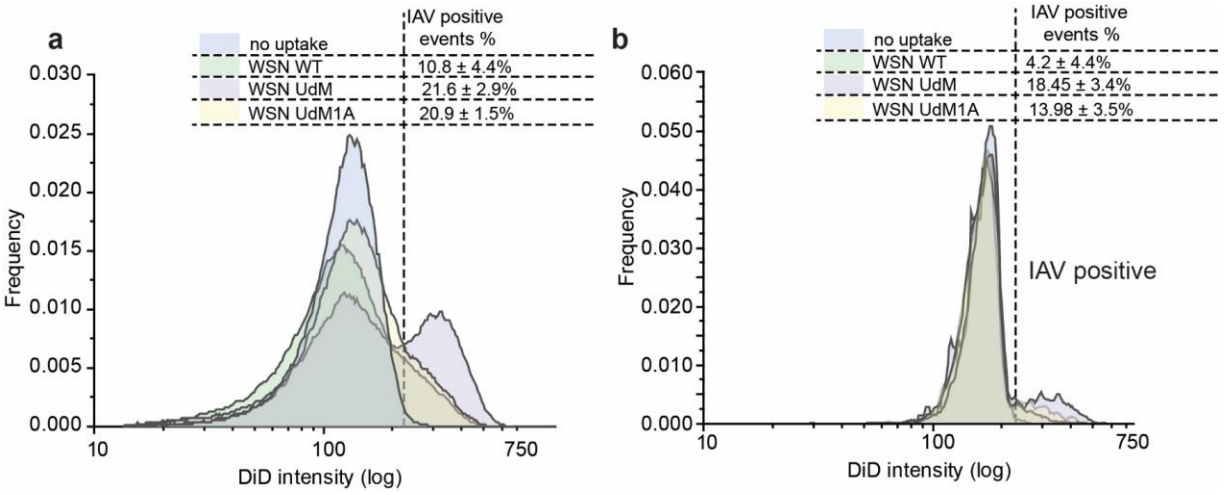

Figure 4.10. Bulk uptake of WSN-UdM is not affected by mutation H_0 in epsin.

a. Uptake (4 hr) of WSN-WT, WSN-UdM and WSN-UdM1A by RPE cells stably expressing epsin EGFP. Percentage of cells with IAV internalization is shown in the inset. **b.** Uptake (4 hr) of WSN-WT, WSN-UdM and WSN-UdM1A by RPE cells stably expressing epsin mut-H_0 EGFP. Percentage of cells with IAV internalization is shown in the inset. For a and b, experiments were repeated n=3 and standard deviation is provided in the inset.

UdM, which cannot form filaments due to a point mutation (WSN-UdM1A) also showed higher uptake than that of WSN-WT. Comparing the uptake of these particles in RPE cells expressing full length epsin and epsin mut-H_0, I observed that uptake of WSN-WT was reduced in RPE cells expressing epsin mut-H_0 **(Figure 4.10a and b)**. However, WSN-UdM did not show significant reduction in internalization in RPE cells expressing epsin mut-H_0 compared to cells expressing full length epsin. However, WSN-UdM1A, the isogenic clone of WSN-UdM1A also showed reduction in internalization to RPE cells expressing epsin mut-H_0 compared to cells expressing full length epsin. Together, these data confirm that filament-forming IAV recruitment is not inhibited by intereference in activity of H_0 helix in the N-terminus of epsin.

4.5 Discussion

Influenza A viruses hijack the activity of endocytic machinery involved in CME to gain cellular entry. Epsin 1, mediated by its UIMs, acts as a cargo specific adaptor for CME of IAVs. In Chapters 2 and 3, I discussed the mechanical regulation of CME by epsin at high membrane tension conditions. Here I uncovered a similar biomechanical role of epsin mediated by its H_0 helix in IAV entry via CME.

UIMs mediate the interaction of epsin with ubiquitinated receptors at IAV binding sites on plasma membrane[130]. I considered CALM, another membrane bending protein from ENTH/ANTH family which is structurally similar to epsin[133], but CALM does not possess UIMs. CALM showed lower strength of recruitment to IAV bound CCSs compared to epsin, confirming the role of UIMs in IAV-mediated recruitment of epsin to CCSs. Interestingly, overexpression of epsin in RPE cells did not lead to an increase in internalization of IAVs. This is consistent with earlier findings that knocking down epsin in cells did not affect the rate of internalization of IAVs[130]. Both these findings point to the ability of IAVs to switch the mode of viral entry to other endocytosis mechanisms or membrane fusion[184].

My investigation along with results from other groups showed that ENTH domain of epsin is biomechanically active with N-terminus H_0 helix in the ENTH domain of epsin acting as a membrane tension and curvature detector[134,156,210]. Further, I showed previously that there exists complementary mechanisms mediated by ENTH domain and C-terminus intrinsically disordered domain of epsin to drive and stabilize membrane curvature necessary for the formation of CCSs at high membrane tension. Internalization of IAVs via CME involves membrane wrapping around IAVs which is energetically costly[62]. IAV tracks obtained using lattice light sheet imaging showed

longer lifetimes for CCSs bound with IAVs consistent with the earlier findings showing that IAV bound CCSs taken longer time to internalize. Motivated by these findings and given that epsin plays an important role in IAV entry via CME, I hypothesize that biomechanical activity of epsin in detecting and driving membrane curvature is necessary for the CCS formation around IAVs. I showed that the removal of ENTH domain from epsin reduces its strength of recruitment to IAV containing CCSs. This result drew comparisons to my earlier findings showing the reduced nucleation of epsin without ENTH into CCSs at high membrane tension. Mutation of H_0 helix in ENTH domain also elicited a similar reduction in strength of recruitment of epsin to IAV containing CCSs. Further, cells overexpressing either epsin mutants without ENTH domain or mutated H_0 helix showed reduction in bulk internalization of IAVs compared to cells expressing full length epsin. This finding is contrary to the earlier results showing that bulk internalization of IAVs is not affected by the expression level of epsin. A potential explanation is that overexpression of epsin mutants with a faulty H_0 helix may compete with and overwhelm endogenous epsin and other membrane bending proteins from binding to IAV bound regions on the cell membrane. The overexpressed epsin mutants still possesses intact UIMs and can bind to the ubiquitinated surface receptors at IAV binding sites without initiating H_0 helix-mediated membrane curvature generation and subsequent nucleation of CCSs around IAVs. Further, IAV uptake experiments using epsin mutant without ENTH domain and UIMs sites will be necessary to test this hypothesis. This mutant will not recognize ubiquitinated surface receptors at IAV binding sites and hence cannot interfere with binding of endogenous membrane bending proteins with UIMs enabling the internalization of IAVs.

The mechanisms that drive the cellular entry of filamentous IAVs is poorly understood. Even though the canonical shape of clathrin-coat assembly is spherical, studies have shown that

non-spherical cargo may also gain cellular entry via CME[211,212]. The internalization of vesicular stomatitis virus via CME is mediated by actin assembly and is regulated by the length of the particle[212]. These filamentous viral particles enter the cells through incompletely coated vesicles that internalize with the aid of actin assembly[211]. This is analogous to the internalization of CCPs at high membrane tension which is also supported by actin assembly[26]. To investigate the pathways through which filamentous IAVs enter cells, our collaborators generated mutant IAVs by replacing the M domain of a spherical laboratory strain with M domain of an IAV strain which produce filamentous particles. The individual filament forming IAVs were not distinguishable from spherical IAVs under TIRF microscopy; however, upon infecting MDCK cells they formed clearly visible filaments which are micrometers long. Compared to spherical IAVs, filament-forming IAVs showed increased bulk internalization into RPE cells. Both 3D-SIM and live-cell tracks of filament-forming IAVs showed that these particles strongly recruit to and are internalized via CCSs. Further, the strength of recruitment of epsin to filament-forming IAVs did not show a drastic drop off as seen in the case of spherical IAVs when the activity of H_0 helix was compromised. In addition, there was no significant drop in bulk internalization of filament-forming IAVs to RPE cells overexpressing epsin mut-H_0 as seen in spherical IAVs. Further the isogenic clone of filament-forming IAV strain with a point mutation preventing the formation of IAV filaments, showed similar uptake characteristics as that of spherical IAVs. This led me to conclude that the unique internalization characteristics of filament-forming IAVs were mediated by the shape of the particles rather than biochemical interactions of M domain. Further investigations is required to uncover how they enable their entry without the membrane curvature generating activity of H_0 helix. I hypothesize that membrane curvature generation by epsin 1 may not play a significant role in the internalization of filament-forming IAVs via CME. Perhaps activity of actin

cytoskeletal assembly is responsible for their entry via CME similar the case of filamentous stomatitis virus. Together, my investigation into IAV entry via CME shows a biomechanical role of epsin in enabling viral entry of spherical IAVs. Although filament-forming IAVs strongly recruit epsin, they did not require the membrane curvature detection and generation of epsin mediated by its H_0 helix.

4.6 Acknowledgments

J.G.J., A.O. and A.P.L. conceived the study, J.G.J., and A.P.L designed the experiments, J.G.J. and performed the experiments. R.M. generated the virus strains. J.G.J. acknowledges Eric Rentchler from UM microscopy core for helping us with lattice light sheet microscopy and 3D-SIM imaging.

Chapter 5 Conclusions and Future Perspective

5.1 Overview

This thesis describes my investigation into the role of mechano-regulation in clathrin-mediated endocytosis (CME), specifically focusing on the role of the membrane bending protein epsin in stabilizing cargo carrying clathrin-coated pits (CCPs).

5.2 Chapter 2 summary and future directions

In Chapter 2, I investigated the effect of membrane tension on the recruitment of epsin into clathrin-coated structures (CCSs). Earlier works from our lab had shown that clathrin recruitment is reduced at high resting membrane tension condition created by forcing cells to spread on large fibronectin islands[32]. In my own work, we found that epsin recruitment to CCSs increased with increasing resting membrane tension. We found that epsin recruitment also increased with acute increase in membrane tension due to hypo-osmotic shock. Epsin-containing CCSs showed high nucleation density at high membrane tension conditions. Further, epsin recruited to CCSs was completed prior to that of clathrin. We hypothesized that insertion of alpha helix at the N-terminus of epsin into the lipid bilayer may be responsible for its unique tension-mediated recruitment into CCSs. The removal of ENTH domain containing H_0 helix did not abrogate the recruitment of epsin to CCSs but reversed the high nucleation density of epsin puncta as well as the high intensity of recruitment of epsin to CCSs at high tension. Removal of ENTH domain also inhibit the ability of epsin to be recruited prior to clathrin into CCSs. Mutating H_0 helix region of epsin or specifically

mutating the PIP_2 binding motifs in the H_0 helix also led to the loss of epsin's unique tension-mediated recruitment. Masking the N-terminus of epsin with an EGFP tag also prevented the early recruitment of epsin to CCSs. Molecular dynamic simulation of the epsin N-terminal homology (ENTH) domain showed the coiling of H_0 helix upon binding to PIP_2 into a more structured domain when embedded in lipid bilayer. Together, these findings led me to conclude that H_0 alpha helix in ENTH domain of epsin can detect the change in area per lipid in bilayer enabling it to detect changes in membrane tension and mediate the tension dependent recruitment of epsin into CCSs.

5.2.1 Does amphipathic helix act as a membrane tension sensor in other endocytic associated proteins?

Multiple families of proteins associated membrane trafficking including small GTPases, ENTH/ANTH family, N-BAR family, Atg proteins are known to possess amphipathic helices (AHs) [208]. These AHs play an important role in membrane curvature detection and induction of membrane fission which are integral in endocytosis[153,155,208]. My investigation into membrane tension-mediated recruitment of epsin into CCSs showed that amphipathic helix H_0 can act a membrane tension sensor[213]. Molecular dynamics simulation from our collaborators have shown that it is the ability of H_0 helix to detect changes in area per lipid in the plasma membrane that enables its tension sensitivity. Formation of H_0 helix upon binding to PIP_2 is not unique to epsin-1, but is observed in other members of ENTH/ANTH families and other protein families[120,127,155]. So I postulate that other H_0 helix containing endocytic proteins can also elicit membrane tension-mediated recruitment with H_0 helix acting as a membrane tension sensor.

To investigate whether other endocytic proteins elicit membrane tension-mediated recruitment, I propose to investigate the recruitment of representative membrane-associated

protein CALM from ANTH family[133], Amphiphysin 2, Endophilin and PICK1 from N-BAR family[155,208], and Arf1 from small GTPase family[208,214]. CALM utilizes its AH to sense and drive membrane curvature and thereby regulates the size and maturation of CCSs[127]. Amphiphysin 2 and Endophilin synergistically recruit dynamin to CCSs and the dynamic clustering of dynamin-amphiphysin helices lead to constriction of membrane and vesicle scission[215–217]. Endophilins form N-BAR lattices on membrane surfaces held by interactions between their N-terminus AHs which lead to curvature generation[218]. AH in PICK1 mediates its membrane curvature sensing enabling its localization to insulin granules, which is critical for the insulin storage in pancreas[210]. GTP activated Arf1 anchors to cell membrane using its N-terminus AH and plays a major role in membrane curvature induction in COPI endocytosis[219]. Altogether, these proteins are involved in integral stages of clathrin-mediated endocytosis and other intracellular trafficking processes including membrane curvature sensing, curvature induction and membrane scission. The amphipathic helical region of these proteins contain PIP_2 binding (K/R/H)(K/R/H)XX(K/R/H) motif[208] **(Table 5.1)**. Our molecular dynamics simulation had shown that the H_0 helix in ENTH domain of epsin is uncoiled in cytosol and coils to form amphipathic helix upon PIP_2 binding followed by horizontal insertion into the lipid bilayer. Further, mutation of PIP_2 binding site RRQMK to SSQMS reverses the tension-mediated elevated recruitment of epsin. Molecular dynamics simulations of amphipathic helices of these proteins, along with plasma

Protein	Amphipathic helix
Epsin 1	1-MSTSSLRRQMKNIVHNY-17
CALM	2-SGQSLTDRITAAQHSVTG-19
Endophilin A1	2-SVAGLKKQFHKATQKVSE-19
Amphiphysin 2	18-VQKKLTRAQEKVLQKLGKA-36
PICK1	113-SLDIVLKKVKHRLVENMS-130
Arf1	1-MGNIFANLFKGLFGKKEMR-19

Table 5.1. PIP_2 binding amphipathic helices in ENTH/ANTH proteins.

Amphipathic helices of different endocytosis associated proteins from ENTH/ANTH family. PIP_2 binding site is marked in red. Adapted from Zhukovsky *et al.* 2019.

membrane recruitment studies of their mutants without PIP_2 binding motif, will help us to understand whether these AHs can act as a tension sensor in addition to the already described roles they play. As membrane tension generally play an inhibitory role in endocytosis, understanding the ability of these proteins to sense tension will provide us with a better mechanistic picture of the molecular machinery involved in endocytosis.

5.3 Chapter 3 summary and future directions

In Chapter 3, I investigated whether elevated recruitment of epsin at high membrane tension environment serves a biological purpose in clathrin-mediated endocytosis. Earlier works from our lab and other groups have shown that membrane tension inhibits clathrin-mediated endocytosis[11,27,28,32]. High membrane tension leads to the premature disassembly of CCSs and prevent CCS transition from hemispherical dome to an omega-shaped pit ready for dynamin-mediated scission and internalization. Using SIM-TIRFM, I visualized the formation of CCSs and characterized them into abortive, productive and stalled structures based on their lifetime and ability form hemispherical domes which appear as a ring shape in super-resolved SIM-TIRF field. Cells overexpressing epsin had a high fraction of productive CCSs which successfully internalize from the plasma membrane. Overexpression of epsin mutant without ENTH domain also showed similar result leading me to conclude that ENTH is not necessary for epsin's role in stabilizing productive CCSs. However, removing the intrinsically disordered domain (IDP) from epsin inhibited its recruitment to CCSs. Specifically, removal of adaptor protein 2 binding motif containing region in epsin rendered it cytosolic. Together, my results support a model where the ENTH and the unstructured IDP region of epsin have complementary roles in which ENTH domain controls CME initiation and IDP region mediates CCS maturation under high tension environments.

5.3.1 Is stabilization of clathrin coat curvature controlled by multivalent interaction of ENTH/ANTH proteins or steric repulsion of their disordered C-terminus domain?

Intrinsically disordered C-terminus region of epsin contains motifs for clathrin and AP2 binding which play a major role in recruitment of epsin to CCSs and providing stability to coat assembly. We hypothesize that multiple endocytic binding sites in ENTH/ANTH proteins interlink the endocytic machinery by acting like a tether creating multivalent interactions. At the same time, steric repulsion created by IDP domains of ENTH/ANTH proteins can generate membrane curvature[18]. It is still not clear whether multivalent interactions or steric repulsion of the C-terminus domain of the ENTH/ANTH protein leads to the stabilization of CCS curvature.

AP180, an ANTH family protein, possesses multiple clathrin, AP2 binding sites (binding to both α2 and β2 appendages) distributed evenly in its structure, binds to PIP_2, and inserts an H_0 helix[162]. Each of the AP2 and clathrin interactions form a link that altogether enables tethering. By generating mutants of AP180 by removing or replacing clathrin binding sites (D[LI]F or DLL), binding sites to α2 appendage of AP2 (DP[FW]), binding sites to β2 appendage of AP2 (DΦ[FW]), we can deduce the effect of multivalent interactions of AP180 to other endocytic proteins and how it influences stability of CCSs. Further, by considering AP180 mutants without a functional ANTH domain such that it cannot bind to PIP_2 nor create H_0 helix insertion, we can study how important these interactions are in stabilizing CCSs. We can quantify the stability of CCS assembly by calculating the fraction of abortive and productive CCSs in cells expressing this mutant.

The role of IDP domain in stabilizing CCS can be determined by studying the stabilization effect of ENTH/ANTH proteins of different hydrodynamic radius. Using an empirical formula developed by Marsh *et al*, I determined the hydrodynamic radius (R_h) of epsin, CALM and AP180 to be 66.6 Å, 60.2 Å and 78.7 Å respectively[220]. Hydrodynamic radius of a disordered protein controls occupancy in 3-dimensional aqueous space and correlates with the crowding effect of the protein[18] **(Figure. 5.1)**. If steric crowding by IDP domain stabilizes clathrin coat curvature, it should lead to more productive CCSs for AP180 followed by epsin and then CALM based on the size of their IDP domains. This can be shown by visualizing the productive CCSs manifesting as rings in a SIM-TIRF field. However, we have to remove the effects of multivalent interactions while studying the contribution of IDP size in curvature stabilization. By generating mutants of epsin and CALM with added IDP regions without endocytic binding sites, we can test the effect of IDP size on CCS stability independent of multivalent interactions. A 199 amino acid long sequence taken from the IDP domain of CALM (IDPΔ [440-638]) which contains no endocytic binding sites can be used as the IDP region to be

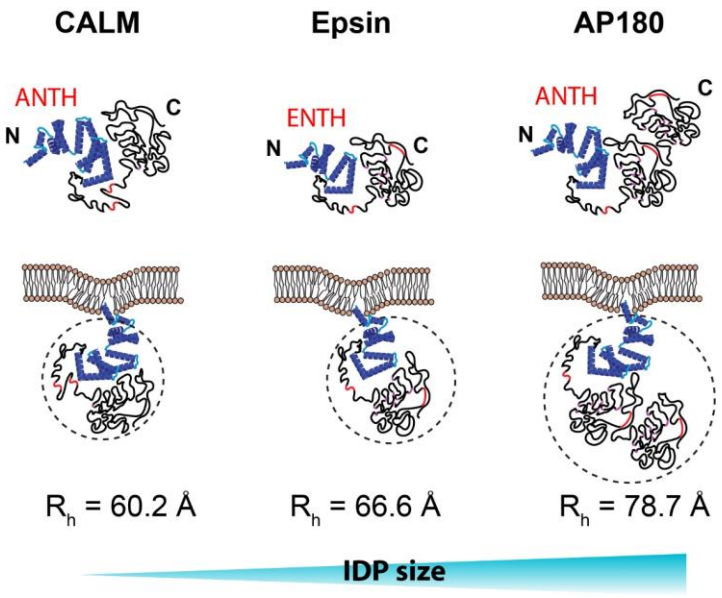

Figure. 5.1. IDP domains of ENTH/ANTH proteins.

Intrinsically disordered structures of epsin, CALM and AP180 along with their estimated hydrodynamic radius (R_h). The dashed circle shows the steric hindrance.

added to generate these mutants. If the hypothesis of IDP size mediating CCS stability is correct, the mutants should exhibit higher stabilization of CCSs than their parent proteins.

5.3.2 How does epsin reducing the fraction of short-lived CCPs affect downstream cell signaling?

Recruitment of epsin into CCSs increases the lifetime of clathrin-coated pits by stabilizing membrane curvature. Cells overexpressing epsin shows reduction in short-lived or abortive CCS. Previous work from our lab showed that epidermal growth factor (EGF) bound to EGF receptor (EGFR) is localized preferentially in short-lived CCSs that correspond to clathrin-dependent EGFR signaling[165]. Phosphorylation of AKT induced by EGF was higher when CME was blocked by the loss of tumor suppressor and lipid phosphatase PTEN. My preliminary investigation into chemokine receptor CXCR4 signaling in cells seeded on PEG

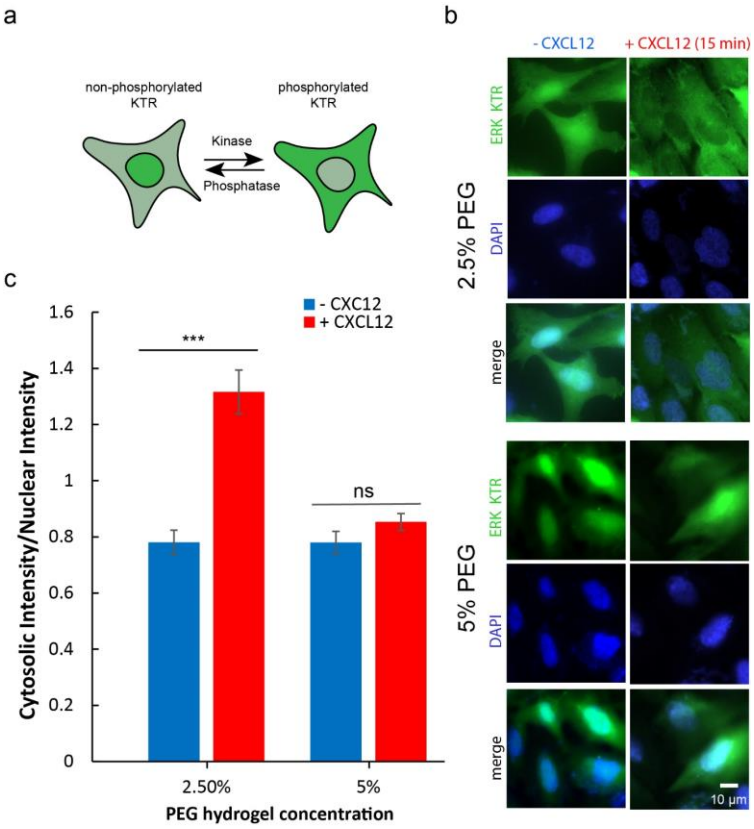

Figure 5.2. Substrate stiffness regulate CXCR4 receptor mediated activation of ERK signaling.

a. Schematic of KTR for reporting the activation of ERK**.** **b.** SUM159 breast cancer cells expressing ERK-KTR seeded on 2.5% and 5% PEG hydrogels. Cells were activated using CXCL12 (50 nM, +15 min). **c.** Quantification of ratio of cytoplasmic to nuclear fluorescence intensity of ERK-KTR (N=10 cells for each condition). The error bars denote standard error. NS denotes not significant. *** represent $p < 0.001$.

hydrogels of different stiffness show activation of ERK signaling in low stiffness condition. I used an ERK-kinase translocation reporter (KTR) which translocates from the nucleus to the cytosol upon phosphorylation of ERK to assess the effect of substrate stiffness on CXCR4 signaling (**Figure 5.2a**)[221]. Fluorescence images of the cells under CXCR4 activation showed clear translocation of ERK-KTR in cells seeded 2.5% PEG hydrogel (**Figure 5.2b**). This was quantified by calculating the ratio of fluorescence intensity of the reporter in the cytosol vs nucleus, The result confirmed that CXCR4 activation leading to ERK signaling is mechanosensitive. Further, our lab showed that clathrin knockdown decreases CXCR4 internalization and increases chemokine CXCL12-induced ERK1/2 phosphorylation[222]. Together these findings lead to the question whether rescue of clathrin-coated pit assembly by epsin affects downstream cell signaling or not. We can assay the effect of epsin-mediated stabilization of CCSs on downstream signaling using the ERK-KTR reporter and AKT-KTR reporter. We should expect downregulation of ERK signaling and AKT signaling in cells overexpressing epsin upon activation by CXCL12 and EGF respectively. This investigation will inform us whether activity of epsin counteracts the hyper activation of AKT and ERK pathways that lead to tumor growth and metastasis[223].

5.4 Chapter 4 summary and future directions

Influenza A viruses (IAVs) hijack CME to gain entry to cells. Membrane bending protein epsin colocalize to IAV-containing CCSs and enabling IAV entry. Epsin interacts with ubiquitinated surface receptors bound to IAVs via its ubiquitin interacting motifs (UIMs). CALM, a structurally similar protein to epsin lacking UIMs, shows weaker recruitment to IAV containing CCSs, confirming the role of UIMs in mediating recruitment of membrane bending proteins to IAV binding sites. Removal of ENTH domain of epsin reduces the affinity of epsin to IAV binding regions of the cell surface. Mutations in ENTH domain that prevent the formation of H_0 helix also

led to similar reduction in affinity of epsin to IAVs. Further bulk internalization of spherical IAVs to RPE cells expressing aforementioned mutants were reduced compared to cells expressing full length epsin. However, overexpression of full length epsin does not increase the internalization of spherical IAVs. This led me to hypothesize that epsin with mutated H_0 may still bind to IAV bound surface receptors using UIMs, but it cannot drive the generation of membrane curvature around IAVs. Internalization of filament-forming IAVs was not affected by the inhibition of H_0 helix formation in ENTH domain of epsin although these particles strongly recruited epsin. I hypothesize that filament-forming IAVs may utilize the activity of other membrane curvature generation proteins such as actin assembly to internalize using CME. Together, these findings support the hypothesis that epsin plays a biomechanical role in viral entry of spherical IAVs.

5.4.1 Role of IAV morphology in determining the endocytosis route for viral entry.

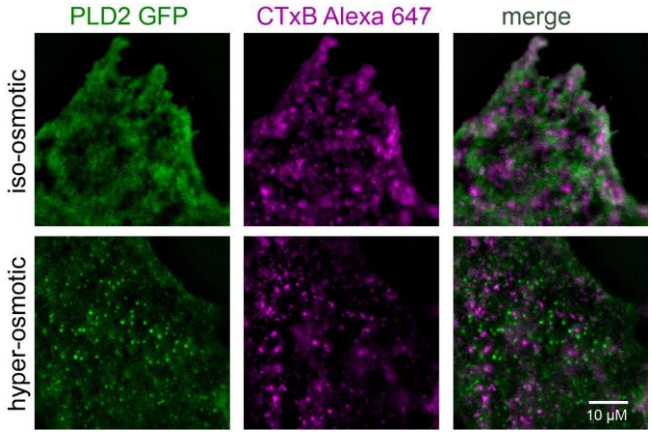

Figure 5.3. Acute drop in membrane tension induces PLD2-mediated macropinocytosis.

C2C12 myoblasts expressing PLD2 GFP cells before and after hyper-osmotic shock. Alexa 647-CTxB label membrane ruffles in the cells.

My investigation showed that entry of filament-forming IAVs did not require membrane curvature detection and generation mediated by ENTH domain of epsin. However, it is clear that filament-forming IAV entry is mechanically sensitive[202,212]. Further, increasing expression level of epsin did not affect the bulk IAV uptake to cells. Studies from other groups showed that filament-forming IAVs internalize via macropinocytosis and their entry is mediated by their morphology and aspect ratio[203,224]. This led

me to hypothesize that IAVs utilize multiple modes of endocytosis for viral entry and the morphology of IAVs may control which pathway IAV entry takes place. Recent findings by my collaborators have pointed to the role of acute reduction plasma membrane tension that activates phospholipase D2 (PLD2) which stimulates macropinocytosis[68]. Live-cell TIRF microscopy of C2C12 myoblasts transiently expressing PLD2 GFP shows the activation of macropinocytosis in plasma membrane regions with ruffling (labelled with CTxB) upon acute membrane tension drop by hyper osmotic shock (**Figure 5.3**). Interestingly, binding of ENTH domain to epsin is shown to reduce membrane tension[116]. Hence, future studies may focus on the mode of internalization of IAVs based on their morphology using CME and PLD2-mediated macropinocytosis. I expect that blocking one particular mechanism of endocytosis may lead to IAVs to switch to an alternate entry mechanism depending on particle size and shape.

5.5 Conclusion and Perspective

Endocytosis has been studied in detail over the past half century [4]. However, a holistic view into the mechanoregulation of endocytic process is only beginning to gain traction in the last decade. Advances in light and electron microscopy with high spatiotemporal resolution and micromechanical manipulation of cells have together pushed the technical capabilities to dissect the mechanoregulation of endocytosis. Along with recent studies from other groups, content of this thesis reveals endocytosis as a process heavily regulated by the mechanical properties of plasma membrane, ECM and cargo[11,25,51,122,189].

Emerging studies are beginning to quantify mechanochemical responses of endocytic proteins during endocytosis[21,62,68,213,225]. Newly discovered endocytic pathways, such as Fast Endophilin-Mediated Endocytosis (FEME) and ultrafast endocytosis, may also be mechanisms

that cells utilize to counter extreme changes in mechanical properties of cells and their surroundings. Given the diverse mechanisms of endocytosis, an important question for future research is to ask whether different endocytic pathways are differentially regulated by mechanical stimuli. From what is currently known, it appears that an increase in membrane tension inhibits all endocytosis. It would be illuminating to monitor two endocytic pathways simultaneously when mechanically perturbed. Further, new knowledge on non-coated mechanosensitive endocytic processes is poised to challenge the existing notions of protein specific membrane bending mechanisms. Alternate mechanisms for membrane bending like steric repulsion by protein crowding, cargo clustering will gain more prominence as a primary mechanism for membrane sculpting. The physiological impact of mechanically regulated endocytosis will also be of significant interest. In particular, many of the endocytic pathways have direct connections to cell signaling pathways. Thus, it is conceivable that part of the mechanotransduction pathway is related to the effect of mechanical stimuli on endocytosis. The plethora of mechanosensitive endocytic processes available at the disposal of cells may point toward an evolutionarily conserved role of endocytosis as a key mechanoregulator.

Organisms undergo and respond to a wide range of mechanical stimuli. Many of the disease states are accompanied by changes in mechanical properties of cells and tissues. The ubiquitous nature of endocytosis and the diverse range of mechanical stimuli in higher organisms pose a great challenge in delineating their co-dependences across different organisms and different biological processes. Current understanding of the mechanics of endocytosis is obtained exclusively from single cell studies perform on two dimensional cultures. However, mechanical stimuli and endocytosis play more complex roles in multicellular processes like embryo development, angiogenesis, and neural plasticity. Exciting new advancements in microscopy like lattice light

sheet microscopy will be instrumental in imaging endocytosis in living organisms beyond the imaging depth of conventional microscopy. Advancements in imaging of endocytic processes in higher-order organisms also call for a greater need in developing automated methods that can simultaneously detect, track and analyze thousands of *in vivo* endocytic events in the midst of interference from motion of organisms, background noise from tissues, and other artifacts. Uncovering the interdependence of mechanical stimuli and endocytic pathways in these contexts will require a combination of sophisticated imaging approaches, powerful analytic techniques and novel tissue manipulation methods.

Bibliography

1. Kaksonen, M. & Roux, A. A. A. Mechanisms of clathrin-mediated endocytosis. *Nat. Rev. Mol. Cell Biol.* **19**, 313–326 (2018).
2. Jones, M. C., Caswell, P. T. & Norman, J. C. Endocytic recycling pathways: emerging regulators of cell migration. *Current Opinion in Cell Biology* vol. 18 549–557 (2006).
3. Fürthauer, M. & González-Gaitán, M. Endocytosis and mitosis: A two-way relationship. *Cell Cycle* vol. 8 3311–3318 (2009).
4. McMahon, H. T. & Boucrot, E. Molecular mechanism and physiological functions of clathrin-mediated endocytosis. *Nat. Rev. Mol. Cell Biol.* **12**, 517–533 (2011).
5. Jain, N., Moeller, J. & Vogel, V. Mechanobiology of Macrophages: How Physical Factors Coregulate Macrophage Plasticity and Phagocytosis. *Annu. Rev. Biomed. Eng.* **21**, 267–297 (2019).
6. Thottacherry, J. J., Sathe, M., Prabhakara, C. & Mayor, S. Spoiled for Choice: Diverse Endocytic Pathways Function at the Cell Surface. *Annu. Rev. Cell Dev. Biol.* **35**, 55–84 (2019).
7. Doherty, G. J. & McMahon, H. T. Mechanisms of Endocytosis. *Annu. Rev. Biochem.* **78**, 857–902 (2009).
8. Zhao, J. & Stenzel, M. H. Entry of nanoparticles into cells: the importance of nanoparticle properties. *Polym. Chem.* **9**, 259–272 (2018).
9. Lacy, M. M., Ma, R., Ravindra, N. G. & Berro, J. Molecular mechanisms of force production in clathrin-mediated endocytosis. *FEBS Lett.* **592**, 3586–3605 (2018).

10. Sochacki, K. A. & Taraska, J. W. From Flat to Curved Clathrin: Controlling a Plastic Ratchet. *Trends Cell Biol.* **29**, 241–256 (2019).

11. Bucher, D. *et al.* Clathrin-Adaptor ratio and membrane tension regulate the flat-To-curved transition of the clathrin coat during endocytosis. *Nat. Commun.* **9**, (2018).

12. Liu, A. P., Chaudhuri, O. & Parekh, S. H. New advances in probing cell-extracellular matrix interactions. *Integr. Biol. (Camb).* **9**, 383–405 (2017).

13. Eisenstein, M. A measure of molecular muscle. *Nature* **544**, 255–257 (2017).

14. Ferguson, J. P. *et al.* Deciphering dynamics of clathrin-mediated endocytosis in a living organism. *J. Cell Biol.* **214**, 347–358 (2016).

15. Aguet, F., Antonescu, C. N., Mettlen, M., Schmid, S. L. & Danuser, G. Advances in analysis of low signal-to-noise images link dynamin and AP2 to the functions of an endocytic checkpoint. *Dev. Cell* **26**, 279–291 (2013).

16. Scott, B. L. *et al.* Membrane bending occurs at all stages of clathrin-coat assembly and defines endocytic dynamics. *Nat. Commun.* **9**, (2018).

17. Stachowiak, J. C. *et al.* Membrane bending by protein–protein crowding. *Nat. Cell Biol.* **14**, 944–949 (2012).

18. Busch, D. J. *et al.* Intrinsically disordered proteins drive membrane curvature. *Nat. Commun.* **6**, 1–11 (2015).

19. Lim, J. P. & Gleeson, P. A. Macropinocytosis: an endocytic pathway for internalising large gulps. *Immunol. Cell Biol.* **89**, 836–843 (2011).

20. Flannagan, R. S., Jaumouillé, V. & Grinstein, S. The Cell Biology of Phagocytosis. *Annu. Rev. Pathol. Mech. Dis.* **7**, 61–98 (2012).

21. Echarri, A. & Del Pozo, M. A. Caveolae - mechanosensitive membrane invaginations

linked to actin filaments. *Journal of Cell Science* vol. 128 2747–2758 (2015).

22. Gauthier, N. C., Masters, T. A. & Sheetz, M. P. Mechanical feedback between membrane tension and dynamics. *Trends Cell Biol.* **22**, 527–535 (2012).

23. Dai, J. & Sheetz, M. P. Regulation of Endocytosis, Exocytosis, and Shape by Membrane Tension. *Cold Spring Harb. Symp. Quant. Biol.* **60**, 567–571 (1995).

24. Mooren, O. L., Galletta, B. J. & Cooper, J. A. Roles for Actin Assembly in Endocytosis. *Annu. Rev. Biochem.* **81**, 661–686 (2012).

25. Apodaca, G. Modulation of membrane traffic by mechanical stimuli. *Am. J. Physiol. Physiol.* **282**, F179–F190 (2017).

26. Boulant, S., Kural, C., Zeeh, J.-C. C., Ubelmann, F. & Kirchhausen, T. Actin dynamics counteract membrane tension during clathrin-mediated endocytosis. *Nat. Cell Biol.* **13**, 1124–1132 (2011).

27. Walani, N., Torres, J. & Agrawal, A. Endocytic proteins drive vesicle growth via instability in high membrane tension environment. *Proc. Natl. Acad. Sci.* **2015**, 201418491 (2015).

28. Hassinger, J. E., Oster, G., Drubin, D. G. & Rangamani, P. Design principles for robust vesiculation in clathrin-mediated endocytosis. *Proc. Natl. Acad. Sci.* **114**, E1118–E1127 (2017).

29. Watanabe, S. & Boucrot, E. Fast and ultrafast endocytosis. *Curr. Opin. Cell Biol.* **47**, 64–71 (2017).

30. Baschieri, F. *et al.* Frustrated endocytosis controls contractility-independent mechanotransduction at clathrin-coated structures. *Nat. Commun.* **9**, (2018).

31. Irajizad, E., Walani, N., Veatch, S. L., Liu, A. P. & Agrawal, A. Clathrin polymerization

exhibits high mechano-geometric sensitivity. *Soft Matter* **13**, 1455–1462 (2017).

32. Tan, X., Heureaux, J. & Liu, A. P. Cell spreading area regulates clathrin-coated pit dynamics on micropatterned substrate. *Integr. Biol. (United Kingdom)* **7**, 1033–1043 (2015).

33. Shi, Z. & Baumgart, T. Membrane tension and peripheral protein density mediate membrane shape transitions. *Nat. Commun.* **6**, 1–8 (2015).

34. Masters, T. A., Pontes, B., Viasnoff, V., Li, Y. & Gauthier, N. C. Plasma membrane tension orchestrates membrane trafficking, cytoskeletal remodeling, and biochemical signaling during phagocytosis. *Proc. Natl. Acad. Sci.* **110**, 11875–11880 (2013).

35. Thottacherry, J. J. *et al.* Mechanochemical Feedback Control of Dynamin Independent Endocytosis Modulates Membrane Tension in Adherent Cells. *Biophys. J.* **116**, 92a--93a (2019).

36. Stachowiak, J. C., Brodsky, F. M. & Miller, E. A. A cost-benefit analysis of the physical mechanisms of membrane curvature. *Nat. Cell Biol.* **15**, 1019–1027 (2013).

37. Dimova, R. Recent developments in the field of bending rigidity measurements on membranes. *Adv. Colloid Interface Sci.* **208**, 225–234 (2014).

38. Pinot, M. *et al.* Polyunsaturated phospholipids facilitate membrane deformation and fission by endocytic proteins. *Science (80-.).* **345**, 693–697 (2014).

39. Jarsch, I. K., Daste, F. & Gallop, J. L. Membrane curvature in cell biology: An integration of molecular mechanisms. *J. Cell Biol.* **214**, 375–387 (2016).

40. Zemel, A., Ben-Shaul, A. & May, S. Modulation of the Spontaneous Curvature and Bending Rigidity of Lipid Membranes by Interfacially Adsorbed Amphipathic Peptides. *J. Phys. Chem. B* **112**, 6988–6996 (2008).

41. Copic, A., Latham, C. F., Horlbeck, M. A., D\textquotesingleArcangelo, J. G. & Miller, E. A. {ER} Cargo Properties Specify a Requirement for {COPII} Coat Rigidity Mediated by Sec13p. *Science (80-.).* **335**, 1359–1362 (2012).

42. Johannes, L., Wunder, C. & Bassereau, P. Bending 'On the Rocks'--A Cocktail of Biophysical Modules to Build Endocytic Pathways. *Cold Spring Harb. Perspect. Biol.* **6**, a016741--a016741 (2014).

43. Morlot, S. *et al.* Membrane Shape at the Edge of the Dynamin Helix Sets Location and Duration of the Fission Reaction. *Cell* **151**, 619–629 (2012).

44. Missirlis, D. The effect of substrate elasticity and actomyosin contractility on different forms of endocytosis. *{PLoS} {ONE}* **9**, e96548 (2014).

45. Jain, N. & Vogel, V. Spatial confinement downsizes the inflammatory response of macrophages. *Nat. Mater.* **17**, 1134–1144 (2018).

46. Patel, N. R. *et al.* Cell Elasticity Determines Macrophage Function. *{PLoS} {ONE}* **7**, e41024 (2012).

47. Scheraga, R. G. *et al.* {TRPV}4 Mechanosensitive Ion Channel Regulates Lipopolysaccharide-Stimulated Macrophage Phagocytosis. *J. Immunol.* **196**, 428–436 (2015).

48. Bordeleau, F. *et al.* Matrix stiffening promotes a tumor vasculature phenotype. *Proc. Natl. Acad. Sci.* **114**, 492–497 (2016).

49. LaValley, D. J. *et al.* Matrix stiffness enhances {VEGFR}-2 internalization, signaling, and proliferation in endothelial cells. *Converg. Sci. Phys. Oncol.* **3**, 44001 (2017).

50. Li, J. *et al.* Integrin endocytosis on elastic substrates mediates mechanosensing. *J. Biomech.* **49**, 2644–2654 (2016).

51. Huang, C. *et al.* Substrate stiffness regulates cellular uptake of nanoparticles. *Nano Lett.* **13**, 1611–1615 (2013).

52. Anselmo, A. C. & Mitragotri, S. Impact of particle elasticity on particle-based drug delivery systems. *Adv. Drug Deliv. Rev.* **108**, 51–67 (2017).

53. Anselmo, A. C. *et al.* Elasticity of nanoparticles influences their blood circulation, phagocytosis, endocytosis, and targeting. *ACS Nano* **9**, 3169–3177 (2015).

54. Lu, F., Wu, S.-H., Hung, Y. & Mou, C.-Y. Size Effect on Cell Uptake in Well-Suspended, Uniform Mesoporous Silica Nanoparticles. *Small* **5**, 1408–1413 (2009).

55. Chithrani, B. D., Ghazani, A. A. & Chan, W. C. W. Determining the Size and Shape Dependence of Gold Nanoparticle Uptake into Mammalian Cells. *Nano Lett.* **6**, 662–668 (2006).

56. Dasgupta, S., Auth, T. & Gompper, G. Shape and Orientation Matter for the Cellular Uptake of Nonspherical Particles. *Nano Lett.* **14**, 687–693 (2014).

57. Brakhage, A. A., Bruns, S., Thywissen, A., Zipfel, P. F. & Behnsen, J. Interaction of phagocytes with filamentous fungi. *Curr. Opin. Microbiol.* **13**, 409–415 (2010).

58. Möller, J., Luehmann, T., Hall, H. & Vogel, V. The Race to the Pole: How High-Aspect Ratio Shape and Heterogeneous Environments Limit Phagocytosis of Filamentous Escherichia coli Bacteria by Macrophages. *Nano Lett.* **12**, 2901–2905 (2012).

59. Sun, J. *et al.* Tunable Rigidity of (Polymeric Core)-(Lipid Shell) Nanoparticles for Regulated Cellular Uptake. *Adv. Mater.* **27**, 1402–1407 (2014).

60. Kruger, T. M. *et al.* Mechanosensitive Endocytosis of High-Stiffness, Submicron Microgels in Macrophage and Hepatocarcinoma Cell Lines. *{ACS} Appl. Bio Mater.* **1**, 1254–1265 (2018).

61. Wei, Q. *et al.* Mechanotargeting: Mechanics-Dependent Cellular Uptake of Nanoparticles. *Adv. Mater.* **30**, 1707464 (2018).

62. Zhang, S., Gao, H. & Bao, G. Physical Principles of Nanoparticle Cellular Endocytosis. *ACS Nano* vol. 9 8655–8671 (2015).

63. Zhang, S., Li, J., Lykotrafitis, G., Bao, G. & Suresh, S. Size-dependent endocytosis of nanoparticles. *Adv. Mater.* **21**, 419–424 (2009).

64. Hu, L., Mao, Z. & Gao, C. Colloidal particles for cellular uptake and delivery. *J. Mater. Chem.* **19**, 3108 (2009).

65. Petersen, E. N., Chung, H.-W., Nayebosadri, A. & Hansen, S. B. Kinetic disruption of lipid rafts is a mechanosensor for phospholipase D. *Nat. Commun.* **7**, (2016).

66. Du, G., Huang, P., Liang, B. T. & Frohman, M. A. Phospholipase D2 Localizes to the Plasma Membrane and Regulates Angiotensin {II} Receptor Endocytosis. *Mol. Biol. Cell* **15**, 1024–1030 (2004).

67. Jiang, Y. *et al.* Phosphatidic Acid Produced by {RalA}-activated {PLD}2 Stimulates Caveolae-mediated Endocytosis and Trafficking in Endothelial Cells. *J. Biol. Chem.* **291**, 20729–20738 (2016).

68. Loh, J. *et al.* An acute decrease in plasma membrane tension induces macropinocytosis via {PLD}2 activation. *J. Cell Sci.* **132**, jcs.232579 (2019).

69. Lin, S.-S. & Liu, Y.-W. Mechanical Stretch Induces {mTOR} Recruitment and Activation at the Phosphatidic Acid-Enriched Macropinosome in Muscle Cell. *Front. Cell Dev. Biol.* **7**, (2019).

70. Banquy, X. *et al.* Effect of mechanical properties of hydrogel nanoparticles on macrophage cell uptake. *Soft Matter* **5**, 3984 (2009).

71. Liu, W. *et al.* Uptake of hydrogel particles with different stiffness and its influence on {HepG}2 cell functions. *Soft Matter* **8**, 9235 (2012).

72. Meng, H. *et al.* Aspect Ratio Determines the Quantity of Mesoporous Silica Nanoparticle Uptake by a Small {GTPase}-Dependent Macropinocytosis Mechanism. *{ACS} Nano* **5**, 4434–4447 (2011).

73. McWhorter, F. Y., Wang, T., Nguyen, P., Chung, T. & Liu, W. F. Modulation of macrophage phenotype by cell shape. *Proc. Natl. Acad. Sci.* **110**, 17253–17258 (2013).

74. Beningo, K. A., Lo, C.-M. & Wang, Y.-L. Flexible polyacrylamide substrata for the analysis of mechanical interactions at cell-substratum adhesions. in *Methods in Cell Biology* 325–339 (Elsevier, 2002). doi:10.1016/s0091-679x(02)69021-1.

75. Bakalar, M. H. *et al.* Size-Dependent Segregation Controls Macrophage Phagocytosis of Antibody-Opsonized Targets. *Cell* **174**, 131-142.e13 (2018).

76. Parton, R. G. & Simons, K. The multiple faces of caveolae. *Nat. Rev. Mol. Cell Biol.* **8**, 185–194 (2007).

77. Richter, T. *et al.* High-Resolution 3D Quantitative Analysis of Caveolar Ultrastructure and Caveola{\textendash}Cytoskeleton Interactions. *Traffic* **9**, 893–909 (2008).

78. del Pozo, M. A. *et al.* Phospho-caveolin-1 mediates integrin-regulated membrane domain internalization. *Nat. Cell Biol.* **7**, 901–908 (2005).

79. Muriel, O. *et al.* Phosphorylated filamin A regulates actin-linked caveolae dynamics. *J. Cell Sci.* **124**, 2763–2776 (2011).

80. Kozera, L., White, E. & Calaghan, S. Caveolae Act as Membrane Reserves Which Limit Mechanosensitive {ICl},swell Channel Activation during Swelling in the Rat Ventricular Myocyte. *{PLoS} {ONE}* **4**, e8312 (2009).

81. Gervasio, O. L., Phillips, W. D., Cole, L. & Allen, D. G. Caveolae respond to cell stretch and contribute to stretch-induced signaling. *J. Cell Sci.* **124**, 3581–3590 (2011).

82. Sinha, B. *et al.* Cells respond to mechanical stress by rapid disassembly of caveolae. *Cell* **144**, 402–413 (2011).

83. Golani, G., Ariotti, N., Parton, R. G. & Kozlov, M. M. Membrane Curvature and Tension Control the Formation and Collapse of Caveolar Superstructures. *Dev. Cell* **48**, 523-538.e4 (2019).

84. Corrotte, M. *et al.* Caveolae internalization repairs wounded cells and muscle fibers. *Elife* **2**, (2013).

85. Mundy, D. I. Dual control of caveolar membrane traffic by microtubules and the actin cytoskeleton. *J. Cell Sci.* **115**, 4327–4339 (2002).

86. Joshi, B. *et al.* Phosphocaveolin-1 is a mechanotransducer that induces caveola biogenesis via Egr1 transcriptional regulation. *J. Cell Biol.* **199**, 425–435 (2012).

87. Peng, F. *et al.* {RhoA} Activation in Mesangial Cells by Mechanical Strain Depends on Caveolae and Caveolin-1 Interaction. *J. Am. Soc. Nephrol.* **18**, 189–198 (2006).

88. Gosens, R. *et al.* Caveolae facilitate muscarinic receptor-mediated intracellular Ca2$\mathplus$ mobilization and contraction in airway smooth muscle. *Am. J. Physiol. Cell. Mol. Physiol.* **293**, L1406--L1418 (2007).

89. Urra, H. *et al.* Caveolin-1-Enhanced Motility and Focal Adhesion Turnover Require Tyrosine-14 but Not Accumulation to the Rear in Metastatic Cancer Cells. *{PLoS} {ONE}* **7**, e33085 (2012).

90. Shi, F. & Sottile, J. Caveolin-1-dependent ~1 integrin endocytosis is a critical regulator of fibronectin turnover. *J. Cell Sci.* **121**, 2360–2371 (2008).

91. Yang, H. *et al.* Mechanosensitive caveolin-1 activation-induced {PI}3K/Akt/{mTOR} signaling pathway promotes breast cancer motility, invadopodia formation and metastasis $\less$i$\greater$in vivo$\less$/i$\greater$. *Oncotarget* **7**, (2016).

92. Goetz, J. *et al.* Biomechanical Remodeling of the Microenvironment by Stromal Caveolin-1 Favors Tumor Invasion and Metastasis. *Cell* **146**, 148–163 (2011).

93. Sandvig, K., Pust, S., Skotland, T. & van Deurs, B. Clathrin-independent endocytosis: mechanisms and function. *Curr. Opin. Cell Biol.* **23**, 413–420 (2011).

94. Thottacherry, J. J. *et al.* Mechanochemical feedback control of dynamin independent endocytosis modulates membrane tension in adherent cells. *Nat. Commun.* **9**, 4217 (2018).

95. Sandvig, K., Kavaliauskiene, S. & Skotland, T. Clathrin-independent endocytosis: an increasing degree of complexity. *Histochem. Cell Biol.* **150**, 107–118 (2018).

96. Howes, M. T. *et al.* Clathrin-independent carriers form a high capacity endocytic sorting system at the leading edge of migrating cells. *J. Cell Biol.* **190**, 675–691 (2010).

97. Howes, M. T., Mayor, S. & Parton, R. G. Molecules, mechanisms, and cellular roles of clathrin-independent endocytosis. *Curr. Opin. Cell Biol.* **22**, 519–527 (2010).

98. Gauthier, N. C., Rossier, O. M., Mathur, A., Hone, J. C. & Sheetz, M. P. Plasma Membrane Area Increases with Spread Area by Exocytosis of a {GPI}-anchored Protein Compartment. *Mol. Biol. Cell* **20**, 3261–3272 (2009).

99. Prévost, C. *et al.* {IRSp}53 senses negative membrane curvature and phase separates along membrane tubules. *Nat. Commun.* **6**, (2015).

100. Sathe, M. *et al.* Small {GTPases} and {BAR} domain proteins regulate branched actin polymerisation for clathrin and dynamin-independent endocytosis. *Nat. Commun.* **9**, (2018).

101. Idone, V. *et al.* Repair of injured plasma membrane by rapid Ca2$\mathplus$-dependent endocytosis. *J. Cell Biol.* **180**, 905–914 (2008).

102. Chernomordik, L. V & Kozlov, M. M. Mechanics of membrane fusion. *Nat. Struct. Mol. Biol.* **15**, 675–683 (2008).

103. Riggi, M. *et al.* TORC2 controls endocytosis through plasma membrane tension. *J. Cell Biol.* **218**, 2265–2276 (2019).

104. DONALDSON, J., PORATSHLIOM, N. & COHEN, L. Clathrin-independent endocytosis: A unique platform for cell signaling and {PM} remodeling. *Cell. Signal.* **21**, 1–6 (2009).

105. Conner, S. D. & Schmid, S. L. Regulated portals of entry into the cell. *Nature* vol. 422 37–44 (2003).

106. Henne, W. M. *et al.* FCHo Proteins Are Nucleators of Clathrin-Mediated Endocytosis. *Science (80-.).* **328**, 1281–1284 (2010).

107. Cocucci, E., Aguet, F., Boulant, S. & Kirchhausen, T. The first five seconds in the life of a clathrin-coated pit. *Cell* **150**, 495–507 (2012).

108. Ferguson, J. P. *et al.* Mechanoregulation of clathrin-mediated endocytosis. *J. Cell Sci.* **130**, 3631–3636 (2017).

109. Ehrlich, M. *et al.* Endocytosis by random initiation and stabilization of clathrin-coated pits. *Cell* **118**, 591–605 (2004).

110. Nunez, D. *et al.* Hotspots Organize Clathrin-Mediated Endocytosis by Efficient Recruitment and Retention of Nucleating Resources. *Traffic* **12**, 1868–1878 (2011).

111. Liu, A. P., Loerke, D., Schmid, S. L. & Danuser, G. Global and Local Regulation of Clathrin-Coated Pit Dynamics Detected on Patterned Substrates. *Biophys. J.* **97**, 1038–

1047 (2009).

112. Tan, X., Luo, M. & Liu, A. P. Clathrin-mediated endocytosis regulates {fMLP}-mediated neutrophil polarization. *Heliyon* **4**, e00819 (2018).

113. Zhao, W. *et al.* Nanoscale manipulation of membrane curvature for probing endocytosis in live cells. *Nat. Nanotechnol.* **12**, 750–756 (2017).

114. Simunovic, M. & Voth, G. A. Membrane tension controls the assembly of curvature-generating proteins. *Nat. Commun.* **6**, 1–8 (2015).

115. Diz-Muñoz, A., Fletcher, D. A. & Weiner, O. D. Use the force: Membrane tension as an organizer of cell shape and motility. *Trends Cell Biol.* **23**, 47–53 (2013).

116. Gleisner, M. *et al.* Epsin N-terminal homology domain (ENTH) Activity as a function of membrane tension. *J. Biol. Chem.* **291**, 19953–19961 (2016).

117. Lai, C.-L. L. *et al.* Membrane Binding and Self-Association of the Epsin N-Terminal Homology Domain. *J. Mol. Biol.* **423**, 800–817 (2012).

118. Hutchison, J. B., Mudiyanselage, A. P. K. K. K., Weis, R. M. & Dinsmore, A. D. Osmotically-induced tension and the binding of N-{BAR} protein to lipid vesicles. *Soft Matter* **12**, 2465–2472 (2016).

119. Cui, H., Lyman, E. & Voth, G. A. Mechanism of membrane curvature sensing by amphipathic helix containing proteins. *Biophys. J.* **100**, 1271–1279 (2011).

120. Drin, G. & Antonny, B. Amphipathic helices and membrane curvature. *FEBS Letters* vol. 584 1840–1847 (2010).

121. Stachowiak, J. C., Hayden, C. C. & Sasaki, D. Y. Steric confinement of proteins on lipid membranes can drive curvature and tubulation. *Proc. Natl. Acad. Sci.* **107**, 7781–7786 (2010).

122. Saleem, M. *et al.* A balance between membrane elasticity and polymerization energy sets the shape of spherical clathrin coats. *Nat. Commun.* **6**, (2015).

123. Naim, H. Y. Apical and basolateral coated pits of {MDCK} cells differ in their rates of maturation into coated vesicles, but not in the ability to distinguish between mutant hemagglutinin proteins with different internalization signals. *J. Cell Biol.* **129**, 1241–1250 (1995).

124. Cordella, N., Lampo, T. J., Mehraeen, S. & Spakowitz, A. J. Membrane fluctuations destabilize clathrin protein lattice order. *Biophys. J.* **106**, 1476–1488 (2014).

125. Saffarian, S., Cocucci, E. & Kirchhausen, T. Distinct Dynamics of Endocytic Clathrin-Coated Pits and Coated Plaques. *{PLoS} Biol.* **7**, e1000191 (2009).

126. Avinoam, O., Schorb, M., Beese, C. J., Briggs, J. A. G. G. & Kaksonen, M. Endocytic sites mature by continuous bending and remodeling of the clathrin coat. *Science (80-.).* **348**, 1369–1372 (2015).

127. Miller, S. E. *et al.* {CALM} Regulates Clathrin-Coated Vesicle Size and Maturation by Directly Sensing and Driving Membrane Curvature. *Dev. Cell* **33**, 163–175 (2015).

128. Grassart, A. *et al.* Actin and dynamin2 dynamics and interplay during clathrin-mediated endocytosis. *J. Cell Biol.* **205**, 721–735 (2014).

129. Henry, A. *et al.* Regulation of Endocytic Clathrin Dynamics by Cargo Ubiquitination. *Dev. Cell* **23**, 519–532 (2012).

130. Chen, C. & Zhuang, X. Epsin 1 is a cargo-specific adaptor for the clathrin-mediated endocytosis of the influenza virus. *Proc. Natl. Acad. Sci.* **105**, 11790–11795 (2008).

131. Mund, M. *et al.* Systematic Nanoscale Analysis of Endocytosis Links Efficient Vesicle Formation to Patterned Actin Nucleation. *Cell* **174**, 884--896.e17 (2018).

132. Simunovic, M. *et al.* Friction Mediates Scission of Tubular Membranes Scaffolded by {BAR} Proteins. *Cell* **170**, 172--184.e11 (2017).

133. Legendre-Guillemin, V., Wasiak, S., Hussain, N. K., Angers, A. & McPherson, P. S. ENTH/ANTH proteins and clathrin-mediated membrane budding. *J. Cell Sci.* **117**, 9–18 (2004).

134. McMahon, H. T. *et al.* Curvature of clathrin-coated pits driven by epsin. *Nature* **419**, 361–366 (2002).

135. Ford, M. G. J. *et al.* Simultaneous binding of PtdIns (4,5) P2 and clathrin by AP180 in the nucleation of clathrin lattices on membranes. *Science (80-.).* **291**, 1051–1055 (2001).

136. Schmid, E. M. & McMahon, H. T. Integrating molecular and network biology to decode endocytosis. *Nature* **448**, 883–888 (2007).

137. Messa, M. *et al.* Epsin deficiency impairs endocytosis by stalling the actin-dependent invagination of endocytic clathrin-coated pits. *Elife* **3**, 1–25 (2014).

138. Capraro, B. R., Yoon, Y., Cho, W. & Baumgart, T. Curvature sensing by the epsin N-terminal homology domain measured on cylindrical lipid membrane tethers. *J. Am. Chem. Soc.* **132**, 1200–1201 (2010).

139. Jaqaman, K. *et al.* Robust single-particle tracking in live-cell time-lapse sequences. *Nat. Methods* **5**, 695–702 (2008).

140. Huang, J. & MacKerell, A. D. CHARMM36 all-atom additive protein force field: Validation based on comparison to NMR data. *J. Comput. Chem.* **34**, 2135–2145 (2013).

141. Jo, S., Kim, T., Iyer, V. G. & Im, W. CHARMM-GUI: A web-based graphical user interface for CHARMM. *J. Comput. Chem.* **29**, 1859–1865 (2008).

142. Gapsys, V., De Groot, B. L. & Briones, R. Computational analysis of local membrane

properties. *J. Comput. Aided. Mol. Des.* **27**, 845–858 (2013).

143. Humphrey, W., Dalke, A. & Schulten, K. VMD: Visual molecular dynamics. *J. Mol. Graph.* **14**, 33–38 (1996).

144. Wrobel, L. K. *et al.* Micropatterning tractional forces in living cells. *Cell Motil. Cytoskeleton* **52**, 97–106 (2002).

145. Gauthier, N. C., Fardin, M. A., Roca-Cusachs, P. & Sheetz, M. P. Temporary increase in plasma membrane tension coordinates the activation of exocytosis and contraction during cell spreading. *Proc. Natl. Acad. Sci. U. S. A.* **108**, 14467–72 (2011).

146. Wen, P. J. *et al.* Actin dynamics provides membrane tension to merge fusing vesicles into the plasma membrane. *Nat. Commun.* **7**, (2016).

147. Zeno, W. F. *et al.* Synergy between intrinsically disordered domains and structured proteins amplifies membrane curvature sensing. *Nat. Commun.* **9**, 1–14 (2018).

148. Wiggins, P. & Phillips, R. Analytic models for mechanotransduction: Gating a mechanosensitive channel. *Proc. Natl. Acad. Sci. U. S. A.* **101**, 4071–4076 (2004).

149. Wiggins, P. & Phillips, R. Membrane-protein interactions in mechanosensitive channels. *Biophys. J.* **88**, 880–902 (2005).

150. Taylor, M. J., Perrais, D. & Merrifield, C. J. A High Precision Survey of the Molecular Dynamics of Mammalian Clathrin-Mediated Endocytosis. *PLoS Biol.* **9**, e1000604 (2011).

151. Bieling, P. *et al.* Force Feedback Controls Motor Activity and Mechanical Properties of Self-Assembling Branched Actin Networks. *Cell* **164**, 115–127 (2016).

152. Panchal, S. C., Kaiser, D. A., Torres, E., Pollard, T. D. & Rosen, M. K. A conserved amphipathic helix in WASP/scar proteins is essential for activation of Arp2/3 complex. *Nat. Struct. Biol.* **10**, 591–598 (2003).

153. Cui, H. *et al.* Understanding the role of amphipathic helices in N-bar domain driven membrane remodeling. *Biophys. J.* **104**, 404–411 (2013).

154. Simunovic, M., Evergren, E., Callan-Jones, A. & Bassereau, P. Curving Cells Inside and Out: Roles of BAR Domain Proteins in Membrane Shaping and Its Cellular Implications. *Annu. Rev. Cell Dev. Biol.* **35**, 1–19 (2019).

155. Fernandes, F. *et al.* Role of helix 0 of the N-BAR domain in membrane curvature generation. *Biophys. J.* **94**, 3065–3073 (2008).

156. Joseph, J. G. & Liu, A. P. Mechanical Regulation of Endocytosis: New Insights and Recent Advances. *Adv. Biosyst.* **4**, 1900278 (2020).

157. Zwiewka, M., Nodzyński, T., Robert, S., Vanneste, S. & Friml, J. Osmotic Stress Modulates the Balance between Exocytosis and Clathrin-Mediated Endocytosis in Arabidopsis thaliana. *Mol. Plant* (2015) doi:10.1016/j.molp.2015.03.007.

158. Boulant, S. Assaying the Contribution of Membrane Tension to Clathrin-Mediated Endocytosis. in *Clathrin-Mediated Endocytosis* 37–50 (Springer New York, 2018). doi:10.1007/978-1-4939-8719-1_4.

159. De Camilli, P. *et al.* The ENTH domain. *FEBS Lett.* **513**, 11–18 (2002).

160. Holkar, S. S., Kamerkar, S. C. & Pucadyil, T. J. Spatial control of epsin-induced clathrin assembly by membrane curvature. *J. Biol. Chem.* **290**, 14267–14276 (2015).

161. Sen, A., Madhivanan, K., Mukherjee, D. & Claudio Aguilar, R. The epsin protein family: Coordinators of endocytosis and signaling. *Biomolecular Concepts* vol. 3 117–126 (2012).

162. Smith, S. M., Baker, M., Halebian, M. & Smith, C. J. Weak molecular interactions in clathrin-mediated endocytosis. *Frontiers in Molecular Biosciences* vol. 4 (2017).

163. Tinevez, J. Y. *et al.* TrackMate: An open and extensible platform for single-particle

tracking. *Methods* **115**, 80–90 (2017).

164. Loerke, D. *et al.* Cargo and Dynamin Regulate Clathrin-Coated Pit Maturation. *PLoS Biol.* **7**, e1000057 (2009).

165. Rosselli-Murai, L. K. *et al.* Loss of PTEN promotes formation of signaling-capable clathrin-coated pits. *J. Cell Sci.* **131**, (2018).

166. Rosselli-Murai, L. K., Joseph, J. G., Lopes-Cendes, I., Liu, A. P. & Murai, M. J. The Machado–Joseph disease-associated form of ataxin-3 impacts dynamics of clathrin-coated pits. *Cell Biol. Int.* cbin.11312 (2020) doi:10.1002/cbin.11312.

167. Cocucci, E., Gaudin, R. & Kirchhausen, T. Dynamin recruitment and membrane scission at the neck of a clathrin-coated pit. *Mol. Biol. Cell* **25**, 3595–3609 (2014).

168. Willy, N. M. *et al.* Endocytic Clathrin Coats Develop Curvature at Early Stages of Their Formation. *bioRxiv* 715219 (2019) doi:10.1101/715219.

169. Pietuch, A., Brückner, B. R. & Janshoff, A. Membrane tension homeostasis of epithelial cells through surface area regulation in response to osmotic stress. *Biochim. Biophys. Acta - Mol. Cell Res.* **1833**, 712–722 (2013).

170. Drake, M. T., Downs, M. A. & Traub, L. M. Epsin Binds to Clathrin by Associating Directly with the Clathrin-terminal Domain. *J. Biol. Chem.* **275**, 6479–6489 (2002).

171. Sochacki, K. A. *et al.* The structure and spontaneous curvature of clathrin lattices at the plasma membrane. *bioRxiv* 2020.07.18.207258 (2020) doi:10.1101/2020.07.18.207258.

172. Brady, R. J., Wen, Y. & O'Halloran, T. J. The ENTH and C-terminal domains of Dictyostelium epsin cooperate to regulate the dynamic interaction with clathrin-coated pits. *J. Cell Sci.* **121**, 3433–3444 (2008).

173. Claudio Aguilar, R., Watson, H. A. & Wendland, B. The yeast epsin Ent1 is recruited to

membranes through multiple independent interactions. *J. Biol. Chem.* **278**, 10737–10743 (2003).

174. Aguilar, R. C. *et al.* Epsin N-terminal homology domains perform an essential function regulating Cdc42 through binding Cdc42 GTPase-activating proteins. *Proc. Natl. Acad. Sci. U. S. A.* **103**, 4116–4121 (2006).

175. Wendland, B., Steece, K. E. & Emr, S. D. Yeast epsins contain an essential N-terminal ENTH domain, bind clathrin and are required for endocytosis. *EMBO J.* **18**, 4383–4393 (1999).

176. Kelly, B. T. *et al.* AP2 controls clathrin polymerization with a membrane-activated switch. *Science (80-.).* **345**, 459–463 (2014).

177. Chen, H. & De Camilli, P. The association of epsin with ubiquitinated cargo along the endocytic pathway is negatively regulated by its interaction with clathrin. *Proc. Natl. Acad. Sci. U. S. A.* **102**, 2766–2771 (2005).

178. Cossart, P. & Helenius, A. Endocytosis of viruses and bacteria. *Cold Spring Harb. Perspect. Biol.* **6**, a016972 (2014).

179. Bayati, A., Kumar, R., Francis, V. & McPherson, P. S. SARS-CoV-2 infects cells after viral entry via clathrin-mediated endocytosis. *Journal of Biological Chemistry* vol. 296 (2021).

180. Piccini, L. E., Castilla, V. & Damonte, E. B. Dengue-3 Virus Entry into Vero Cells: Role of Clathrin-Mediated Endocytosis in the Outcome of Infection. *PLoS One* **10**, (2015).

181. Van Der Schaar, H. M. *et al.* Dissecting the cell entry pathway of dengue virus by single-particle tracking in living cells. *PLoS Pathog.* (2008) doi:10.1371/journal.ppat.1000244.

182. Hu, T. Y., Frieman, M. & Wolfram, J. Insights from nanomedicine into chloroquine

efficacy against COVID-19. *Nat. Nanotechnol.* **15**, 247–249 (2020).

183. Daecke, J., Fackler, O. T., Dittmar, M. T. & Krausslich, H.-G. Involvement of Clathrin-Mediated Endocytosis in Human Immunodeficiency Virus Type 1 Entry. *J. Virol.* (2005) doi:10.1128/jvi.79.3.1581-1594.2005.

184. Shaw, M. L. & Palese, P. Fields Virology 6th. *Fields Virology* (2013).

185. Maartens, G., Celum, C. & Lewin, S. R. HIV infection: Epidemiology, pathogenesis, treatment, and prevention. in *The Lancet* (2014). doi:10.1016/S0140-6736(14)60164-1.

186. Murrell, S., Wu, S. C. & Butler, M. Review of dengue virus and the development of a vaccine. *Biotechnology Advances* (2011) doi:10.1016/j.biotechadv.2010.11.008.

187. Barro, R. J., Ursúa, J. F. & Weng, J. The Coronavirus and the Great Influenza Pandemic: Lessons from the "Spanish Flu" for the Coronavirus's Potential Effects on Mortality and Economic Activity. *SSRN* (2020) doi:10.3386/W26866.

188. Ozili, P. K. & Arun, T. Spillover of COVID-19: Impact on the Global Economy. *SSRN Electron. J.* (2020) doi:10.2139/SSRN.3562570.

189. Wiegand, T. *et al.* Forces during cellular uptake of viruses and nanoparticles at the ventral side. *Nat. Commun. 2020 111* **11**, 1–13 (2020).

190. Sun, S. X. & Wirtz, D. Mechanics of Enveloped Virus Entry into Host Cells. *Biophys. J.* **90**, L10–L12 (2006).

191. Gefen, A. Effects of Virus Size and Cell Stiffness on Forces, Work, and Pressures Driving Membrane Invagination in a Receptor-Mediated Endocytosis. *J. Biomech. Eng.* **132**, (2010).

192. Huang, C., Zhang, Y., Yuan, H., Gao, H. & Zhang, S. Role of Nanoparticle Geometry in Endocytosis: Laying Down to Stand Up. *Nano Lett.* **13**, 4546–4550 (2013).

193. Rennick, J. J., Johnston, A. P. R. & Parton, R. G. Key principles and methods for studying the endocytosis of biological and nanoparticle therapeutics. *Nat. Nanotechnol.* **16**, (2021).

194. Dudek, A. M. *et al.* GPR108 Is a Highly Conserved AAV Entry Factor. *Mol. Ther.* **28**, 367–381 (2020).

195. Büning, H. AAV Entry: Filling in the Blanks. *Mol. Ther.* **28**, 346–347 (2020).

196. Monto, A. S. & Fukuda, K. Lessons From Influenza Pandemics of the Last 100 Years. *Clin. Infect. Dis.* **70**, 951–957 (2020).

197. Dou, D., Revol, R., Östbye, H., Wang, H. & Daniels, R. Influenza A virus cell entry, replication, virion assembly and movement. *Frontiers in Immunology* vol. 9 1 (2018).

198. Böttcher-Friebertshäuser, E., Garten, W., Matrosovich, M. & Klenk, H. D. The hemagglutinin: A determinant of pathogenicity. *Curr. Top. Microbiol. Immunol.* **385**, 3–34 (2014).

199. Rudnicka, A. & Yamauchi, Y. Ubiquitin in influenza virus entry and innate immunity. *Viruses* **8**, 293 (2016).

200. Meineke, R., Rimmelzwaan, G. F. & Elbahesh, H. Influenza Virus Infections and Cellular Kinases. *Viruses* **11**, (2019).

201. Rust, M. J., Lakadamyali, M., Zhang, F. & Zhuang, X. Assembly of endocytic machinery around individual influenza viruses during viral entry. *Nat. Struct. Mol. Biol.* **11**, 567–573 (2004).

202. Dadonaite, B., Vijayakrishnan, S., Fodor, E., Bhella, D. & Hutchinson, E. C. Filamentous influenza viruses. *J. Gen. Virol.* **97**, 1755–1764 (2016).

203. Rossman, J. S., Leser, G. P. & Lamb, R. A. Filamentous Influenza Virus Enters Cells via Macropinocytosis. *J. Virol.* **86**, 10950–10960 (2012).

204. de Vries, E. *et al.* Dissection of the influenza a virus endocytic routes reveals macropinocytosis as an alternative entry pathway. *PLoS Pathog.* **7**, e1001329 (2011).

205. Neumann, G. *et al.* Generation of influenza A viruses entirely from cloned cDNAs. *Proc. Natl. Acad. Sci.* **96**, (1999).

206. Bourmakina, S. V & García-Sastre, A. Reverse genetics studies on the filamentous morphology of influenza A virus. *J. Gen. Virol.* **84**, 517–527 (2003).

207. Lakadamyali, M., Rust, M. J. & Zhuang, X. Endocytosis of influenza viruses. *Microbes Infect.* **6**, (2004).

208. Zhukovsky, M. A., Filograna, A., Luini, A., Corda, D. & Valente, C. Protein Amphipathic Helix Insertion: A Mechanism to Induce Membrane Fission. *Front. Cell Dev. Biol.* **0**, 291 (2019).

209. Decuzzi, P. & Ferrari, M. The Receptor-Mediated Endocytosis of Nonspherical Particles. *Biophys. J.* **94**, 3790 (2008).

210. Herlo, R. *et al.* An Amphipathic Helix Directs Cellular Membrane Curvature Sensing and Function of the BAR Domain Protein PICK1. *Cell Rep.* **23**, 2056–2069 (2018).

211. Cureton, D. K., Massol, R. H., Saffarian, S., Kirchhausen, T. L. & Whelan, S. P. J. Vesicular Stomatitis Virus Enters Cells through Vesicles Incompletely Coated with Clathrin That Depend upon Actin for Internalization. *PLoS Pathog.* **5**, (2009).

212. Cureton, D. K., Massol, R. H., Whelan, S. P. J. & Kirchhausen, T. The length of vesicular stomatitis virus particles dictates a need for actin assembly during clathrin-dependent endocytosis. *PLoS Pathog.* **6**, (2010).

213. Joseph, J. G., Osorio, C., Yee, V., Agrawal, A. & Liu, A. P. Complimentary action of structured and unstructured domains of epsin supports clathrin-mediated endocytosis at

high tension. *Commun. Biol.* **3**, 1–16 (2020).

214. Adarska, P., Wong-Dilworth, L. & Bottanelli, F. ARF GTPases and Their Ubiquitous Role in Intracellular Trafficking Beyond the Golgi. *Front. Cell Dev. Biol.* **0**, 1977 (2021).

215. Takeda, T. *et al.* Dynamic clustering of dynamin-amphiphysin helices regulates membrane constriction and fission coupled with GTP hydrolysis. *Elife* **7**, (2018).

216. Meinecke, M. *et al.* Cooperative Recruitment of Dynamin and BIN/Amphiphysin/Rvs (BAR) Domain-containing Proteins Leads to GTP-dependent Membrane Scission*[S]Ã¢â„¢Â¦. (2013) doi:10.1074/jbc.M112.444869.

217. Simunovic, M., Voth, G. A., Callan-Jones, A. & Bassereau, P. Special Issue: Quantitative Cell Biology When Physics Takes Over: BAR Proteins and Membrane Curvature. *Trends Cell Biol.* **25**, 780–792 (2015).

218. Mim, C. *et al.* Structural Basis of Membrane Bending by the N-BAR Protein Endophilin. *Cell* **149**, 137–145 (2012).

219. Beck, R. *et al.* Membrane curvature induced by Arf1-GTP is essential for vesicle formation. *Proc. Natl. Acad. Sci.* **105**, 11731–11736 (2008).

220. Marsh, J. A. & Forman-Kay, J. D. Sequence Determinants of Compaction in Intrinsically Disordered Proteins. *Biophys. J.* **98**, 2383–2390 (2010).

221. Regot, S., Hughey, J. J., Bajar, B. T., Carrasco, S. & Covert, M. W. High-sensitivity measurements of multiple kinase activities in live single cells. *Cell* (2014) doi:10.1016/j.cell.2014.04.039.

222. DeNies, M. S., Rosselli-Murai, L. K., Schnell, S. & Liu, A. P. Clathrin heavy chain knockdown impacts CXCR4 signaling and post-translational modification. *Front. Cell Dev. Biol.* (2019) doi:10.3389/fcell.2019.00077.

223. Cao, Z. *et al.* AKT and ERK dual inhibitors: The way forward? *Cancer Lett.* **459**, 30–40 (2019).

224. Edinger3, T. O., Pohl3, M. O. & Stertz, S. Entry of influenza A virus: host factors and antiviral targets. doi:10.1099/vir.0.059477-0.

225. Willy, N. M. *et al.* CALM supports clathrin-coated vesicle completion upon membrane tension increase. *Proc. Natl. Acad. Sci.* **118**, (2021).